Julius-Maximimilians-Universität Würzburg

Fakultät für Chemie und Pharmazie

On the correlation between the electronic structure and transport properties of [2.2]paracyclophanes and other aromatic systems

Dissertation zur Erlangung des
naturwissenschaftlichen Doktorgrads der
Julius-Maximilians-Universität Würzburg

vorgelegt von
Johannes Pfister

Würzburg 2011

Eingereicht am: _____

bei der Fakultät für Chemie und Phamrazie.

1. Gutachter: _____

2. Gutachter: _____

der Dissertation

1. Prüfer: _____

2. Prüfer: _____

3. Prüfer: _____

des öffentlichen Promotionskolloquiums.

Tag des öffentlichen Promotionskolloquiums: _____

Doktorurkunde ausgehändigt am: _____

Table of Contents

1. Introduction

The world´s thirst for electrical power grows steadily. The United States Energy Information Administration (EIA) predicts an increase of energy consumption by 49% from $522 \cdot 10^{18}$ J in 2007 to $780 \cdot 10^{18}$ J in 2035 (see figure 1.1).[1] New sources of energy have to be found and existing technologies must be improved to sustain this need of energy. Figure 1.2 contains the 2010 annual report of The Renewable Energy Policy Network for the 21st Century.[2] 2010 78% of the consumed energy was provided by fossil fuels, a limited resource. 2.8% was produced by nuclear energy and 19% by renewable energy sources. It is important to mention that 68% of the energy consumption counted as “renewable” was traditional biomass (plant and animal matter) for heat and cooking fire in developing regions.[3] Only 0.7% of these 19% renewable energy, a very small amount, was produced by wind, solar, biomass and geothermal power plants. Since fossil fuels are limited and rapidly decreasing mankind needs other sources. One possibility is the sun. In one year $3{,}850{,}000 \cdot 10^{18}$ J of energy is absorbed by our planet. Less than 1‰ is used in photosynthesis. Simply put, one year of solar radiation is more energy for the earth than twice

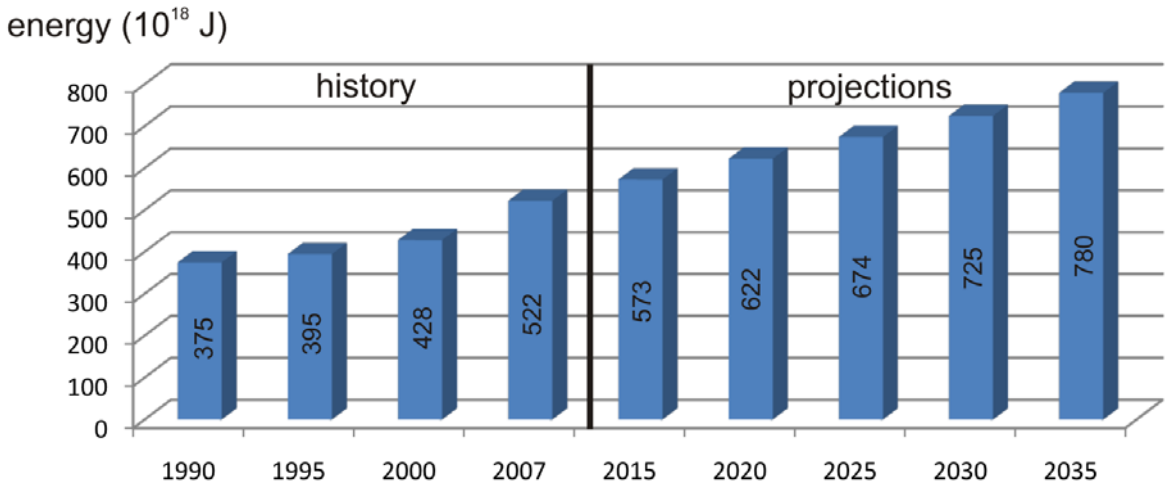

Figure 1.1 Worldwide energy consumption for the last 20 years and future projections. Source: U.S. Energy Information Administration (EIA).

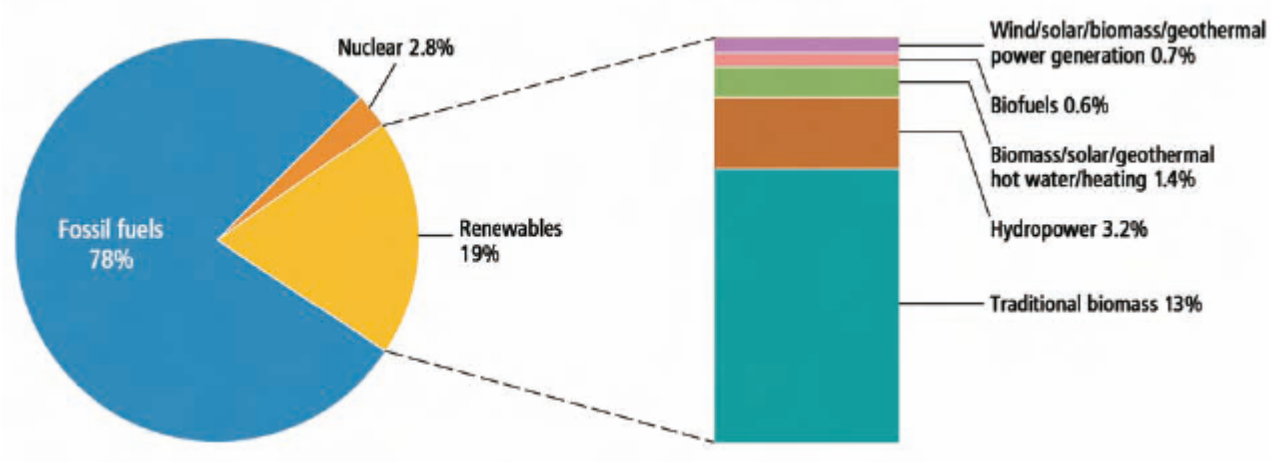

Figure 1.2 Renewable energy share of global energy consumption 2008.[3]

than twice the amount provided by all the planet´s reserves of fossil fuels and uranium combined.[4] The primary energy use in 2005 was "only" $487 \cdot 10^{18}$ J. As a consequence, the complete need of energy could easily be provided by the sun, but the problem is, how can it be harvested?

DESERTEC[5] is one concept of using wind and solar power in deserts in Europe, the Middle East and North Africa. The idea is to use these areas with low population but high amounts of solar radiation to produce electricity and to use this energy for the global market. The power of the sun is harvested in two ways: as solar thermal power and by photovoltaics. The first silicon-based solar cells were built by Gerald Pearson, Calvin Fuller, and Daryl Chaplin in 1954. With an efficiency of 4.5% – 6% the costs were still 286 USD/Watt. A lot of research has been done, but, as figure 1.3 shows, in 2010 photovoltaics are still very expensive in comparison to its alternatives according to the Trade Association for Wind Turbines (Wirtschaftsverband Windkraftwerke e. V.).[6] For more data from different sources, see also Ref.6. To achieve competitiveness these costs have to be reduced by at least a factor of 5. One way to achieve this is the improvement of the efficiency of solar cells. The highest conversion is achieved by inorganic III-V semiconductor solar cells with up to 41.1%. For these so called triple cells composed of GaInP/GaInAs/Ge the sunlight is focused 454-fold. This type is very expensive in the production and in general only used for space travel.[7]

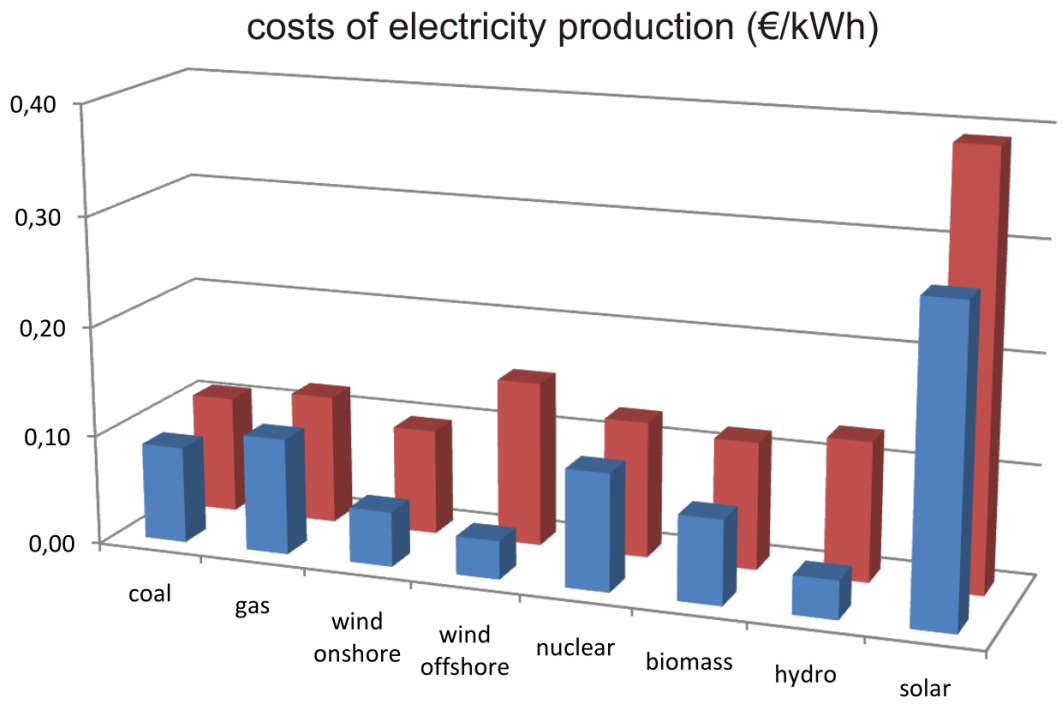

Figure 1.3 Cost of electricity production in 2010 according to the Trade Association for Wind Turbines (Wirtschaftsverband Windkraftwerke e.V. – WVW). Blue and red give the minimal and maximal cost, respectively.[6]

Another possibility to improve the energy/cost ratio is to use cheaper materials. This is the reason for research on organic solar cells.[8-13] Composed of plastics this type has the lowest production cost, but on the other hand, the efficiencies are inferior to their inorganic counterparts. Improvements can be achieved, if we understand how the fundamental processes in solar cells work. The most important concepts are shown in figure 1.4 for an organic heterojunction solar cell: The cell is composed of a transparent indium-tin-oxide (ITO) and a silver (Ag) electrode. In between are the organic donor and acceptor layers, which are mixed heterogeneously, hence its name. Sunlight is absorbed in the donor layer forming an exciton (orange circle, definition see chapter 2). This has to be transferred to the donor-acceptor interface via exciton transport. There, the excited donor molecule transfers an electron to an acceptor molecule forming a polaron pair. After the charges are separated into electron (green circle, negatively charged) and hole (purple circle, positively charged) both have to be transported to their

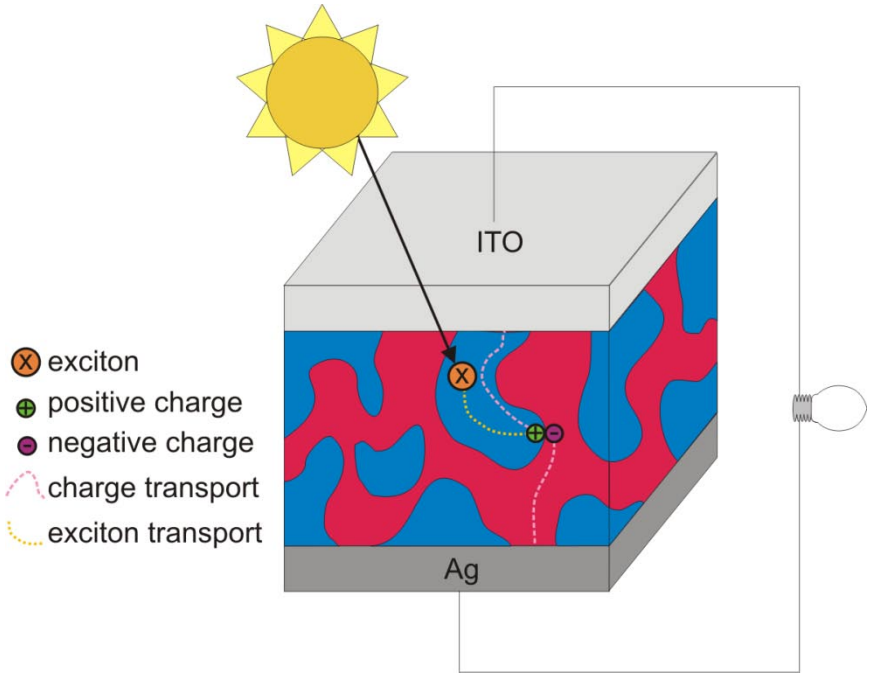

Figure 1.4 Structure of an organic heterojunction solar cell.

corresponding electrodes. There, the charges are transferred and electric current is achieved. Lots of problems reduce the efficiency, like charge recombination, thermal deexcitation, and the thickness of the layers for a perfect balance between absorption and diffusion lengths. The major bottlenecks of organic solar cells are exciton and charge transport. This thesis presents working principles (chapter 2 and 3) and results (chapter 4 to 6) for these fundamental processes.

Organic materials, especially π-conjugated molecules, are also used for applications as electronic devices, *e.g.* organic field-effect transistors (OFETs)[14-18], radiofrequency identification tags[19, 20] and organic light-emitting diodes (OLEDs).[21-24] The material properties of these devices are owing to their capability of electronic switching by electric fields,[25, 26] electromechanical forces[27] or photoactive/photochromic response.[25, 28] Advances in the design of these materials, known as molecular nanotechnology,[29] depend on an improved control of the interplay between the orientation of the molecules relative to another, the photophysics of the individual chromophores as well as energy and charge transport in the bulk.[30] Typically thin films[31, 32] of organic materials are used as device

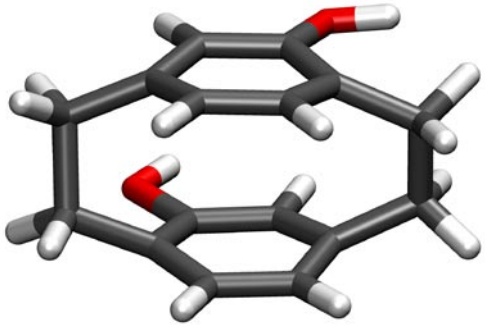

Figure 1.5 *Pseudo-ortho*-dihydroxy[2.2]paracyclophane

components. However, it is challenging to understand these amorphous materials in detail as the molecular subunits experience a range of environments and generally lack the periodic long range order of crystals. Thus, small, well defined model compounds are very well suited to understand fine details of the fundamental processes that give rise to material properties. Such models are *e.g.* [2.2]paracyclophanes and its hydroxyl-substituted derivatives (*e.g. pseudo-ortho*-dihydroxy[2.2]paracyclophane, see figure 1.5). They are unique with respect to the strong “through-space” coupling of the π-systems of their benzene moieties and are thus promising candidates as materials due to their specific photophysical properties[33-37] and their high electric conductivity.[38-40] [2.2]Paracyclophane is known since 1949[41] and has been widely modified.[42-48] These compounds can be regarded as models for closely packed π-systems bound together by organic bridges. The influences of the distance between the two benzene subunits on photo absorption properties can be investigated by varying the bridge length and/or the substitution pattern at the π-systems.

2. Model Concepts and Background

2.1 Transport in Organic Materials

Charge and exciton transport play very important roles in organic materials. While the first considers only one particle, namely a charge, which is either a positive hole or a negative electron to be transferred, exciton transport is described in a two particle picture: Simultaneously one electron is deexcited in one system while a second one is promoted in another system (in this thesis two organic molecules). Both transport processes follow the same fundamental concepts. The most important are Fermi´s Golden Rule, the Franck-Condon principle, and Marcus theory. These will be discussed in this chapter in detail and applied on both exciton and charge transport.

2.1.1 Fermi´s Golden Rule

The following chapter is based on the PhD work of P. Marquetand[49] and the textbooks of G. Baym,[50] F. Schwabl,[51] and P. W. Atkins *et al*.[52]

Fermi´s Golden Rule is one of the most important and widely used expression of quantum mechanics. Despite its name it is based on Gregor Wentzel´s work on the photoelectric effect[53] and the radiationless Auger-Meitner-Effect.[54] The term “Golden Rule” originates from Fermi, who called it “Golden Rule No.2”[55] in his lecture notes to honor its conceptual and practical importance. Fermi references this equation to Dirac´s work[56] about the quantum theory of absorption and emission of radiation. To derive Fermi´s Golden Rule time-dependent perturbation theory is applied:

The interaction between matter and a time-dependent external electric field can be described by a time-dependent Hamiltonian

$$\hat{H}(t) = \hat{H}_0 + \hat{W}(t), \tag{2.1}$$

where $\hat{H}_0$ is the Hamiltonian of the unperturbed system and $\hat{W}(t)$ the time-dependent interaction. For a purely vibrational interaction, a permanent dipole moment μ is exhibited by the molecule. Then, the time-dependent interaction is

$$\hat{W}(t) = -\mu\vec{E}(t)\cos\theta. \tag{2.2}$$

where θ is the angle between the electric field vector and the dipole moment. The perturbation is furthermore defined to be

$$\widehat{W}(t) = 0 \text{ for } t \leq t_0 \text{ and}$$

$$\widehat{W}(t) > 0 \text{ for } t > t_0. \tag{2.3}$$

In the case of a transition between two electronic states, generally written as initial and final state $|i\rangle$ and $|f\rangle$, the Hamiltonian is written as

$$\widehat{H}(t) = \begin{pmatrix} \widehat{T} + V_i & -\vec{\mu}_{if}\vec{E}(t) \\ -\vec{\mu}_{if}\vec{E}(t) & \widehat{T} + V_f \end{pmatrix} \tag{2.4}$$

or

$$\widehat{H}(t) = |i\rangle\left(\widehat{T} + V_i\right)\langle i| + |i\rangle\left(-\vec{\mu}_{if}\vec{E}(t)\right)\langle f| + |f\rangle\left(-\vec{\mu}_{if}\vec{E}(t)\right)\langle i| + |f\rangle\left(\widehat{T} + V_f\right)\langle f| \tag{2.5}$$

with $\widehat{T}$ as the kinetic operator, V_n as the potential energy in state $|n\rangle$ $(n = i, f)$ and $\vec{\mu}_{if}$ as the transition dipole moment.

Applying time-dependent perturbation theory, the interaction of a weak laser field with a molecule can be described.[51] For $t \leq 0$, when no perturbation is present, the system obeys

$$i\hbar\frac{\partial}{\partial t}\Psi_0(t) = \widehat{H}_0\Psi_0(t). \tag{2.6}$$

Due to the perturbation this changes for larger times to

$$i\hbar\frac{\partial}{\partial t}\Psi_0(t) = \left\{\widehat{H}_0 + \widehat{W}(t)\right\}\Psi(t). \tag{2.7}$$

It is convenient to separate the unperturbed system, normally presumed to be known, from the perturbed system. For that reason we change to the interaction representation index I), also known as Dirac-representation, where

$$\Psi(t) = e^{-\frac{i}{\hbar}\widehat{H}_0 t}\Psi_I(t) \tag{2.8}$$

and

$$\widehat{W}_I(t) = e^{\frac{i}{\hbar}\widehat{H}_0 t}\widehat{W}(t)e^{-\frac{i}{\hbar}\widehat{H}_0 t}. \tag{2.9}$$

The Schrödinger equation for the perturbed system now is written

$$i\hbar \frac{\partial}{\partial t} \Psi_I(t) = \widehat{W}_I(t) \Psi_I(t). \tag{2.10}$$

Time integration leads to

$$\Psi_I(t) = \Psi_I(t_0) + \frac{1}{i\hbar} \int_{t_0}^{t} dt' \, \widehat{W}_I(t') \Psi_I(t'), \tag{2.11}$$

where at a time t = t_0, the wave function $\Psi_I(t_0) = \Psi(t_0)$. An approximate solution can be obtained by iteration into the following series expansion:

$$\begin{aligned} \Psi_I(t) &= \Psi_I(t_0) + \frac{1}{i\hbar} \int_{t_0}^{t} dt' \, \widehat{W}_I(t') \left[\Psi_I(t_0) + \frac{1}{i\hbar} \int_{t_0}^{t'} dt'' \, \widehat{W}_I(t'') \left[\ldots \right] \right] \\ &= \Psi_I(t_0) + \frac{1}{i\hbar} \int_{t_0}^{t} dt' \, \widehat{W}_I(t') \Psi_I(t_0) \\ &\quad + \left(\frac{i}{\hbar} \right)^2 \int_{t_0}^{t} dt' \int_{t_0}^{t'} dt'' \, \widehat{W}_I(t') \widehat{W}_I(t'') \Psi_I(t_0) + \ldots \end{aligned} \tag{2.12}$$

Truncation of the wavefunction after the first integral is termed $\Psi_I^{(1)}$, because a first order correction is applied. The notation for higher orders proceeds analogously. The first-order wave function can be evaluated by using Eq. 2.9:

$$\begin{aligned} \Psi^{(1)}(t) &= e^{-\frac{i}{\hbar}\widehat{H}_0 t} \Psi_I^{(1)}(t) \\ &= e^{-\frac{i}{\hbar}\widehat{H}_0 t} \left[\Psi_I(t_0) + \frac{1}{i\hbar} \int_{t_0}^{t} dt' \, \widehat{W}_I(t') \Psi_I(t_0) \right] \\ &= e^{-\frac{i}{\hbar}\widehat{H}_0 t} \Psi_I(t_0) + \frac{1}{i\hbar} \int_{t_0}^{t} dt' \, e^{-\frac{i}{\hbar}\widehat{H}_0 (t - t')} \widehat{W}_I(t') e^{-\frac{i}{\hbar}\widehat{H}_0 t'} \Psi(t_0). \end{aligned} \tag{2.13}$$

Higher-order terms can be obtained analogously.

An application of time-dependent perturbation theory is to describe transitions between two eigenstates of a quantum system. The eigenstates $|n\rangle$ with their eigenvalues E_n form an orthonormal basis and obey the time-independent Schrödinger equation

$$\widehat{H}_0 |n\rangle = E_n |n\rangle. \tag{2.14}$$

First, the system, described by $\Psi(t)$, is in the initial state $|i\rangle$, which is not necessarily the ground state. The probability $P_{if}(t)$ that the transition to the final state $|f\rangle$ has happened at time t is given by[50]

$$P_{if}(t) = |\langle f|\Psi_I(t)\rangle|^2 = |\langle f|\Psi(t)\rangle|^2. \tag{2.15}$$

Within first-order perturbation theory (see Eq. 2.13) the transition amplitude $\langle f|\Psi(t)\rangle$ is evaluated as:

$$\langle f|\Psi^{(1)}(t)\rangle = \left\langle f\left|e^{-\frac{i}{\hbar}\hat{H}_0 t}\right|i\right\rangle + \frac{1}{i\hbar}\int_{t_0}^{t} dt' \left\langle f\left|e^{-\frac{i}{\hbar}\hat{H}_0(t-t')}\hat{W}(t')e^{-\frac{i}{\hbar}\hat{H}_0 t'}\right|i\right\rangle \tag{2.16}$$

$$= -\frac{i}{\hbar}e^{-\frac{i}{\hbar}E_2 t}\int_{t_0}^{t} dt' e^{\frac{i}{\hbar}(E_f-E_i)t'}\langle f|\hat{W}(t')|i\rangle$$

Therefore, the transition probability can be written as

$$P_{if}(t) = \left|\frac{i}{\hbar}\int_{t_0}^{t} dt' e^{\frac{i}{\hbar}(E_f-E_i)t'}\langle f|\hat{W}(t')|i\rangle\right|^2. \tag{2.17}$$

Setting $\hat{W}$ independent of time, *i.e.* adding a small constant term W to the Hamiltonian at t = 0, we get for

$$P_{12}(t) = \left|\frac{i}{\hbar}\frac{e^{\frac{i}{\hbar}(E_f-E_i)t}-1}{\frac{i}{\hbar}(E_f-E_i)}\langle f|W|i\rangle\right|^2 \tag{2.18}$$

$$= \left|\frac{2\sin\left(\frac{1}{2}\frac{E_f-E_i}{\hbar}t\right)}{E_f-E_i}\langle f|W|i\rangle\right|^2,$$

where $e^{ia} - e^{ib} = 2\sin\frac{1}{2}(a-b)$ was applied.[50] Describing an optical transition in this frame has to consider several final states $|k\rangle$ representing the different vibrational levels, which are close in energy. These are accessible due to the spectral width of W. To calculate the total transition probability, one has to sum over all states. This is approximated by an integral over the energies E_k times the density of states ρ (number of states per unit energy). Then, the transition probability equals to

$$\sum_k P_{ik}(t) \approx |\langle k|W|i\rangle|^2 \int dE_k \rho(E_k)\left|\frac{2\sin\left(\frac{E_k-E_i}{2\hbar}t\right)}{E_k-E_i}\right|^2. \tag{2.19}$$

When t is long enough, the density of states factor can be taken out of the integral and evaluated as

$$\int dE_k \left| \frac{2\sin\left(\frac{E_k - E_i}{2\hbar} t\right)}{E_k - E_i} \right|^2 = \frac{2\pi}{\hbar} t. \tag{2.20}$$

This leads to the transition rate $\Gamma = \frac{d}{dt} \sum_k P_{ik}(t)$, which is the transition probability per time unit. It is approximated by

$$\Gamma = \frac{2\pi}{\hbar} |\langle k|W|i\rangle|^2 \rho(E_i). \tag{2.21}$$

This equation is also called Fermi´s Golden Rule. $\langle k|W|i\rangle$ is also known as transfer integral or electronic coupling V_{ec}. Many different forms of Fermi´s Golden Rule exist, *e.g.*

$$\Gamma = \frac{2\pi}{\hbar} |V_{ec}|^2 \delta(E_f - E_i). \tag{2.22}$$

2.1.2 Franck-Condon Principle

This chapter is based on the text book of Atkins *et al.*[52] Whenever an electronic transition takes place in a molecule the electronic structure, i.e. the distribution of the electrons, changes. As a result the nuclei move on a different energy potential and therefore, they respond by breaking into more vigorous vibration and the absorption spectrum shows a structure characteristic of the vibrational energy levels of the molecule. The combination of electronic and vibrational transitions is known as vibronic transitions. They can be explained and predicted with the help of the Franck-Condon principle.

A fundamental approximation used in the Franck-Condon principle is the Born-Oppenheimer Approximation. There, it is assumed that due to the difference in masses between electrons and nuclei the electrons move much faster. As a consequence the total wavefunction Ψ can be separated into a product of the electronic wavefunction Ψ_{el} and the nuclear wavefunction Ψ_n:

$$\Psi(\vec{r_i}, \vec{R_j}) = \Psi_{el}(\vec{r_i}, \vec{R_j}) \cdot \Psi_n(\vec{R_j}) \tag{2.23}$$

The Franck-Condon principle implements the Born-Oppenheimer approximation into vibronic transitions. During the electronic transition the cores are treated as stationary, but then adjust once the electrons have adopted their final distribution.

Qualitatively the Franck-Condon principle can be illustrated in figure 2.1. For a diatomic molecule two potential energy curves for two electronic states are depicted. R is the bond distance between the nuclei. The upper curve is typically displaced to the right, as an excitation normally occurs from bonding to antibonding molecular orbitals

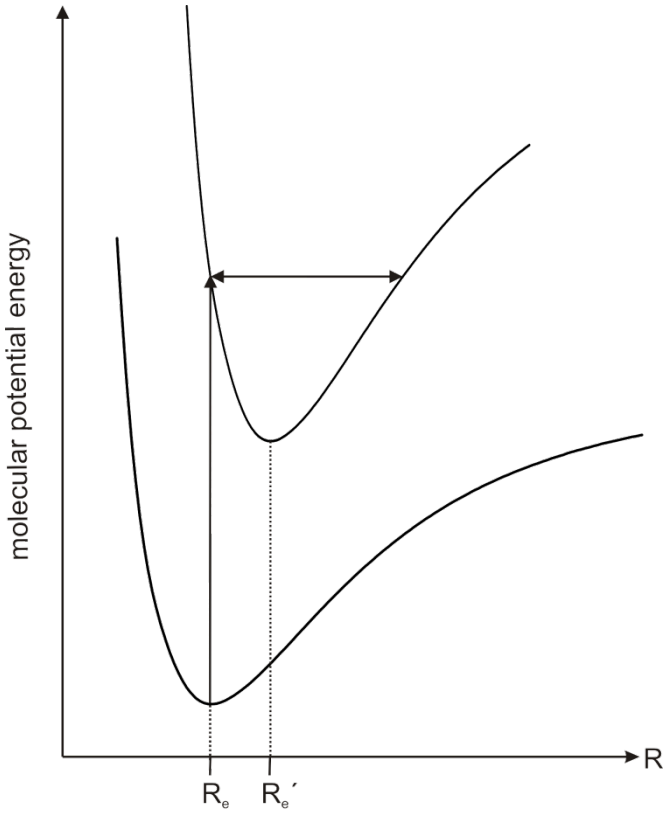

Figure 2.1 Classical description of the Franck-Condon principle.

and therefore *R* increases. For the same reason, the force constants describing the stretch vibration between the nuclei differ. In the classical picture the transition will occur from the minimum in the initial state (lower curve) vertically to the intersection between excitation and final state potential (upper curve). At this point the excited molecule is at a turning point of a vibration and the positions of the nuclei are still the same as they were before the transition. Once the intersection is reached, the molecule starts to vibrate at an energy corresponding to the intersection.

The quantum mechanical description of this process is depicted in figure 2.2. The transition occurs from the vibrational ground state of the initial electronic state potential to the vibrational states in the final electronic state. This way the vibrational wavefunction undergoes the least change, which corresponds to the preservation of the dynamical state of the nuclei as required by the Franck-Condon principle (*i.e.* the position of the nuclei does not change). The vibrational state with a wavefunction that

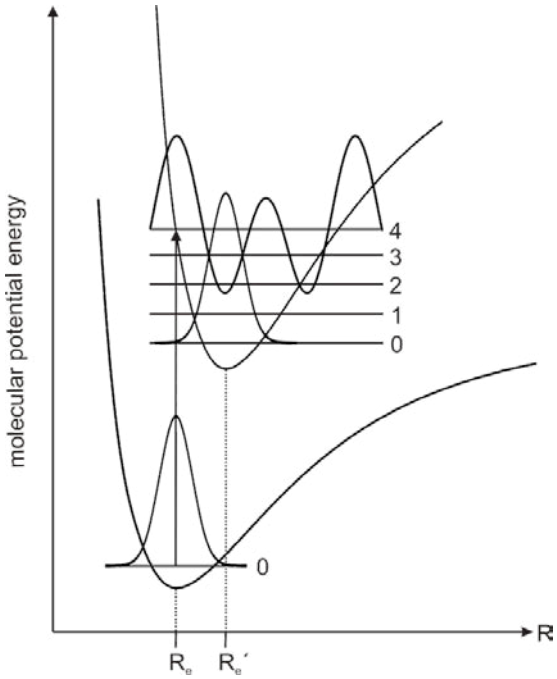

Figure 2.2 Quantum mechanical description of the Franck-Condon principle. The transition occurs from the electronic and vibrational ground state into the electronic and vibrational excited state.

most resembles the original bell-shaped Gaussian of the vibrational ground state is one with a peak immediately above the ground state (*i.e.* maximal overlap between the vibrational levels of ground and excited electronic state). As depicted in figure 2.2 this wavefunction corresponds to an energy level that lays in much the same position as in the vertical transition of the classical description.

To justify the quantum mechanical description the transition dipole moment between the ground vibronic state $|\varepsilon\upsilon\rangle$ and the upper vibronic state $|\varepsilon'\upsilon'\rangle$ has to be evaluated. In a molecule the electric dipole moment operator μ depends on the

position and charges of the electrons, $\vec{r}_i$ and –e, as well as the positions and charges of the nuclei, $\vec{R}_s$ and $Z_s e$:

$$\mu = -e\sum_i \vec{r}_i + e\sum_s Z_s\vec{R}_s = \mu_e + \mu_N \tag{2.24}$$

Within the Born-Oppenheimer approximation, the vibronic state $|\varepsilon\upsilon\rangle$ is described by the wavefunction $\Psi_\varepsilon(\vec{r},\vec{R})\Psi_\upsilon(\vec{R})$, where $\vec{r}$ and $\vec{R}$ denote the electronic and nuclear coordinates, respectively. The transition dipole moment is therefore

$$\begin{aligned}\langle\varepsilon'\upsilon'|\mu|\varepsilon\upsilon\rangle &= \int \Psi^*_{\varepsilon'}(\vec{r},\vec{R})\,\Psi^*_{\upsilon'}(\vec{R})(\overrightarrow{\mu_e}+\overrightarrow{\mu_N})\Psi_\varepsilon\,(\vec{r},\vec{R})\Psi_\upsilon\,(\vec{R})\mathrm{d}\tau_e\mathrm{d}\tau_N \\ &= \Psi^*_{\upsilon'}(\vec{R})\{\int \Psi^*_{\varepsilon'}(\vec{r},\vec{R})\overrightarrow{\mu_e}\,\Psi_\varepsilon\,(\vec{r},\vec{R})\mathrm{d}\tau_e\}\Psi_\upsilon\,(\vec{R})\mathrm{d}\tau_N \\ &\quad +\Psi^*_{\upsilon'}(\vec{R})\overrightarrow{\mu_\upsilon}\{\int \Psi^*_{\varepsilon'}(\vec{r},\vec{R})\,\Psi_\varepsilon\,(\vec{r},\vec{R})\mathrm{d}\tau_e\}\Psi_\upsilon\,(\vec{R})\mathrm{d}\tau_N\end{aligned} \tag{2.25}$$

In the final term the integral over the electronic coordinates is zero because the electronic states are orthogonal to each other for each selected value of $\vec{R}$. The integral over the electron coordinates in the remaining integral is the electric transition dipole moment for the transition when the nuclei have the coordinates $\vec{R}$. Approximately, this transition dipole moment is independent from $\vec{R}$ as long as the displacement of the nuclei from the equilibrium is sufficiently small. If this holds the integral can be approximated by a constant $\overrightarrow{\mu_{e'e}}$ and the overall transition dipole moment can be approximated as

$$\langle\varepsilon'\upsilon'|\vec{\mu}|\varepsilon\upsilon\rangle \approx \overrightarrow{\mu_{e'e}}\int \Psi^*_{\upsilon'}(\vec{R})\Psi_\upsilon\,(\vec{R})\mathrm{d}\tau_N = \overrightarrow{\mu_{e'e}}S(\upsilon',\upsilon) \tag{2.26}$$

where

$$S(\upsilon',\upsilon) = \int \Psi^*_{\upsilon'}(\vec{R})\Psi_\upsilon\,(\vec{R})\mathrm{d}\tau_N \tag{2.27}$$

is the overlap integral between two vibrational states in their respective electronic states. Therefore, the transition dipole moment has the largest absolute value between vibrational states with the largest overlap. Compared to the classical picture this is the quantitative version of the previous qualitative discussion, where the upper vibrational state had a local bell-shaped region above the Gaussian function of the ground vibrational state of the lower electronic state.

Generally, the $S(\upsilon', \upsilon)$ are non-zero. Normally, several vibrational states have significant absolute values of $S(\upsilon', \upsilon)$ and as a consequence transitions take place between all of them and the ground state. The result is a progression of transitions and a series of lines is observed in the electronic spectrum. The square of the transition dipole moments are called Franck-Condon factors, $|S(\upsilon', \upsilon)|^2$, which are directly proportional to the relative intensities of the lines found in the spectrum.

2.1.2.1 Simulation of REMPI Spectra

Simulation of the REMPI spectra are based on Franck-Condon factors as described in Ref.57: First, the normal-mode coordinates and force constants of the ground and excited states are determined. The standard orthogonal normal modes $Q_{1(2)}$ are obtained as a linear combination of Cartesian displacements[58]

$$Q_{1(2)i} = \sum_j L_{1(2)ji} \left(q_{1(2)} - q_{1(2)j}^{(0)} \right). \quad (2.28)$$

Here, the matrix $L_{1(2)}$ connects the 3n - 6 (n is the number of atoms in the (nonlinear) molecule) normal coordinates with the set of 3n mass-weighted Cartesian coordinates $q_{1(2)}$; the vectors $q_1^{(0)}$ and $q_2^{(0)}$ correspond to the stationary points on the adiabatic potential surfaces of states 1 and 2, respectively. Then, the normal modes displacements $\Delta Q_{1(2)}$ are obtained by projecting the displacements $\Delta q = q_1^{(0)} - q_2^{(0)}$ onto the normal-mode vectors.[59] Finally, substituting the calculated quantities into Eq. 2.30 and Eq. 2.29 results in the Huang-Rhys factors[60] S_i and the total relaxation energy λ_{tot}[59]

$$\lambda_{tot} = \sum \lambda_i = \sum \hbar \omega_i S_i \quad (2.29)$$

$$\lambda_i = \frac{k_i}{2} \Delta Q_i^2, \quad (2.30)$$

$$S_i = \lambda_i / \hbar \omega_i. \quad (2.31)$$

The normal modes of ground and excited state, Q_1 and Q_2, are in general different and related by multidimensional rotation and translation,[61]

$$Q_1 = \mathbf{J} Q_2 + \Delta Q. \quad (2.32)$$

The mixing of the normal coordinates of the two states is described by **J**, the Duschinsky matrix. In this work this mixing is neglected (**J** = 1), which is referred to

as the parallel mode approximation.[62] As a consequence the relative intensity of a multidimensional vibrational transition is obtained as a simple product of one-dimensional Franck-Condon integrals,[63]

$$I(m_1, n_1, m_2, n_2, \dots m_p, n_p) = \prod_{i=1}^{p} FCI(m_i, n_i)^2 \exp\left\{\frac{-\hbar m_i \omega_i}{k_B T}\right\}, \quad (2.33)$$

$$FCI(m, n)^2 = \exp(-S) S^{(n-m)} \frac{m!}{n!} \left[L_m^{(n-m)}(S)\right]^2, \quad (2.34)$$

where m_i and n_i are the initial and final vibrational quantum numbers of the mode ω_i, k_B is the Boltzmann constant, T is the temperature, and $L_n^{\alpha}(x)$ is a Laguerre polynomial. The square of the FCI is the Franck-Condon factor (FCF). As we consider only transitions from the vibrational ground state (m = 0) the temperature-averaged FCFs turn into the standard Poisson distribution,[57]

$$I(m = 0, n) = \frac{S^n}{n!} e^{-S}. \quad (2.35)$$

2.1.3 Marcus-Hush Theory

Originally developed (Nobel prize[64] in 1992) by R.A. Marcus in 1956 the Marcus theory[64-72] describes electron transfer in the so called outer-sphere, *i.e.* both reactants do not share an atom or a group, or, more generally, reactions in which the interaction between the relevant orbitals of the two centers is weak. The extension to the description of inner-sphere electron reactions (reactions take place in covalently bound systems) was given by Hush.[73]

Marcus theory can be applied not only for electron transfer, but for exciton transfer as well. To explain the principle we first consider two diabatic (non-interacting) states corresponding to the reactants (A* + B) and products (A + B*) relative to their reaction coordinate R(x), see figure 2.3 for an exergonic reaction. A and B are two different systems (atoms, molecules, …), while the asterix denotes either a charged (excited) species in case of charge (exciton) transport. Reactants and products represent initial state and final state, respectively. To reach the product state the systems have to overcome the barrier $\Delta G^{\neq}$. The reaction free energy is ΔG^0. The central idea in the Marcus treatment is that the activation energy $\Delta G^{\neq}$ can be decomposed into two parts.[74] The first one is characteristic of the reaction type, the

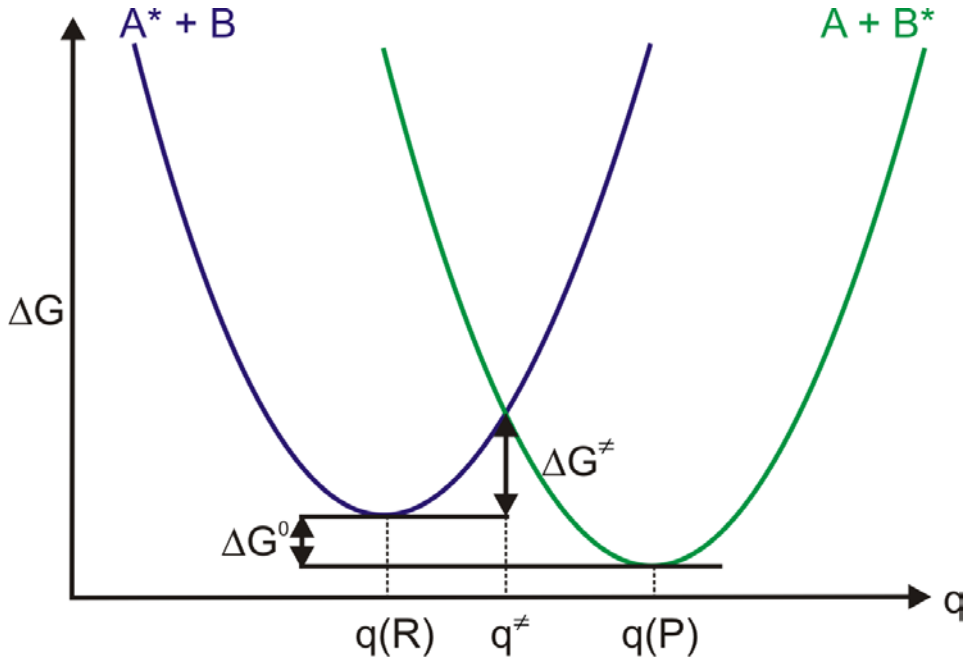

Figure 2.3 Diabatic description of an exciton or charge transfer reaction between two systems A and B. $\Delta G^{\neq}$ represents the reaction barrier and ΔG^{0} is the reaction free energy. The x-axis is the general reaction coordinate represented by the position of the nuclei q, the y-axis represents the free energy.

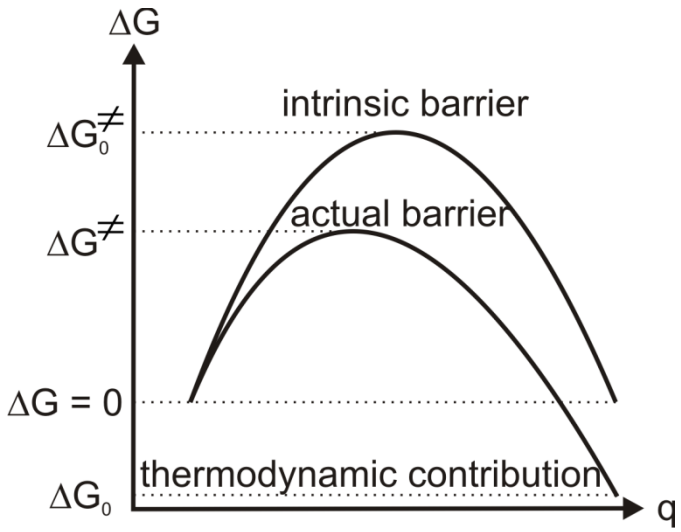

Figure 2.4 Decomposition of the activation energy $\Delta G^{\neq}$ into the intrinsic part as well as the thermodynamic contribution.

intrinsic activation energy $\Delta G_0^{\neq}$, which is gained by a hypothetical thermo neutral reaction ($\Delta G^{0} = 0$). The second part takes into account that reactants and products do not have the same energy and therefore introduces the thermodynamic

correction. This decomposition is depicted in figure 2.4. Similar reactions should have similar intrinsic activation energies, and the Marcus equation obeys both the Bell-Evans-Polanyi principle[75, 76] as well as the Hammond postulate.[77] The barrier can be calculated by

$$\Delta G^{\neq} = \Delta G_0^{\neq} + \frac{\Delta G^0}{2} + \frac{(\Delta G^0)^2}{16\Delta G_0^{\neq}}. \qquad (2.36)$$

Except for very exo- or endothermic reactions (or a very small $\Delta G_0^{\neq}$), the last term in Eq. 2.36 is small and roughly half the reaction energy enters the activation energy. As $\Delta G^{\neq}$ is a parabolic function of the reaction energy, the activation energy will increase if the reaction energy is too exergonic. The turnover occurs at $\Delta G_0 = -4\Delta G_0^{\neq}$. Lower ΔG_0 values correspond to the so called "inverted" region. A comparison between normal and inverted region, as well as their border, where the activation energy is equal to 0 and the reaction rate k gets maximized, is shown in figure 2.5. The inverted region is difficult to access experimentally,[78] but was proven to exist by Closs *et al.* in 1986.[79]

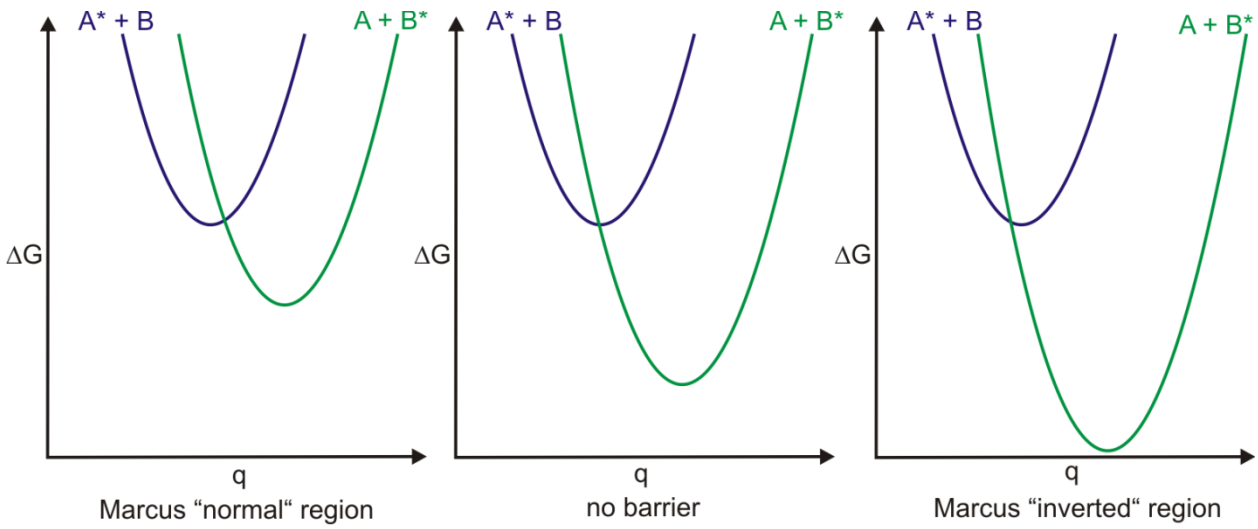

Figure 2.5 Marcus "normal" region (left), the inverted region (right), and the limiting case (middle), where the barrier is 0 and the transfer rate is maximized.

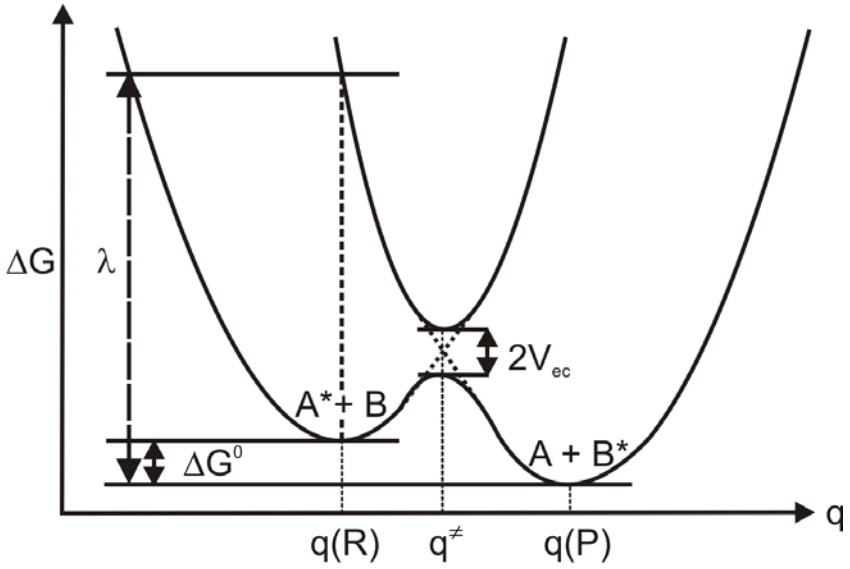

Figure 2.6 Schematic description of the Marcus Theory. The x-axis describes the reaction coordinate represented by the positions R of the nuclei, and the y-axis the free enthalpy G. λ is the relaxation energy, ΔG^0 the Gibbs free energy between reactants and products, and V_{ec} the electronic coupling parameter. The curves represent the adiabatic states of products and reactants.

Since the states have to interact in the case of transfer reactions the description changes from the diabatic to the adiabatic picture, see figure 2.6. This interaction is expressed by V_{ec}, the so called electronic coupling parameter, which is also known as the transfer integral. Its calculation will be discussed in chapter 3. The lower parabola represents the initial reactant state A* + B at q(R) and the final product state A + B* at q(P). λ describes the reorganization energy which is gained by relaxation of the structure after vertical transition from the initial to the final state. Whether the diabatic or adiabatic representation is appropriate depends on the relative magnitude of V_{ec} and λ. This will be explained in detail in section 2.3. In this thesis the semi-classical Marcus Theory rate expression is used which has the form

$$k = \frac{|V_{ec}|^2}{\hbar}\sqrt{\frac{\pi}{\lambda k_B T}}\exp\left(-\frac{(\lambda+\Delta G^\circ)^2}{4\lambda k_B T}\right), \qquad (2.37)$$

with k_B as the Boltzmann constant, and T as the absolute temperature. It can be derived from Fermi´s Golden Rule and will be explained in the next subsection.

2.1.3.1 Derivation of the Semi-Classical Marcus Rate Equation

It is assumed that

- all normal modes are classical ($\hbar\omega_i \ll k_B T$).
- the potential energy surfaces of an initial reactant (R) state to a final product (P) state have a parabolic form and have the same vibrational frequencies:

  $E_R(q) = E_R(0) + \frac{1}{2}\omega_0\left(q - q(R)\right)^2$ and $E_P(q) = E_P(0) + \frac{1}{2}\omega_0\left(q - q(P)\right)^2$. (2.38)

  the thermal equilibrium is reached and the distribution of the initial states is given by:

  $$f(q) = \frac{1}{Z}\exp\left(-\frac{E_R(q)}{k_B T}\right), \quad (2.39)$$

  with Z being a partition function.

If these conditions apply, Fermi´s Golden Rule (Eq. 2.22) can be rewritten as an ensemble average:

$$k = \frac{2\pi}{\hbar}\int dq\, f(q)|V_{ec}|^2\delta(E_R(q) - E_P(q)). \quad (2.40)$$

Evaluation of Z in Eq. 2.40 gives

$$Z = \int_{-\infty}^{+\infty} dq\, \exp\left(-\frac{1}{2}\omega_0^2(q - q(R))^2\right). \quad (2.41)$$

Substituting $x = \sqrt{\frac{\omega_0^2}{k_B T}}(q - q(R))$, Eq. 2.41 becomes

$$Z = \sqrt{\frac{k_B T}{\omega_0^2}}\int_{-\infty}^{+\infty} dx\, \exp\left(-\frac{x^2}{2}\right) = \sqrt{\frac{2\pi k_B T}{\omega_0^2}} \quad (2.42)$$

The argument of the delta function in Eq. 2.40 can be rewritten as

$$E_R(q) - E_P(q) = \Delta G^0 + \frac{\omega_0^2}{2}[q^2 - 2q(R)q + q^2(R) - q^2 + 2q(P)q + q^2(P)] \quad (2.43)$$

with $\Delta G^0 = E_R(0) - E_P(0)$ (2.44)

$$E_R(q) - E_P(q) = \Delta G^0 - \omega_0^2 q(q(R) - q(P)) + \frac{\omega_0^2}{2}\left(q^2(R) - q^2(P)\right) \quad (2.45)$$

Eq. 2.45 is linear in the normal mode coordinate q. The coordinate $q^{\neq}$, where the diabatic surfaces of R and P cross $(E_R(q) = E_P(q))$, is expressed as

$$q^{\neq} = \frac{\Delta G^0 + \frac{\omega_0^2}{2}\left(q^2(R) - q^2(P)\right)}{\omega_0^2 q(q(R) - q(P))}. \tag{2.46}$$

A delta function can be written in general as

$$\delta\big(f(x)\big) = \sum_i \frac{\delta(x - x_i)}{|f'(x_i)|}. \tag{2.47}$$

This property allows us to rewrite the delta function of Eq. 2.40 as

$$\delta\big(E_R(q) - E_P(q)\big) = \frac{\delta(q - q^{\neq})}{\omega_0^2(q(R) - q(P))}. \tag{2.49}$$

Combining Eq. 2.42 and Eq. 2.48, Eq. 2.40 becomes

$$k = \frac{2\pi}{\hbar}\sqrt{\frac{\omega_0^2}{2\pi k_B T}}\frac{|V_{ec}|^2}{\omega_0^2(q(R) - q(P))}\int_{-\infty}^{+\infty} dq\, \exp\left(-\frac{\omega_0^2(q - q(R))^2}{2k_B T}\right)\delta(q - q^{\neq}) \tag{2.49}$$

$$<=> k = \frac{2\pi}{\hbar}\frac{|V_{ec}|^2}{\sqrt{2\pi k_B T \omega_0^2 (q(R) - q(P))^2}}\exp\left(-\frac{\omega_0^2(q^{\neq} - q(R))^2}{2k_B T}\right). \tag{2.50}$$

Inserting the reorganization energy λ and the activation barrier $\Delta G^{\neq}$ to replace reactant and product coordinates as

$$\lambda = \frac{\omega_0^2}{2}\big(q(R) - q(P)\big)^2 \tag{2.51}$$

$$\Delta G^{\neq} = \frac{1}{2}\omega_0^2\big(q^{\neq} - q(R)\big)^2 \tag{2.52}$$

$$\Delta G^{\neq} = \frac{\big(\Delta G^0 + \lambda\big)^2}{4\lambda} \tag{2.53}$$

into Eq. 2.50 we finally obtain Eq. 2.37

$$k = \frac{|V_{ec}|^2}{\hbar}\sqrt{\frac{\pi}{\lambda k_B T}}\exp\left(-\frac{(\lambda + \Delta G^{\circ})^2}{4\lambda k_B T}\right).$$

2.1.3.2 Calculation of the Reorganization Energy

The reorganization energy λ is the quantity to describe the system reorganizing during the charge or exciton transfer. λ can be decomposed into an internal (λ_{int}) and an external (λ_{ext}) reorganization energy.

The latter represents the surroundings of the interacting systems. If the transfer takes place in the condensed phase, λ_{ext} is associated to the change of the nuclear polarization of the solvent. Marcus developed a model in the 1960´s for charge transfer, which is based on the hypothesis that the medium around molecules A and B is a dielectric continuum. There, the external reorganization energy can be written[71]

$$\lambda_{ext} = \frac{(\Delta e)^2}{2}\left(\frac{1}{\varepsilon_{opt}} - \frac{1}{\varepsilon_s}\right)\left(\frac{1}{r_A} + \frac{1}{r_B} - \frac{2}{R_{AB}}\right) \qquad (2.54)$$

where Δe is the amount of charge transferred, ε_{opt} and ε_s are the optical and static dielectric constant of the medium, r_A and r_B are the radius of the molecules A and B, which are considered as two spherical ions, and R_{AB} is the distance between them.

In the solid state the external reorganization is related to the complete electronic and nuclear depolarization of the molecules in the surrounding of the molecular ion in the initial state and their polarization of the final state after charge transfer. A systematic way of evaluating λ_{ext} has proven difficult due to the complexity of nuclear and electronic degrees of freedom. Therefore, in this work which focuses on crystalline systems, the external reorganization energy has been neglected. This is supported by the results of Norton *et al.*[80] and McMahon *et al.*,[81] who showed that λ_{ext} is smaller by one order of magnitude than λ_{int} in oligoacenes. Furthermore, λ_{int} of a molecule is smaller in a cluster than in the gas phase.[80] Thus, the neglect of the external reorganization energy is compensated by the overestimated internal relaxation energy calculated in the gas phase. [34]

The internal reorganization energy λ_{int} is decomposed into two parts,[57] which are both shown in figure 2.7. λ_1 corresponds to the relaxation of the molecule A* after vertical transition from the neutral (ground) state A into the charged (excited) state A* and λ_2 is the corresponding term for relaxation after the vertical transition back from A* to A. Thus, the internal reorganization energy is just the sum over both parts:

$$\lambda_{\text{int}} = \lambda_1 + \lambda_2. \tag{2.55}$$

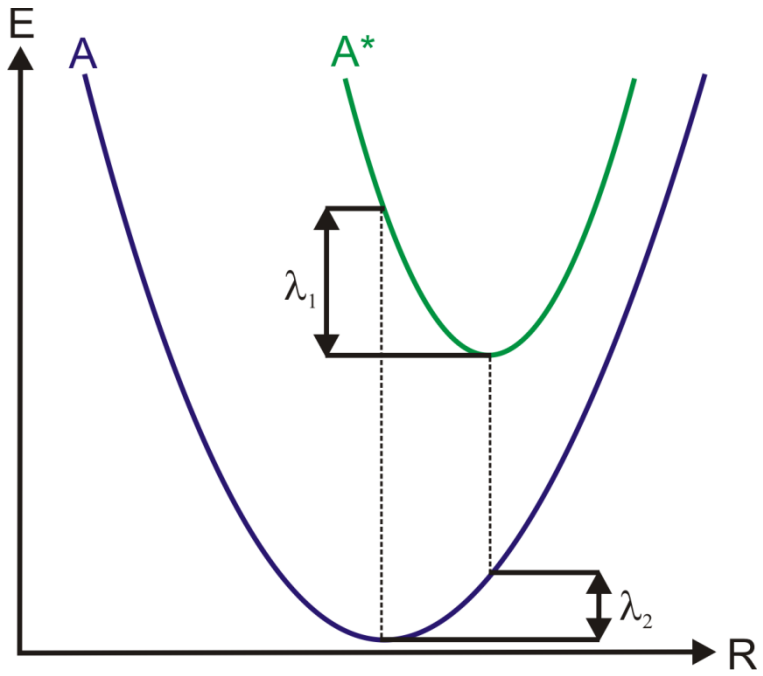

Figure 2.7 Internal relaxation energy λ_{int} decomposed into its two parts λ_1 and λ_2. A is the system in the ground (neutral) state and A* the system in the corresponding excited (charged) state in case of exciton (charge) transfer.

2.2 Exciton Transport

To describe exciton transport in organic materials, one of the major bottlenecks in the efficiency of organic solar cells, one has to understand first the concept of an exciton, which originates from solid state theory (section 2.2.1.1). The interaction between an exciton and its neighbored molecules is intimately related to the phenomenon of the Davydov splitting (section 2.2.2). The transport itself adopts the ideas of charge transport (chapter 2.3) as it uses the semi-classical Marcus theory for hopping transport (section 2.1.3.2) in a weak coupling regime (section 2.4).

2.2.1 Exciton Theory

The ideal exciton is a quantum of electronic excitation energy without any charge.[82] It is created whenever a system (complex, cluster, nanoparticle, or crystal) absorbs light. Excitons travel through crystals transporting energy, but not charge.[83] Therefore, their movement is unaffected by external fields. Different types of excitons

exist and the present work will focus on those called after the description by Frenkel[83] and Wannier,[84] while also introducing the Davydov exciton, a special subclass of the Frenkel-type.

Excitons are affected by lattice vibrations. If the thermal energy kT is comparable with the binding energy of the exciton, then it can be “ionized” to produce a negatively charged particle or a positively charged hole. These are charge carriers and therefore responsible for electric currents. If light is absorbed under these thermal conditions the conductivity of the crystal will increase. This effect is known as photoconductivity. There are also others ways to ionize an exciton: A real crystal shows a large number of imperfections like vacancies, interstitial defects, dislocations, foreign atoms and even the surfaces of the crystal. All of them perturb the perfect periodicity of the lattice. There, an exciton can ionize and photoconductivity is observed as a result. Another possibility is the collision of two excitons, but this is highly improbable without the use of laser beams. Excitons in solids can dissipate in three different ways: Conversion into heat through coupling with lattice vibrations, transformation into free charges (ionizations), and by emission of light (fluorescence, phosphorescence).

Finally, it should be emphasized, that excitons can only be understood by quantum theory: An exciton is a quantum of excitation and hence a pseudoparticle. Many other forms of quantized excitations exist, among them lattice vibrations, which have the greatest influence on excitons. The coupling between both gives rise to the so called exciton-phonon complex.

2.2.1.1 Frenkel Exciton

First by Frenkel[83] in 1931 and Peierls[85] in 1932, the exciton was introduced as “excitation waves”, which are formed in solids by light absorption and subsequently transform into heat. In these simple solids the interaction between electrons from neighboring atoms or ions is small compared to the attraction between electrons and cores within the individual atoms. Examples for these kinds of solids are solid xenon and sodium chloride. Having a inert gas configuration, the shells within each atom are always full and the electrons do not interact a lot with other atoms or ions as long as they remain within the closed shells. As a consequence, the material does not conduct electric current, *i.e.* it is an insulator. If one atom absorbs enough energy

(*e.g.* a photon), then an electron is moved out of the closed shells, but is still bound to its parent atom/ion. This electron is now moving within the space influenced by the positive charge field created by its own absence from its original closed shell. The latter is called “hole” and is treated in solid state physics like an electron except for its positive charge. This electron-hole pair is not bound to any particular atom, but can pass from one atom to the next in the crystal, constituting what Frenkel called an “excitation wave” or simply exciton. Its movement does not result in a net flow of charge. The electron is still bound by Coulombic force to the hole and the distance between them is called the “exciton radius”. This radius is considered to be small in Frenkel excitons (therefore the alternative name zero-radius exciton), i.e. less than the interatomic distance. Electron and hole are tightly bound and localized, see figure 2.8.

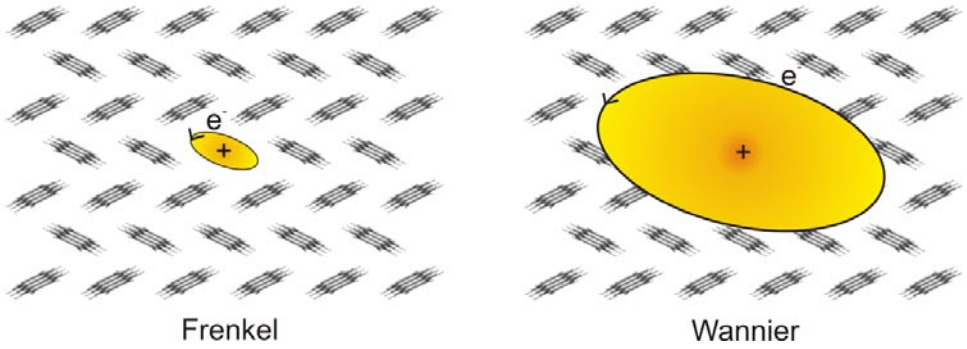

Figure 2.8 Localized Frenkel-type exciton (left) and delocalized Wannier-type exciton (right).

2.2.1.2 Mott-Wannier Exciton

A similar, yet slightly different approach was given by Wannier[84] and Mott[86] for excitons with large radius, resulting in the alternative name large-radius exciton, and for solids, where the valence atoms cannot be identified to their parent atoms anymore. This is the case for many semiconductors, in particular the so called covalent solids such as germanium, silicon, gallium arsenide and cuprous oxide etc. There, the interaction between neighboring atoms is increased and the valence electrons are normally shared by several atoms to form bonds. Although the electrons have gained a greater spatial volume in which they can move, they are still not contributing to electric current, even if an external field is applied. In such solids the valence electrons occupy the valence band and a conduction band is found

energetically above. If the interaction between neighboring atoms is increased, so will the extent of the valence band. Additionally, the gap between both bands decreases. Ionic solids are therefore just the limiting case with a large gap and a narrow valence band. If one electron gets excited in such a semiconductor, it will leave a positive hole of the valence band. This hole will attract the electron to form an exciton, which binds much weaker than an electron in the valence band. The exciton radius is large and can cover up to tens or hundreds of atomic sites.

2.2.1.3 Davydov Exciton

A formerly third type of exciton is known by the name “Davydov exciton”, which are found in organic substances with ring units such as benzene and anthracene.[82] The ring systems as a whole are excited by the absorption of light and the excitation energy is delocalized over the complete molecule. The excitation energy can also be passed on from one ring to another. The small interaction between neighboring rings is small compared with the interatomic forces within the ring. Therefore, Davydov excitons are localized and resemble Frenkel excitons.

2.2.2 Davydov Splitting

Based on the first investigations of excitons in molecular crystals[87-89] Davydov was the first who developed the exciton theory for molecular crystals.[90, 91] For this thesis it is sufficient to describe the simplest system for which exciton effects can be considered: the excitonically coupled dimer. The principles described here can be extrapolated to molecular aggregates.

The excitonically coupled dimer consists of two monomer subunits. They don´t have to be within the van-der-Waals radius, or chemically linked via bonds. Both molecules are fixed in space for a given distance R_{12} and do not have any surroundings. Both are considered to have only two energy levels. For a given Hamiltonian $\hat{H}$ their eigenstates ψ^i are determined by

$$\hat{H}\psi_n^i = \varepsilon_n^i \psi_n^i, \tag{2.56}$$

where the subscript n defines the subsystem and the superscript i refers to ground and excited state. Since we assume both subunits to be identical we omit the subscript: ε^i . Furthermore, the ground state energy is set to zero.

The total Hamiltonian for interacting molecules (Coulombic interaction) includes besides $\hat{H}_1$ and $\hat{H}_2$ also the interaction V between them. In this case ψ_1 and ψ_2 are no longer the correct eigenstates and also the eigenenergies will be different, *i.e.* interaction of the molecules will result in perturbations of the energy spectrum. Since this interaction is weak, the perturbation theory for degenerate states can be used with the Heitler-London approximation:[91] Linear combinations of the product of the molecular eigenfunctions are equal to the eigenfunctions of the dimer. We describe the electronic ground state for the dimer as $\Psi^0 = \psi_1^0\psi_2^0$. The leads to the corresponding ground state energy of the dimer as

$$E^0 = \langle\psi_1^0\psi_2^0|\hat{H}_1 + \hat{H}_2 + V|\psi_1^0\psi_2^0\rangle = \varepsilon_1^i + \varepsilon_2^i + \langle\psi_1^0\psi_2^0|V|\psi_1^0\psi_2^0\rangle = V_{00}. \quad (2.57)$$

The coupling between the molecules can already lead to a change in the ground state energy by V_{00}. The excited states are written as

$$\Psi^f = c_{f1}\psi_1^1\psi_2^0 + c_{f2}\psi_1^0\psi_2^1. \quad (2.58)$$

The coefficients c_{f1} and c_{f2} are normalized and orthogonal:

$$c_{f1}^2 + c_{f2}^2 = 1$$

$$c_{f1} \cdot c_{g1} + c_{f2} \cdot c_{g2} = 0, \quad (2.59)$$

where f and g represent different eigenstates. Thus, the excited state of the dimer is a linear combination of two terms in which one or the other molecule is excited. The coefficients $c_{f1,2}$ determine the relative contributions of these two terms. Also, the dimer eigenstates must fulfill the Schrödinger equation:

$$(\hat{H}_1 + \hat{H}_2 + V)\Psi^f = E^f\Psi^f. \quad (2.60)$$

By multiplication from the left with either $\psi_1^1\psi_2^0$ or $\psi_1^0\psi_2^1$ and integration over the entire space gives the two equations:

$$c_{f1}(\varepsilon_1^1 + \langle\psi_1^1\psi_2^0|V|\psi_1^1\psi_2^0\rangle) + c_{f2}\langle\psi_1^1\psi_2^0|V|\psi_1^0\psi_2^1\rangle = c_{f1}E^f, \quad (2.61)$$

$$c_{f1}\langle\psi_1^0\psi_2^1|V|\psi_1^1\psi_2^0\rangle + c_{f2}(\varepsilon_2^1\langle\psi_1^0\psi_2^1|V|\psi_1^0\psi_2^1\rangle) = c_{f2}E^f, \quad (2.62)$$

or abbreviated as

$$c_{f1}\left(\varepsilon_1^1 + V_{11} - E^f\right) + c_{f2}V_{12} = 0, \tag{2.63}$$

$$c_{f2}V_{21} + c_{f2}\left(\varepsilon_2^1 + V_{22} - E^f\right) = 0. \tag{2.64}$$

V_{12} and V_{21} are resonance interaction terms, also called the electronic coupling parameter (called V_{ec} in this thesis) or transfer integral. Rewriting this into a determinant gives for non-trivial solutions (c_{f1} and c_{f2} should not both be equal to 0):

$$\begin{vmatrix} \varepsilon_1^1 + V_{11} - E^f & V_{12} \\ V_{21} & \varepsilon_2^1 + V_{22} - E^f \end{vmatrix} = 0. \tag{2.65}$$

Since both molecules are identical $\varepsilon_1^{0,1} = \varepsilon_2^{0,1} = \varepsilon^{0,1}$, $V_{12} = V_{21}$ and $V_{11} = V_{22}$. Thus Eq. 2.65 can be written as

$$\left(\varepsilon^1 + V_{11} - E^f\right)^2 = {V_{12}}^2 \tag{2.66}$$

which gives the two eigenenergies

$$E^1 = \varepsilon^1 + V_{11} - V_{12},$$

$$E^2 = \varepsilon^1 + V_{11} + V_{12}. \tag{2.68}$$

The excitation energy has changed going from the monomer to the dimer. The energy levels are split by $2V_{12}$. This effect is known as Davydov splitting or exciton splitting. The average energy of these two levels has been shifted with respect to the monomer ground state by $V_{11} - V_{00}$, which is also called displacement energy D. This D is comparable to the change a molecule experiences when it goes from the gas phase to its condensed phase surrounding, which usually leads to a red shift of the absorption bands.

The value of the resonance interaction V_{12} can be evaluated by transition dipole moments (chapter 3.1.1), the Coulomb interaction between transition densities of two monomers (chapter 3.1.3) or by calculation of the complete dimer system (chapter 3.1.4).

The above molecule is of course oversimplified. In this description the energy levels of the two molecules do not have to be identical (non-equivalent site energies). Mixing with other excited states, the influence of internal and

environmental vibrations (*e.g.* phonons in crystals), and different broadening mechanisms are not considered.

2.3 Charge Transport

In charge transport (CT) either a positive hole or a negative electron is transferred from an initial electronic state (donor, reactant) to a final state (acceptor, product). Each of these states is characterized by its own vibronic states. The main focus of this thesis is CT in bimolecular systems. This is governed by a balance between the electronic and nuclear motion, which corresponds to the electronic and nuclear frequency ν_{el} and ν_{nuc}. Taking the inverse of these provides the vibrational and electronic characteristic times, t_{el} and t_n, respectively. The two limits $t_n \gg t_{el}$ and $t_n \ll t_{el}$are referred to as the strong coupling regime and the weak coupling regime.[60]

- In the strong coupling regime, also termed adiabatic limit, the electronic states are delocalized over the whole donor-acceptor complex and $V_{ec} \gtrsim \lambda$ (or $V_{ec} > \hbar\omega$). To be more specific: The initial state is partially delocalized over the final state. There, the use of the double-well delocalized adiabatic representation is advantageous, see figure 2.6. The adiabatic transfer is understood as the vibrational degrees of freedom when the system moves from one energy well to the other. Here, the rate constant can be obtained by a standard Arrhenius-type equation neglecting the electronic coupling.
- In the weak coupling regime, also termed non-adiabatic charge transfer ($V_{ec} < \lambda$ by several orders of magnitude), the vibrational motion is much faster than the electronic motion ($\nu_{nuc} \gg \nu_{el}$). The electronic states are localized and a description based on diabatic initial and final states is appropriate. The crossing point between the initial and the final state can easily be reached, but the transmission is limited by the electronic frequency. This is the case for all investigated systems in this thesis.
- In case of $V_{ec} > \lambda$ it is impossible to distinguish between reactant and product as the electronic states are fully delocalized over the systems.

2.4 Diffusion

Diffusion is a process which leads to an equal distribution of particles in a given volume. The basis is the thermal motion of particles, which can be either atoms, molecules or charge carriers. Statistically, diffusion describes particles moving from areas of higher concentration into areas with lower concentration, but diffusion itself also happens if there is no concentration gradient. Therefore, diffusion occurs without a preferred direction. It normally applies on scales of nano- to millimeters. If the distances are greater, then convection dominates transport of matter in liquids and gas. In physics diffusion is divided into four different types:[92]

- classical Fick diffusion

  A strong concentration gradient exists. Particles move from the area of high concentration into the area of low concentration. Diffusion is described mathematically by Fick´s First and Second law:

  $$J = -D\frac{\delta c}{\delta x} \tag{2.69}$$

  $$\frac{\delta c}{\delta t} = D\frac{\delta^2 c}{\delta x^2} \tag{2.70}$$

  with J as the flux, c as concentration, x is the considered direction, t the time, and D the diffusion constant.

- counter-diffusion

  This type is in principal identical to the classical treatment by Fick. The difference arises as counter-diffusion also incorporates a second concentration gradient which leads to diffusion in opposing directions.

- self-diffusion

  In the absence of any concentration gradients (*e.g.* pure water) particles move randomly without any preferred direction. This model is applicable to describe Brownian motion. In crystals, the self diffusion constant is given by

  $$D = \lim_{t\to\infty} \frac{1}{2dt} \sum_i p_i(t)(r_i - r_0)^2, \tag{2.71}$$

  where p_i denotes the probability that the lattice site i is occupied by a charge carrier or exciton and $|r_i - r_0|$ is the distance between the lattice site i and the origin of the system. Diffusion lengths L_D are obtained by

  $$L_D = \sqrt{2D\tau} \tag{2.72}$$

with τ as the lifetime. Since this thesis neglects the interaction with other particles self-diffusion is the best model to describe exciton and charge transport. Although the gradient is missing self diffusion in crystals is subject to anisotropy, which will be discussed in more detail in chapter 4.

- tracer-diffusion
  This type is similar to self-diffusion, but this time the considered moving particle (called tracer) is found for low concentration solvated in another substance, *e.g.* small amounts of KCl in a solution of NaCl in water. The tracer is usually marked with a radioactive isotope or able to fluoresce.

To calculate the diffusion constant D several models are possible. The easiest way is derived from the kinetic gas theory as[93]

$$D = \frac{1}{3}\langle x\rangle\langle \nu\rangle, \tag{2.73}$$

where $\langle x\rangle$ is the average length a particle moves until it collides with another one and $\langle \nu\rangle$ its corresponding average velocity. The derivation of Eq. 2.73 assumes an ideal gas. Its particles move without interaction with their neighbors. Therefore, these particles do not change their direction and Eq. 2.73 represents only an upper boundary for diffusion.

In the case of hopping transport in organic crystals (this thesis), Eq. 2.73 is not directly applicable as transport takes place between single systems carrying the exciton (or charge) and their neighbors. *E.g.* the pathway of a given exciton (or charge carriers) along a cell axis in crystals is composed of a straight direction along this axis and all other combinations (zig-zag motion or random motion), which will ultimately lead the exciton (or charge carrier) into the same direction, see figure 2.9. Taking these motions into account requires a more general approach for hopping transport. The following sections summarize the approach presented in more detail in Ref.94, which employs the master equation, which, in the case of low charge-carrier densities, has the form

$$\frac{dp_i}{dt} = \sum_j \left(\nu_{ij} p_j - \nu_{ji} p_i\right) \tag{2.74}$$

where p_i denotes the probability that the lattice site i is occupied by a charge carrier.

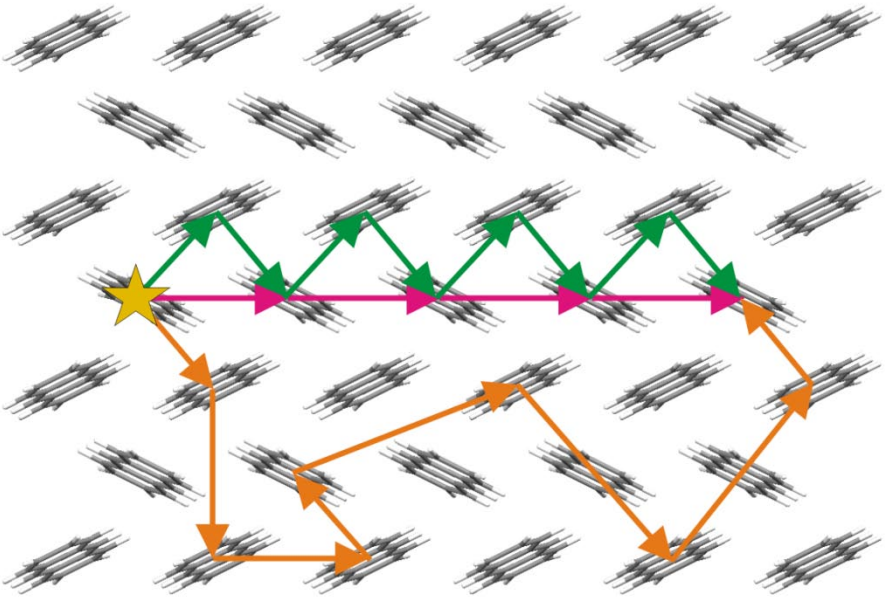

Figure 2.9 Different possibilities for an exciton or charge carrier (star) to travel along the cell axis b in the anthracene crystal: straight (pink), zig-zag (green) or random (orange).

The index j represents a given neighbored system, where excitons (or charge carriers) can be transported to or from. Although it is possible to include repulsive interaction between charge carriers in the master equation, Eq. 2.74 gives good results in the case of low densities.

Under steady state conditions, the occupation probabilities do not change anymore ($dp_i/dt = 0$) as a dynamic equilibrium is reached. The result is a linear system of equations of the form

$$\mathbf{N} \cdot \vec{p} = \vec{0} \tag{2.75}$$

with $\vec{p}$ containing the unknown p_i and **N** is a negative semidefinite sparse matrix which contains all hopping rates ν_{ij}. **N** is approximated by a finite matrix with cyclic boundary conditions, *i.e.* if a charge carrier (or exciton) leaves the crystal at one side then it reenters at the opposite site. Note that this approximation results in a constraint. The probability for this kind of jump must be very small to avoid wrong occupation numbers. Therefore, the matrix must be big enough. This is accomplished for our systems if we choose our crystal to be a cube of three unit cells

in each direction. Bigger matrices do not change the results for charge transport.[94] Hopping rates have been calculated from all monomers in one unit cell to all other monomers in the same and the adjacent cells. Since the semi-classical Marcus rate expression (Eq. 2.37) to obtain the jump rates k depends strongly on the distance via the coupling V_{ec}, larger jump distances can be neglected.

Taking into account the normalization condition $\sum_i p_i = 1$ Eq. 2.75 results in the occupation probabilities for all sites (if we assume $\Delta G^0 = 0$ for all site combinations). With these probabilities the mobilities μ can be calculated in field direction from

$$\mu = \frac{\langle v \rangle}{F} \tag{2.76}$$

with F as the electric field, $\langle v \rangle$ as the average velocity

$$\langle v \rangle = \sum_i p_i \nu_i = \sum_i p_i \frac{\langle r_{||} \rangle}{\tau_i}, \tag{2.77}$$

where v_i is the resulting average velocity at site i,

$$\langle r_{||} \rangle_i = \frac{\sum_j \nu_{ji} \left(\vec{r}_{ji} \frac{\vec{F}}{F} \right)}{\sum_j \nu_{ji}} \tag{2.78}$$

is the average displacement at site i in field direction, and

$$\tau_i = \left(\sum_j \nu_{ji} \right) \tag{2.79}$$

is the dwell time of the charge carrier (or exciton) at site i. Combining Eqs. 2.76 to 2.79 gives the mobility as

$$\mu = \frac{1}{F} \sum_i \left(p_i \sum_j \nu_{ji} \frac{\sum_j \nu_{ji} \left(\vec{r}_{ji} \frac{\vec{F}}{F} \right)}{\sum_j \nu_{ji}} \right) = \frac{1}{F} \sum_{ij} p_i \nu_{ji} \vec{r}_{ji} \frac{\vec{F}}{F}. \tag{2.80}$$

A different and easier approach to the mobility is a calculation without an external field. Then, the occupation probabilities of the sites are equal and the master equation does not have to be solved. Eq. 2.80 is not resolvable (because F = 0) and the mobility is calculated via the diffusion constant D and the Einstein relation[95]

$$\mu = \frac{q}{k_B T} D, \tag{2.81}$$

where k_B is the Boltzmann constant and, T the absolute temperature, and q the charge. Apart from Eq. 2.73 different approaches exist to evaulate D.[96-100] Following the concepts for the mobility above provides

$$D = \frac{1}{2n}\frac{d}{dt}\langle r^2\rangle = \frac{1}{2n}\sum_i p_i \frac{\langle r^2\rangle_i}{\tau_i}, \tag{2.82}$$

where n is the spatial dimensionality. If the diffusion is regarded in one dimension only, then n = 1 and

$$D = \frac{1}{2}\sum_i p_i \frac{\langle r_{||}^2\rangle_i}{\tau_i} \tag{2.83}$$

where

$$\langle r_{||}^2\rangle_i = \frac{\sum_j \nu_{ji}\left(\vec{r}_{ji}\vec{e}\right)}{\sum_j \nu_{ji}} \tag{2.84}$$

is the variance of the charge carrier position at site i in the direction of the unit vector $\vec{e}$. These equations lead to

$$D = \frac{1}{2}\sum_{ij} p_i \nu_{ji}\left(\vec{r}_{ji}\vec{e}\right)^2. \tag{2.85}$$

Without an external field (F = 0) and identical site energies ($\Delta G^0 = 0$) Eq. 2.85 turns into

$$D = \frac{1}{2}\sum_{ij} \nu_i\left(\vec{r}_j\vec{e}\right)^2. \tag{2.86}$$

As shown in more detail in Ref.94 Eqs. 2.85 and 2.86 are not strictly correct. Only if the unit cell of the crystal contains a single molecule and only if the crystal structure has a perfect translation symmetry (*i.e.* $G_i^0 = G_j^0 <=> \Delta G_{ij}^0 = 0$), then those equations are correct. Less ordered or amorphous materials have different site energies G_i^0 and G_j^0 due to the surroundings of their lattice site. Consequently, the occupation numbers p_i differ and the master equation has to be applied. If ΔG_{ij}^0 is too big the charge carrier (or exciton) may be trapped between two lattice sides with similar energy and Eq. 2.85 becomes inapplicable. The charge carrier (or exciton) hops between those two sites until all the time. This does not contribute to the macroscopic spread of the occupation probability with the time. The true macroscopic diffusion constant is overestimated by the averaging in Eq. 2.85. This

problem does not occur in Eq. 2.80, because $\vec{r}_{ji}$ is not squared in contrast to Eq. 2.85 and the contribution of the trapped charge carrier to the diffusion cancels when summed over all lattice sites. Another problem exists even in perfect crystals: If the coupling and consequently the transfer rate in a specific dimer is high in comparison to all its neighbors, then the charge carrier (or exciton) will also move back and forth. This also leads to an overestimation of D by application of Eqs. 2.85 and 2.86 and a combination of Eqs. 2.80 and 2.81 is necessary to get the correct values for the diffusion constant.[94]

Another possibility to calculate the mobility and the diffusion constant is a Monte Carlo approach.[101] Neglecting the interaction between charge carriers (or excitons) gives

$$\mu = \frac{1}{F}\frac{d}{dt}\langle \vec{r}_{ji}\frac{\vec{F}}{F}\rangle \tag{2.87}$$

and

$$D = \frac{1}{2}\frac{d}{dt}\langle\left(\vec{r}_{ji}\vec{e} - \langle\vec{r}_{ji}\vec{e}\rangle\right)^2\rangle. \tag{2.88}$$

To obtain smooth lines the time-dependent average position $\langle \vec{r}_{ji}\frac{\vec{F}}{F}\rangle$ and the variance $\langle\left(\vec{r}_{ji}\vec{e} - \langle\vec{r}_{ji}\vec{e}\rangle\right)^2\rangle$ are averaged over a sufficient number of simulations. This approach is an alternative to solve the master equation. It is a feasible way to log motions at the atomic scale underlying the transport properties as a function of time. However, many simulations are necessary for this statistical method to get an acceptably low statistical error. Additionally, it must be confirmed that the stationary state being reached within the simulation time. In case of strongly disordered systems this is a serious problem. In contrast to Monte Carlo the previous approach is numerically more efficient, because it provides the stationary state by means of an analytic numerical methods.[102]

The validity of the Einstein relation has been called into question for disordered organic materials in general[100, 103, 104] or at least if an external field is applied.[105-107] It turned out that this is only true for rather high charge-carrier densities,[108] low temperatures and high electric fields. This is not the case in the systems under consideration in this work. Extremely low temperature causes the charge carriers

(or excitons) to not being able to reach sites with higher energy. The thermal energy needed as activation is insufficient and only transfer to sites with lower energy is possible. Mobility and diffusion constant is then temperature independent.[109] The transport coefficients are independent on the field,[110, 111] for small fields, but for higher fields nonlinear effects become important and D/μ increases with the field.[112]

2.5 Band Transport

Although not a topic in this thesis, band theory is a common concept used to describe transport in metallic and inorganic semiconductors.[113] Originally developed by Bloch[114] in 1928 to calculate the electronic structure, band theory describes crystals as being constituted by atoms or molecules regularly positioned in space to form a periodic lattice. These sites are fixed in space and electrons moving within the crystal are hardly influenced by the nuclei. As a consequence, electrons scatter only weakly on their way through the crystal. In this case, the energies and wavefunctions are obtained by considering that the movement of the electrons is influenced by the potential V(r) of the fixed nuclei (Born-Oppenheimer). Another approximation is that each electron at position r is subject to a potential V(r) which takes into account the attraction of the nuclei and the repulsion of all the other electrons. Finally, the problem is reduced to a one-electron problem where electrons are considered independent moving in a potential with the periodicity of the crystal. The stationary states of these electrons are delocalized over the whole crystal. These states are the so-called called Bloch functions and the probability to find an electron is distributed over the whole crystal.

Assuming an infinite linear atomic chain where only nearest neighbor interactions are considered, a tight-binding Hamiltonian describes the system:

$$H = E_0 + \sum_q |\varphi_q\rangle V_{ec} \langle\varphi_{q+1}| + \sum_q |\varphi_q\rangle V_{ec} \langle\varphi_{q-1}| \qquad (2.89)$$

where E_0 is the atomic site energy and V_{ec} is the electronic coupling or transfer integral (see chapter 3). The energies of the Bloch functions are given by:

$$E(k) = E_0 - 2V_{ec}\cos(kR_a) \qquad (2.90)$$

with k as wave factor and R_a as the interatomic distance in the chain.

Eq. 2.90 describes the energy of the Bloch function as a periodic function of the wave factor with a period of $2\pi/R_a$. The region between $-\pi/R_a$ and π/R_a is called the Brillouin zone. The energy ranges from $E_0 - 2V_{ec}$ to $E_0 + 2V_{ec}$ for $k = 0$ and $k = \pi/R_a$, respectively and is distributed in a band resulting from the interaction of all the atomic localized energy levels. The bandwidth is proportional to the interaction given by V_{ec}. If the bandwidth is large, then there is a high charge carrier delocalization and high mobilities are expected. In a band picture the charge carrier mobilities are expressed by

$$\mu = \frac{q\tau}{m_{eff}} \tag{2.91}$$

where τ is the scattering time, q the charge, and m_{eff} the effective mass of the electron or holes.

The band theory is well established for inorganic covalently bound materials. However, it is not suited to describe transport in organic materials as organic molecular crystals are only weakly bound by van der Waals interactions. As a consequence, those crystals are very flexible and the prerequisite of fixed sites in band theory is not given. Due to the complex nodal structure of molecular orbitals in organic systems the coupling parameter becomes very sensitive to even small displacements of the nuclei. This leads to a charge carrier localization as lattice vibrations (called phonons) disrupt the long-range order in organic crystals.[94] The existence of charge carriers or excitons forces nearby molecules to relax, which leads to additional perturbation of the order in the crystal and thus, emphasizes the localization by enlarging the relaxation energy. The electronic coupling Models have been developed to incorporate local[115] (Holstein) or nonlocal[116] (Peierls) coupling. Nonlocal coupling results in a polaron model describing the charge carrier as partially localized and dressed by phonons.[117-120] The average coupling is of the same order of magnitude as the fluctuations of the coupling resulting in a strong localization.[121] Other models treat the inter- and intramolecular vibrations classically while the charges are localized.[122-124]

3. Calculation of the Electronic Coupling Parameter – Concepts

Transport of charges or exciton energy strongly depends on the electronic coupling matrix element also known as the transfer integral. This interaction is defined by $V_{ec} = \langle \Psi_A | \hat{H} | \Psi_B \rangle$, where $\hat{H}$ is the electronic Hamiltonian of the system and Ψ_A and Ψ_B are wavefunctions, which represent the electronic state, respectively, before and after the charge or energy transfer process. Both states are diabatic, *i.e.* there is no coupling between them.[125] The diabatic states can be chosen as local charged or excited molecules as we will see in section 3.1.3 or as it has been shown by Fink *et al.* in Ref.126 for a local complete-active-space self-consisting-field (CASSCF)[127-129] approach for exciton transfer. In many cases, the adiabatic picture turns out to be easier to apply[96] (the adiabatic representation is diagonal with respect to the electronic Hamiltonian in contrast to the diabatic representation), but more expensive. Sections 3.1.4 and 3.2.1 describe an adiabatic ansatz for exciton and charge transport, respectively.

3.1 Exciton Transport

In organic solar cells exciton transport is a major bottleneck due to its low efficiency. Therefore, improvements can be achieved mostly at developing materials with better exciton transport properties. Apart from the rather easily accessible reorganization energy, the main focus in this section of the thesis is the calculation of the transfer integral. Starting from the Förster Theory the related Dexter Transport will be introduced. Then, the diabatic approximation called monomer transition density approach (MTD) will be introduced. Finally the more complete and easier supermolecular approach will be discussed, which uses the adiabatic picture.

3.1.1 Förster Theory

Exciton transport was observed experimentally and explained theoretically by Theodor Förster. He discovered an increase of fluorescence quenching of a given dye in solution, if the concentration of a second dye with a large transition dipole moment increases.[130] The classical treatment was published in 1951,[67] while the quantum mechanical description already appeared in 1948[130] and was reviewed in 1965.[131] Before this, Eisenschitz *et al.* discussed in 1929 the interaction of two

ground state H-atoms and found the so called London dispersion.[132] There, the interaction energy E_{disp} between a H-atom in the ground state to a H-atom in the excited state was found to be proportional to $\frac{1}{R_{AB}^6}$. Named after its discoverer, exciton transport is also known as Förster Resonance Energy Transfer (FRET)[133-136] or other names like *e.g.* excitation energy transfer (EET).[137-140] FRET originally describes the process of transport of absorbed light between two chromophores. The transport process does not involve photons, but a dipole-dipole term stemming from the electrostatic interaction of the electrons. In the classical treatment the excited donor induces an oscillatory field at the acceptor. Also important is the conservation of the spin in both acceptor and donor system; that´s why FRET is also called singlet-singlet-transfer. Within Förster´s approximated description the coupling can be calculated by

$$V_{ec} \approx \frac{1}{n^2 R_{AB}{}^3}\left(\vec{D}_A \cdot \vec{D}_B - 3\frac{(\vec{D}_A \cdot \vec{R}_{AB})(\vec{R}_{AB} \cdot \vec{D}_B)}{R_{AB}{}^2}\right) = \frac{D_A D_B}{n^2 R_{AB}{}^3}\kappa, \qquad (3.2)$$

where n is the refractive index of the medium, $\vec{R}_{AB}$ the distance between the chromophores, κ the orientation factor, and $\vec{D}_A$ ($\vec{D}_B$) the transition dipole moment of system A (B). In most cases κ is assumed to be 2/3, which is the average value, if the chromophores are rotated in all possible orientations.[141, 142] Exciton transfer is named homo-transfer, if both systems (molecules, complexes or nanoparticles) are

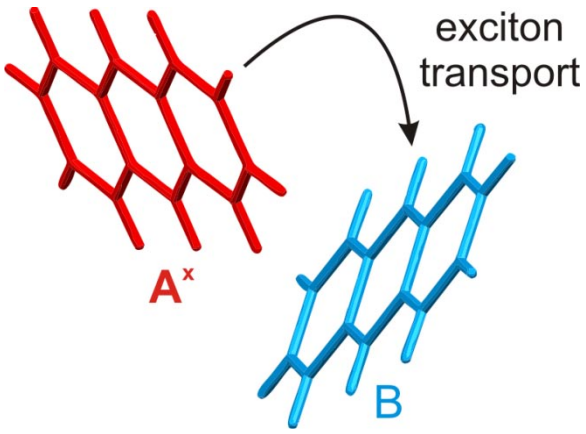

Figure 3.1 Radiationless exciton transport between two identical, neighbored molecules A and B.

of the same type, see figure 3.1, and hetero-transfer, if the involved systems are different in their chemical structure.

In this thesis we only consider homo-transfer between two identical molecules, A and B, see figure 3.1. The excitation energy is transferred from molecule A^x (^{x} denotes the molecule to be excited) to B. In the one-electron picture the excited electron in the LUMO of molecule A is deexcited, while simultaneously one electron in the HOMO of B gets excited as shown schematically by the molecular orbital scheme in figure 3.2:

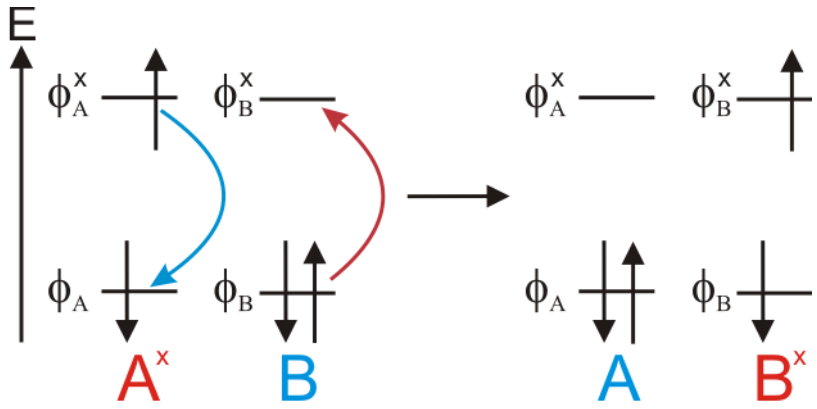

Figure 3.2 Schematic description of the exciton transport for homo-transfer between two identical systems A and B in the one-electron picture. An electron in the excited state A^x is deexcited from its LUMO ϕ_A^x to its HOMO ϕ_A while simultaneously one electron in molecule B gets promoted from the HOMO ϕ_B to the LUMO ϕ_B^x.

Limitations of this ansatz are the requirement to have bright states, *i.e.* transition-dipoles non-equal to zero, and the range limit, where the approximation is valid. Generally the dipole approximation is reasonable for distances greater than 10 Å. For dimers closer than that higher moments and overlap effects become important.

3.1.2 Dexter Transfer

Closely related to the quantum mechanical description of Förster is Dexter´s variant published in 1953.[143] Dexter pointed out that other energy transfer mechanisms besides the Förster type (dipole-dipole interaction) are possible. Higher multipole-multipole interactions also contribute to the exciton transport, but these are more range dependent than the dipole-dipole interaction. Thus, Dexter transfer

becomes important for closely spaced systems, and for forbidden excitations with no transition dipole moment. This may happen by interchanging the electron between the LUMO on A and the LUMO on B. At the same time the electron in the HOMO of B with the spin opposite to the electron in the HOMO of A is transferred to the HOMO of A. This is shown in Figure 3.3:

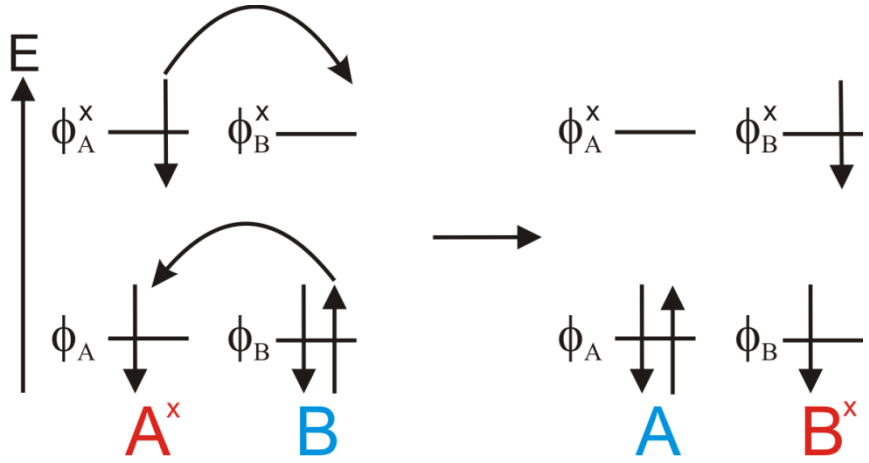

Figure 3.3 Dexter Transfer between two systems A and B. Electrons are interchanged between the LUMOs (ϕ_A^x and ϕ_B^x) and HOMOs (ϕ_A and ϕ_B) of the systems.

Similar to the Förster transfer the spin is also conserved. But in contrast, the Dexter mechanism is possible for energy transfer of triplet states. The intermolecular exchange of electrons requires significant overlap between the MOs of the different systems. This is only possible for closely spaced molecules and decreases exponentially. Consequently, Dexter transfer rates decrease rapidly with increasing distance of the systems.

3.1.3 Monomer Transition Density Approach

Another possibility to quantify exciton transport is the Monomer Transition Density (MTD) approach.[126] Using the same formulas as described in the previous chapters, the difference arises in the calculation of the electronic coupling parameter V_{ec}. It can be calculated by

$$V_{ec} = \frac{H_{AB} - H_{AA}S}{1 - S^2}. \qquad (3.3)$$

Eq. 3.3 is the exact solution of the supermolecular ansatz (see section 3.1.4), which refers to the Davydov splitting (see section 2.2.2). MTD approximates this coupling by assuming S → 0 for large intermolecular distances, resulting in

$$V_{ec} \approx H_{AB} - H_{AA}S \approx H_{AB}. \tag{3.4}$$

Applying Slater-Condon rules as well as neglecting Dexter-Transfer,[143] H_{AB} is given in a one-electron picture by

$$H_{AB} = 2 \int d\mathbf{r}_1 \, d\mathbf{r}_2 \phi_A^x(1)\phi_A(1)\frac{1}{r_{12}}\phi_B(2)\phi_B^x(2). \tag{3.5}$$

This corresponds to Fig. 3.2 of the Förster-Transfer.[130, 144, 145] Eq. 3.5 includes the product of the HOMO and LUMO orbital on molecule A or B. The result is the transition density (TD) of the HOMO-LUMO excitation on that molecule, which can be visualized. For the example of ethylene, this is depicted in figure 3.4:

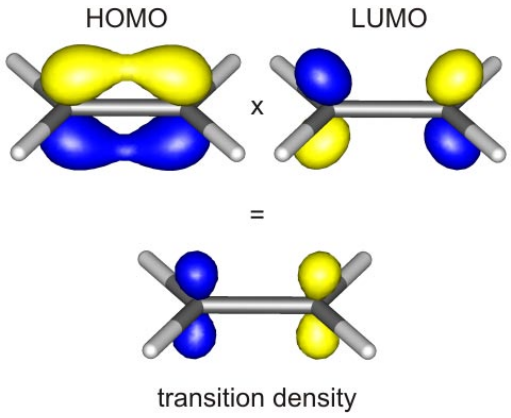

Figure 3.4 The product of the HOMO and LUMO orbital is the transition density.

Leaving the one-electron picture MTD approximates the electronic coupling parameter by the Coulombic coupling integral

$$V_{ec}^{MTD} = \iint \frac{\rho_D(\mathbf{r}_1)\rho_A(\mathbf{r}_2)}{r_{12}} d\mathbf{r}_1 d\mathbf{r}_2. \tag{3.6}$$

Here, r_{12} is the distance between the electrons at $\mathbf{r}_1$ and $\mathbf{r}_2$ and $\rho_D(\mathbf{r})$ ($\rho_A(\mathbf{r})$) is the TD resulting from the deexcitation (excitation) on the donor (acceptor) molecule. These may be evaluated from the excited and ground state wave functions Ψ_x and Ψ_g of the acceptor or donor[146]

$$\rho(\mathbf{r}_1) = N \int \int \Psi_x^*(\mathbf{r}_1, \mathbf{r}_2, \dots, \mathbf{r}_N) \cdot \Psi_g(\mathbf{r}_1, \mathbf{r}_2, \dots, \mathbf{r}_N) d\mathbf{s} d\mathbf{r}_2 d\mathbf{r}_3 \dots d\mathbf{r}_N. \tag{3.7}$$

N is the number of electrons in the system and d**s** = $ds_1ds_2…ds_N$ indicates integration over all spin coordinates of these electrons. The TDs ρ are expanded in terms of the basis functions χ_i of the system, *e.g.*

$$\rho_A(\mathbf{r}_1) = \sum_{ij} \rho_{A,ij}\chi_i^*(\mathbf{r}_1) \cdot \chi_j(\mathbf{r}_1), \tag{3.8}$$

and the integral in Eq. (3.6) is evaluated via the two-electron integrals

$$V_{ec}^{MTD} = \sum_{ij}\sum_{kl} \rho_{D,ij}(ij|kl)\rho_{A,kl}, \tag{3.9}$$

with

$$(ij|kl) = \iint \chi_i^*(\mathbf{r}_1)\chi_j(\mathbf{r}_1)\frac{1}{r_{12}}\chi_k^*(\mathbf{r}_2)\chi_l(\mathbf{r}_2). \tag{3.10}$$

Familiar to the MTD approach is the transition density cube method (TDC).[147, 148] It is based on the same assumptions as MTD and approximates V_{ec} by the Coulombic interaction. The difference arises in the calculation: While MTD evaluates the coupling by the complete transition densities, TDC first subdivides these into small cubes (also called cells), which interact then. These interactions are finally integrated to give V_{ec}.

3.1.4 Supermolecular Approach

More expensive than the application of Förster or Dexter theory and MTD is the calculation of the coupling by the supermolecular approach. There, the coupling V_{ec} is determined in accordance to the Davydov splitting as

$$V_{ec} = \frac{E_D^+ - E_D^-}{2}. \tag{3.11}$$

E_D^+ and E_D^- represent the energies of the two excited states of the dimer (their eigenenergies are denoted E^1 and E^2 in section 2.2.2), which result from the coupling of the excited states in the monomer units. Compared to Förster theory the advantages of this approach are its general applicability to *e.g.* transfer between “dark states” with vanishing transition dipole moment. Furthermore, this approach is not restricted to large distances between the chromophores. Especially at close proximity between the monomers this approach excels as shown already by Fink *et al*.[126] with a comparison of a broad range of methods: Depending on the system size higher level methods like CASSCF[128, 149] or spin-component scaled approximate

coupled cluster singles-and-doubles model[150-153] (SCS-CC2) should be chosen. If the system size is too big less expensive methods like time-dependent Hartree-Fock (TD-HF) or time-dependent Density Functional Theory (TD-DFT) should be applied. Fink *et al.* stated not to use TD-DFT due to the problematic charge-transfer intruder states.[126] Thus states were predicted with unacceptable large errors of up to 4 eV which consequently lead to an erratic admixture with neutral states. This spoils the shape and the energy splitting of the states used to compute V_{ec}. In contrast, TD-HF appeared as a better alternative: The excitation energies and the transition dipole moments are predicted reasonably at the same computational cost of TD-DFT with hybrid functionals. In more recent work, Sagvolden *et al.* concludes that Fink *et al.* are too pessimistic regarding the use of TD-DFT:[154] According to their data the problems found by Fink *et al.* are present in their work as well, but only for the Ideal Dipole Approximation (IDA), B3LYP[155] and the PBE[156] functional. Global hybrid functionals with a larger fraction of exact exchange like BHLYP[157] perform as well as CC2,[153] while TD-HF overestimates the monomer transition dipole moment resulting in incorrect large couplings at long-range.

A further disadvantage to the supermolecular approach is the computational cost. Only here it is necessary to calculate the dimer, while the other approaches only need calculations on the monomers. Another problem occurs for compounds with energetically nearly spaced excited states. Figure 3.5 depicts in (a) the case of

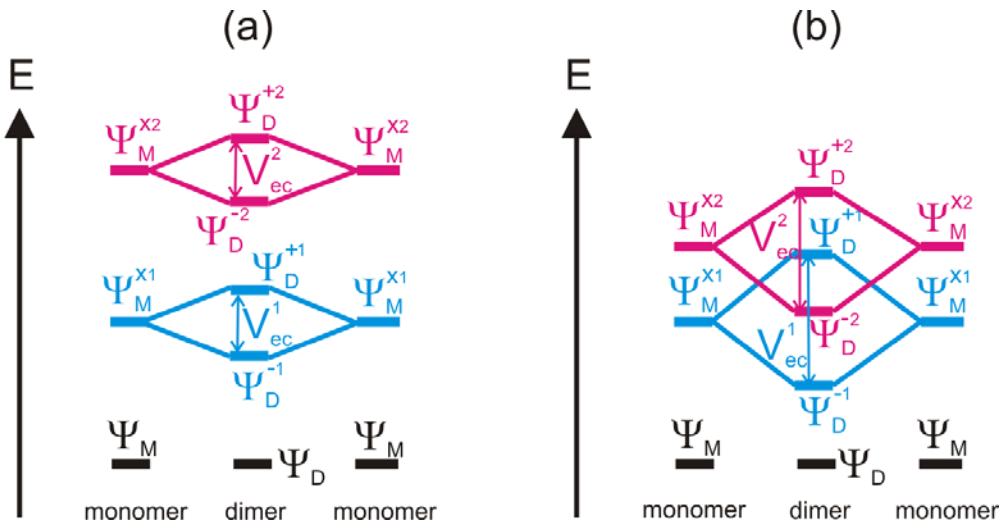

Figure 3.5 Davydov splitting shown for the case of well separated excited states (a), and closely spaced excited states (b) in the monomers.

energetically well separated excited states in the monomer and dimer, while (b) shows closely spaced monomer excited states. There, E_D^{-1} and E_D^{+1} of the dimer states Ψ_D^{-1} and Ψ_D^{+1}, referring to monomer excited state Ψ_M^{x1}, are difficult to determine in the dimer, since their order is not the first and second excited state of the dimer. Additional evaluations of the dimer excited states are required to determine their relation to the monomer states. This can be done with the help of TDs (see section 3.1.3) as their shapes of Ψ_D^- and Ψ_D^+ resemble the plus and minus linear combinations of the corresponding monomer TDs. Ethylene is shown as an example in figure 3.6:

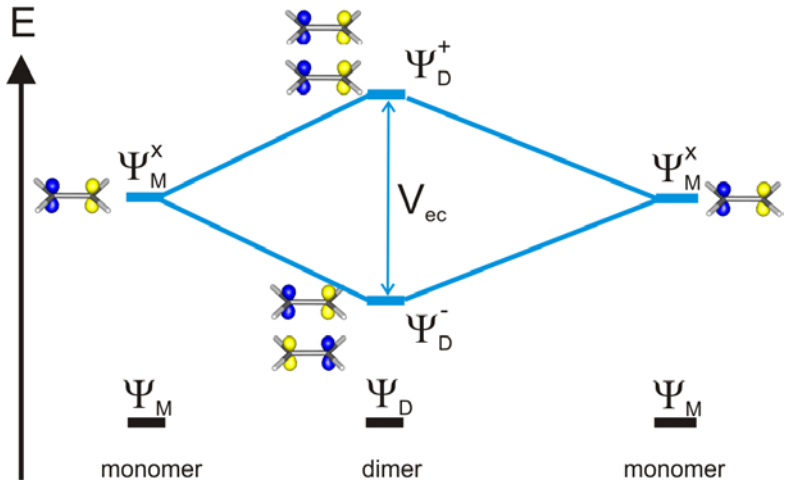

Figure 3.6 Description of the dimer states Ψ_D^- and Ψ_D^+ as linear combinations of the monomer excited states Ψ_M^+ and their corresponding transition densities.

3.2 Charge Transport

3.2.1 Energy Splitting in Dimer

The simplest way of calculating the electronic coupling for charge transfer is referred to as the “energy splitting in dimer” (ESD) method.[125, 158-160] The basis assumption is identical to section 3.1.4: At the transition point the excess charge is delocalized over both monomers. Calculating the adiabatic states Ψ_1 and Ψ_2 with their corresponding energies E_1 and E_2 results in the electronic coupling as $V_{ec} = (E_2 - E_1)/2$. Although the structure of the charged dimer at the transition state (*i.e.* the crossing point for diabatic states) is required, it is a common approximation to consider the geometrical structure of the neutral dimer or the geometry obtained as the average over the ionic and neutral nuclear coordinates of the monomers.[161-163] To further simplify the calculation Koopmans´ theorem[164] is applied, *i.e.* ESD relies on a one-electron approximation. Therefore, the transfer integral for charge transport can be calculated from the energy of the frontier molecular orbitals:

$$V_{ec} = \frac{\varepsilon_{L+1} - \varepsilon_L}{2} \tag{3.12}$$

for electron transport and

$$V_{ec} = \frac{\varepsilon_H - \varepsilon_{H-1}}{2} \tag{3.13}$$

for hole transport, where $\varepsilon_{L(H)}$ and $\varepsilon_{L+1(H-1)}$ are the energies of the LUMO and LUMO+1 (HOMO and HOMO-1) orbitals calculated by a closed-shell configuration of the dimer neutral state. ESD is the most frequently used method due to its easy application. The estimated transfer integrals agree well with results derived by second-order perturbation theory based on CASSCF (CASPT2) and CASSCF-State Interaction (CASSI) calculations.[165, 166] However, ESD should be used cautiously, if the monomers are strongly coupled. Then the LUMO and HOMO orbital splitting can be significantly different from the actual electronic coupling matrix element due to large spatial overlap.[167] The one-electron approximation in the dimer is no longer valid and the transfer integral must be evaluated by $V_{ec} = \langle \Psi_A | \hat{H} | \Psi_B \rangle$, which is done in the next section.

3.2.2 Two-State Model

The following section discusses only the LUMO and LUMO+1 orbitals, which determine the properties for electron transport. In the case of hole transport the HOMO and HOMO-1 orbitals have to be considered, respectively. This case works in the same way, but has been omitted for the sake of clarity.

In the present work the transfer integrals of charge transport have been calculated by a combination of a diabatic and an adiabatic ansatz using the one-electron approximation. To evaluate the transfer integral in the dimer, the charge is considered to be initially localized on one monomer. In the final state, it has transferred and localizes on the other monomer. As in the previous chapter, the initial and final states of the dimer are described by the LUMO orbitals for hole transport of the isolated, neutral monomer. Again, this approximation is only valid for systems with well separated (several tenths of an eV) LUMO and LUMO+1 orbitals, which holds true for systems such as pentacene. There, a dimer composed of such monomers has a LUMO level with significant contributions stemming only from the LUMOs of the two monomers. The transfer integral can then be defined as

$$V_{ec} = \langle \varphi_{L,A} | \hat{H} | \varphi_{L,B} \rangle \qquad (3.14)$$

with $|\varphi_{L,A}\rangle$ and $|\varphi_{L,B}\rangle$ being the LUMO level of the monomers A and B responsible for electron transport. The transfer integral for both intra- and intermolecular transport is calculated with this approach, which is also known as the “two-state model”.[125, 159, 160, 162, 163, 168]

If the assumption of well separated LUMO and LUMO+1 orbitals is unjustified, then Eq. 3.14 is no longer valid. In *e.g.* phenanthroline-based bathocuproine (BCP),

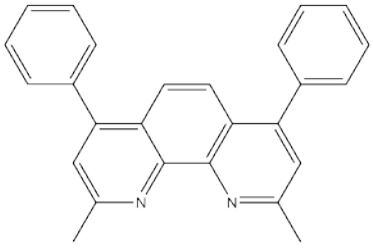

Figure 3.7 Chemical structure of phenanthroline-based bathocuproine (BCP).

see figure 3.7, the LUMO/LUMO+1 energy difference is merely 0.02 eV. For such cases a more general definition of the electronic coupling is necessary, which includes not only the LUMO but also the LUMO+1 orbitals of the monomers in both initial and final states of the coupled dimer system. Then, the LUMO level becomes

$$|\Psi_L\rangle = c_{L,A}|\varphi_{L,A}\rangle + c_{L+1,A}|\varphi_{L+1,A}\rangle + c_{L,B}|\varphi_{L,B}\rangle + c_{L+1,B}|\varphi_{L+1,B}\rangle = |\psi_1\rangle + |\psi_2\rangle. \quad (3.15)$$

A and B represent monomer A and B, $c_{L,A}$, $c_{L,B}$ and $c_{L+1,B}$, $c_{L+1,A}$ are the coefficients of the dimer LUMO and LUMO+1 levels with the molecular orbitals $|\varphi_L\rangle$ and $|\varphi_{L+1}\rangle$ taken from the isolated monomers as basis set. $|\Psi_L\rangle$ can be split into a combination of two components,

$$|\psi_A\rangle = c_{L,A}|\varphi_{L,A}\rangle + c_{L+1,A}|\varphi_{L+1,A}\rangle, \quad (3.16)$$

$$|\psi_B\rangle = c_{L,B}|\varphi_{L,B}\rangle + c_{L+1,B}|\varphi_{L+1,B}\rangle, \quad (3.17)$$

which are mixed states of $|\varphi_L\rangle$ and $|\varphi_{L+1}\rangle$ localized on monomer A or B. $|\psi_A\rangle$ is the best description for the initial state and $|\psi_B\rangle$ for the final state in this context, if both states are orthogonalized. The electronic coupling is now calculated by

$$V_{ec} = \langle\psi_A|\hat{H}|\psi_B\rangle \quad (3.18)$$

Compared to Eq. 3.14, Eq. 3.18 represents a linear combination of the monomer LUMO and LUMO+1 levels as the initial and final states where the electronic Hamiltonian is determined by the dimer system. $|\psi_A\rangle$ and $|\psi_B\rangle$ is the new basis set, which can be seen as an auxiliary basis set of $|\varphi_{L,A}\rangle$ and $|\varphi_{L+1,A}\rangle$. If $c_{L+1,A}$ and $c_{L+1,B}$ are both zero, then Eq. 3.18 is equivalent to Eq. 3.14.[169]

To obtain the correct values for transfer integrals Valeev *et al*. emphasized the necessity of a proper orthogonalization of the initial and final states, *i.e.* $|\psi_A\rangle$ and $|\psi_B\rangle$.[170] In matrix form, the eigenvalue equation is represented by

$$\begin{pmatrix} H_{AA} & H_{AB} \\ H_{BA} & H_{BB} \end{pmatrix}\begin{pmatrix} c_A \\ c_B \end{pmatrix} = E\begin{pmatrix} S_{AA} & S_{AB} \\ S_{BA} & S_{BB} \end{pmatrix}\begin{pmatrix} c_A \\ c_B \end{pmatrix}, \quad (3.19)$$

where $H_{AA} = \langle\psi_A|\hat{H}|\psi_A\rangle$, $H_{BB} = \langle\psi_B|\hat{H}|\psi_B\rangle$, $H_{AB} = H_{BA} = \langle\psi_A|\hat{H}|\psi_B\rangle$, $S_{AA} = \langle\psi_A|\psi_A\rangle$, $S_{BB} = \langle\psi_B|\psi_B\rangle$, and $S_{AB} = S_{BA} = \langle\psi_A|\psi_B\rangle$. Note that the overlap S_{AA} and S_{BB} are not normalized and therefore different from 1. To obtain correct values for V_{ec} a

symmetric orthogonalization should be applied to the basis set ($|\psi_A\rangle$,$|\psi_B\rangle$), and the Hamiltonian matrix **H**, as pointed out in Ref.125 and Ref.170. This can be done by using standard procedures as given in *e.g.* Ref.91. As a result

$$\mathbf{H}' = \mathbf{X}^{+}\mathbf{H}\mathbf{X}, \tag{3.20}$$

and

$$|\psi'_A\rangle = \mathbf{X}_{AA}|\psi_A\rangle + \mathbf{X}_{BA}|\psi_B\rangle,$$

$$|\psi'_B\rangle = \mathbf{X}_{AB}|\psi_A\rangle + \mathbf{X}_{BB}|\psi_B\rangle, \tag{3.21}$$

where **X** is the transformation matrix. ($|\psi'_A\rangle$, $|\psi'_B\rangle$) is the new orthogonal basis set. The off-diagonal elements of $\mathbf{H}'$ are defined as the “effective transfer integrals”,

$$V_{ec,eff} = \langle\psi'_A|\hat{H}|\psi'_B\rangle. \tag{3.22}$$

4. Exciton and Charge Transport Properties in Weakly Interacting Systems

4.1 Exciton Transport in Anthracene

Anthracene $C_{14}H_{10}$ (depicted in figure 4.1) was chosen as a test system for our programs and concepts, because its exciton and charge transport properties are experimentally well investigated.[171-174] For a theoretical simulation of these problems the knowledge of the molecular, crystal and electronic structure is necessary. This

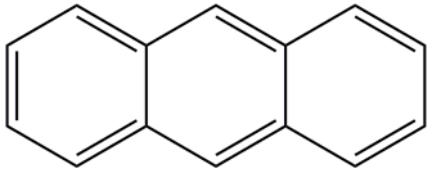

Figure 4.1 Chemical structure of anthracene.

thesis uses the crystal structure published in Ref.175, which is depicted for its unit cell in figure 4.2: The crystal is composed of two monoclinic substructures with translation symmetric molecules at the corners resulting in a herringbone structure.

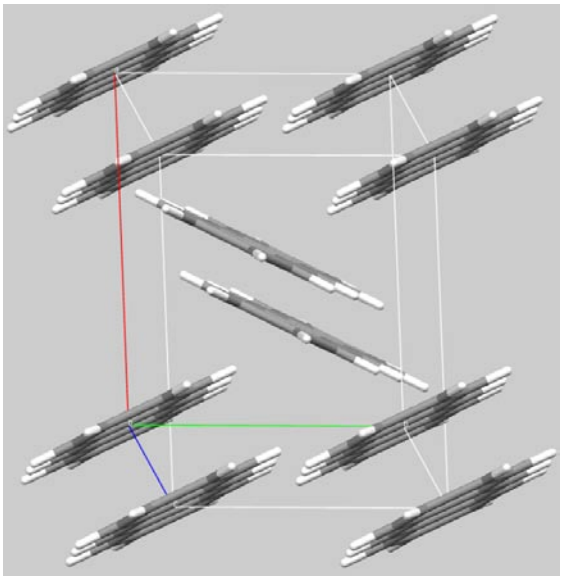

Figure 4.2 Crystal structure of anthracene: monoclinic polymorph, α = 90°, β = 125°, γ = 90°, a = 8.5 Å (red), b = 6.0 Å (green), and c = 11.1 Å (blue).[175]

Table 4.1: Reorganization energies λ for anthracene calculated with three different approaches. Energies are given in eV relative to their corresponding optimized ground state structure in the electronic ground state.

	SCS-CC2 / TZV(2df,p)		B3LYP / TZV(2df,2pd)		RI-BLYP / TZV(2df,2pd)	
structure / state	ground state	excited state	ground state	excited state	ground state	excited state
ground state	0.00	0.25	0.00	0.22	0.00	0.17
excited state	3.84	3.56	3.20	2.98	2.86	2.69
λ	0.54		0.44		0.34	

To obtain the reorganization energy the description given in section 2.1.2.3 was followed. The external reorganization energy was neglected. The total reorganization energy approximated by the internal relaxation energy is given in table 4.1. Depending on the approach it is either 0.54 eV for the spin-component scaled approximate coupled cluster second order method,[150-153] or 0.34 eV for the resolution of identity[176, 177] (RI) approximated BLYP functional.[178-180] B3LYP[155] as a hybrid functional performs in between those producing a relaxation energy of 0.44 eV. SCS-CC2 has been proven to be the better choice for the description of π-conjugated[181-183] systems and therefore, its results are used for anthracene in the following calculations. Since B3LYP has a lower computational cost and performs better than BLYP it is a good compromise for bigger systems.

The calculation of the free reaction energy ΔG^0 was neglected due to two reasons: First, it is assumed to be 0, because the surroundings of each molecule in this crystal morphology are identical to the other molecules. Second, the computational costs to calculate an excited molecule with a reasonable amount of surrounding molecules exceed the scope of this work, if no approximations are applied. This task is currently addressed by other coworkers.

For the description of exciton transport we chose the $1^1B_{2u}^+$ state. Kawashima *et al*.[184] used a complete-active-space self-consisting-field[127-129] (CASSCF) approach which describes this state as a combination between the HOMO-LUMO (coefficient

0.8753) and HOMO-1-LUMO+1 (coefficient 0.1613) transition. It has a weak transition dipole moment and lies 0.02 eV below in excitation energy (exp. 3.43 eV[185]) than the $1^1B_{3u}^-$ state (exp. 3.45 eV[186]). The latter transition has no transition dipole moment and is composed of the HOMO-1-LUMO and HOMO-LUMO+1 configurations with coefficients of 0.6003 and -0.5886, respectively.

The transition densities of both states are shown in figure 4.3. Note that the contour values were chosen differently for a better visualization (±0.0060 in $1^1B_{2u}^+$ and ±0.0025 in $1^1B_{3u}^-$). Figure 4.3 explains visually, why the $1^1B_{2u}^+$ has a net transition dipole and $1^1B_{2u}^+$ does not: the plus and minus phases rule themselves out in the $1^1B_{3u}^-$ transition density resulting in no transition dipole moment (experimental oscillator strength f = 0)[184]. In contrast, the plus and minus phases on the top and bottom atoms in figure 4.3 for the $1^1B_{2u}^+$ have opposing sign towards each other. The do not cancel each other completely. Hence, the transition dipole moment has an experimental oscillator strength of f = 0.1.[184]

Using the MTD approach described in section 3.1.3 all dimer combinations in the unit cell have been evaluated regarding their electronic coupling parameter V_{ec} for both the $1^1B_{2u}^+$ and $1^1B_{3u}^-$ transitions. Applying the WAVELS program package with a (4/4) complete-active-space to produce the transition densities results in the electronic couplings summarized in table 4.2, which is read as follows: m0 denotes a monomer sitting on an edge of the unit cell and m1 is the translation variant monomer closer to m0. The three numbers in front describe the translation of the

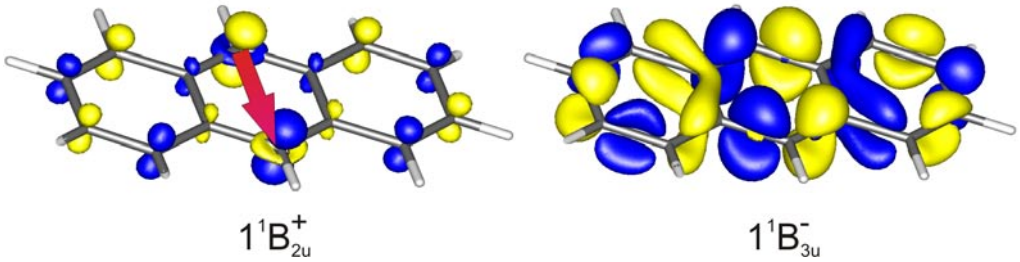

Figure 4.3 Transition densities of the $1^1B_{2u}^+$ and $1^1B_{3u}^-$ states in anthracene. The red arrow represents the transition dipole moment, which is only found for the $1^1B_{2u}^+$ transition.

Table 4.2 V_{ec} in meV for the $1^1B_{2u}^+$ and $1^1B_{3u}^-$ transition in the anthracene crystal calculated by the MTD approach. See text for the nomenclature.

dimer	V_{ec} $(1^1B_{2u}^+)$	V_{ec} $(1^1B_{3u}^-)$
01:00:00_m0:m0	6.69	-0.03
01:01:00_m0:m0	3.73	-0.02
-1:01:00_m0:m0	3.73	-0.02
01:01:-1_m0:m0	3.35	0.00
01:00:01_m1:m1	3.07	-0.40
00:-1:01_m0:m0	1,77	0.15
-1:00:01_m0:m0	0.91	0.01
01:00:01_m0:m0	0.91	0.01
00:01:01_m0:m0	0.86	0.08
-1:00:01_m1:m0	0.77	0.03
01:01:01_m0:m0	0.67	0.01
-1:01:01_m0:m0	0.67	0.01
01:-1:01_m0:m0	0.58	0.01
-1: -1: -1_m1:m0	-0.29	0.01
-1:00:-1_m1:m0	-0.29	0.00
00:-1:-1_m1:m0	-0.76	0.03
00:00:-1_m0:m1	-0.76	0.02
-1:-1:00_m0:m1	-1.57	-0.01
00:00:00_m0:m1	-1.67	-0.35
00:-1:01_m0:m1	-1.79	0.91
00:00:01_m0:m1	-2.21	0.38
00:00:01_m0:m0	-3.07	0.40
-1:-1:01_m0:m1	-3.66	-0.02
00:-1:00_m0:m1	-5.16	-0.98
-1:00:00_m0:m1	-5.17	-0.98
00:01:00_m0:m0	-42.92	-0.11

second monomer along the cell axes. *E.g.* 00:00:-1_m0:m1 is a dimer formed by two translational variant molecules, where m1 is translated once in opposite direction of the c axis.

The results show that exciton transport is faster for the $1^1B_{2u}^+$ than $1^1B_{3u}^-$ transition. The values differ by up to two orders of magnitude. As the transfer rate is dependent on the coupling quadratically (see Eq. 2.37), it is justified to approximate exciton transport in anthracene only with the $1^1B_{2u}^+$transition. Furthermore, the biggest coupling is found along the b-axis (-42.9 meV) and surpasses the second biggest by a factor of ~ 6 (a-axis, V_{ec} = 6.7 meV). This already indicates a strong preferred direction and exciton diffusion lengths are expected to be big along the b-direction, if only one dimensional transport is assumed.

A comparison between differently sized complete-active-spaces has been done by applying a 2/2 CAS. A selection of dimer structures and their respective V_{ec} between this 2/2 CAS and the former used 4/4 CAS is shown in table 4.3. the results show that a proper choice of the size of the CAS is essential. Although the HOMO-LUMO transition configuration has a coefficient of 0.8753 in a CAS(12/12) and therefore is the main contribution, the neglect of the HOMO-1-LUMO+1 transition configuration (which is included in a (4/4)CAS) leads to errors greater than a factor of 10. Therefore, the correct choice of a proper complete-active-space is compulsory.

Table 4.3 Influence of the size of the complete-active-space on $|V_{ec}|$ in anthracene for the $1^1B_{2u}^+$transition. The couplings are given in meV.

dimer	CAS(4/4)	CAS(2/2)
00:01:00_m0:m0	42.9	80.6
01:00:00_m0:m0	6.69	16.5
00:00:01_m0:m0	3.07	8.8
00:00:00_m0:m1	1.67	8.0
01:01:01_m0:m0	0.67	10.8

An evaluation of the self diffusion coefficient and the exciton diffusion length was done in cooperation with Jan Schoeneboom and Yuki Nagata from BASF SE, Ludwigshafen. The results are summarized in table 4.4. Overall our combined efforts produce values in very good agreement to the experiment. The deviation of the calculated L_D in b-direction from the experiment can be explained with the

Table 4.4 Simulated and experimental diffusion constants and exciton diffusion lengths for isotropic and anisotropic exciton transport in anthracene.

	simulation / experiment				
dimension	**V_{ec} (meV)**	**k (10^{12} s^{-1})**	**D (10^{-7} m^2s^{-1})**	**L_D (nm)**	
isotropic	-	-	28	230	380[174] 200[171] 130[172] 60[173]
a	6.7 / -	0.5 / -	4.4	93 / 60 (±10)[173]	
b	42.9 / -	21 / -	87	420 / 100[173]	
c	3.1 / -	0.1 / -	2.4	70 / 40[173]	

approximations in the MTD approach: MTD approximates Vec by neglecting overlap effects. Since the b-axis is the shortest one, the biggest errors are expected to be found there. Nevertheless, the MTD approach with a correct CAS-size proves to be well-performing.

4.2 Charge Transport in Perylene

Perylene $C_{20}H_{12}$ (chemical structure in figure 4.4) exist in two known crystal morphologies. The α form was first reported by Donaldson *et al.* in 1953.[187] Tanaka *et al.* published the β form in 1963[188] and reported, that β is transformed into α at about 140°C. At and below room temperature, both forms are stable.[189] Both polymorphs are monoclinic; their space group is $P2_1/c$. The α form has 4 monomers in the unit cell, which cannot be projected onto another by applying n ($n \in \mathbb{Z}$) times a translation along any combinations of unit cell axis vectors. The interplanar spacing

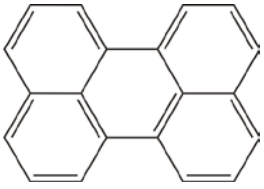

Figure 4.4 Chemical structure of perylene.

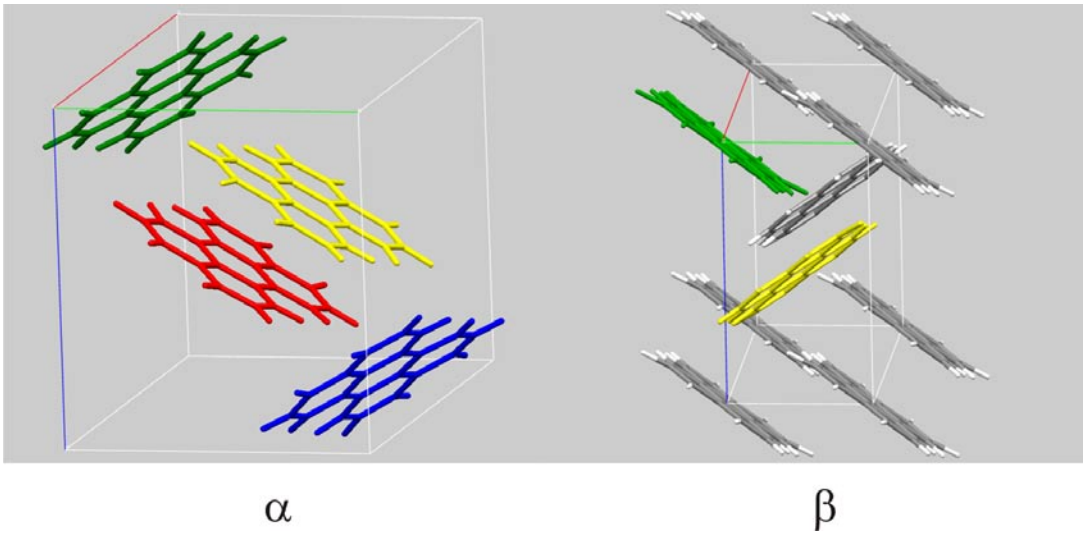

Figure 4.5 Crystal structure of α- and β-perylene (CCDC 198723 and CCDC198724). Nomenclature: m0 (green), m1 (yellow), m2 (blue), and m3 (red). Cell axes: a red, b green, and c blue.

between dimeric pairs is 3.415 Å in α, and 3.46 Å in β. The latter has two translational invariant monomers in the unit cell (identical to anthracene). Both crystal structures are shown in figure 4.5. The cell axis are longer in the α form (a = 10.24 Å, b = 10.79 Å, c = 11.13 Å) than in β (a = 9.76 Å, b= 5.84 Å, c = 10.61 Å). Shorter distances should result generally in stronger coupled dimers. The transfer integrals have been calculated based on the two-state model described in section 3.2.2. All calculations were done on the B3LYP/cc-pVDZ level, which was proven to perform well enough by Sancho-Garcia *et al.*[190] The reorganization energies are shown in table 4.5. If only these are considered, then perylene preferably transports positive charge carriers as λ_{hole} is smaller by 29 meV (16.8%) than $\lambda_{electron}$.

Table 4.5 Reorganization energies given in meV for electron and hole transport in perylene calculated on the B3LYP/cc-pVDZ level.

	$\lambda_{neutral}$	$\lambda_{charged}$	λ
hole	70	72	142
electron	84	86	171

4.2.1 Hole Transport

The most important couplings for both polymorphs are shown in table 4.6 for α- and β-perylene. The full list is available in the appendix. The strongest coupled dimer in α-perylene is 00:00:00_m1:m3, in which the monomers can also be described as a very closely spaced π-stack with an intermolecular distance < 3.5 Å. Here, m1 and m3 have an electronic coupling of 49.0 meV. As a consequence, transfer will be slightly preferred in α-perylene along this direction. Because there are many other dimers with couplings ranging from 1 meV to 30 meV, the holes will diffuse isotropically, if one considers only the couplings. Transport between translation symmetric molecules (*i.e.* m0:m0) is less important, as the couplings are very weak (see table 4.6, bottom-left). Stronger coupled than the best dimer in α-perylene by a factor of 2.5 is the transport along the translation symmetric molecules in b-direction of β-perylene (V_{ec} = 127.5 meV). No couplings of the same magnitude can be found in the remaining crystal, as the second strongest dimers (*e.g.* 01:01:01_m1:m0) have V_{ec}-values of only 10.1 meV. Because the coupling enters the semi-classical Marcus

Table 4.6 Dimers in α- and β-perylene with the most important couplings in meV regarding hole transport. The lower part represents the coupling between dimers along the cell axes.

alpha		**beta**	
dimer	**V_{ec}**	**dimer**	**V_{ec}**
00:00:00_m1:m3	49.0	00:01:00_m1:m1	127.5
00:00:00_m1:m0	29.5	01:01:01_m1:m0	10.1
00:00:00_m0:m3	19.8	01:01:00_m1:m1	2.1
01:00:00_m0:m1	11.2	00:00:00_m0:m1	1.3
01:00:00_m1:m2	8.9	01:01:00_m0:m0	0.1
01:00:00_m1:m3	2.6		
01:-1:00_m0:m2	1.8		
01:00:00_m0:m0	1.0	01:00:00_m0:m0	2.1
00:01:00_m0:m0	$1 \cdot 10^{-2}$	00:01:00_m0:m0	127.5
00:00:01_m0:m0	$6 \cdot 10^{-6}$	00:00:01_m0:m0	$3 \cdot 10^{-4}$

transfer rate (Eq. 2.37) quadratically, mobilities and diffusion constants should be maximal along this direction.

Taking these transfer integrals as input for the calculation of diffusion constants and mobilities following the protocol of Stehr et al.[94] results in the values summarized in table 4.7. As expected from table 4.6 the diffusion constants are in the same order of magnitude for all separate directions in α-perylene. Transport along the b-direction is slightly favored to the other directions. However, the situation is totally different in the β-polymorph. Not only is the isotropic hole mobility in β-perylene greater by a factor of 6 than in α-perylene, but the transport is strongly favored along the b-direction, as the coupling between monomers along the b-axis is very high (127.5 meV) compared to the other dimers (≤ 10.1 meV), and due to the very short monomer distance of only 5.84 Å between monomers in b-direction. A three dimensional representation of the hole mobility in β-perylene is depicted in figure 4.6.

To achieve the best performance in devices which need hole transport along a specific direction (e.g. field effect transistors or organic bilayer solar cells), the perylene β-polymorph should be taken and turned that the c-axis matches the transport direction given by the device. For applications where transport in all directions is more important, α-perylene presents itself as the more balanced choice.

Table 4.7 Calculated diffusion coefficients D in 10^{-6} m^2/s for hole transport in α- and β-perylene at T = 300 K and F = 10^7 V/m. D is given for isotropic diffusion as well as along the cell axes a, b and c.

	α	**β**
D_{iso}	3.5	21.9
D_a	2.2	2.0
D_b	4.8	63.0
D_c	3.3	0.4

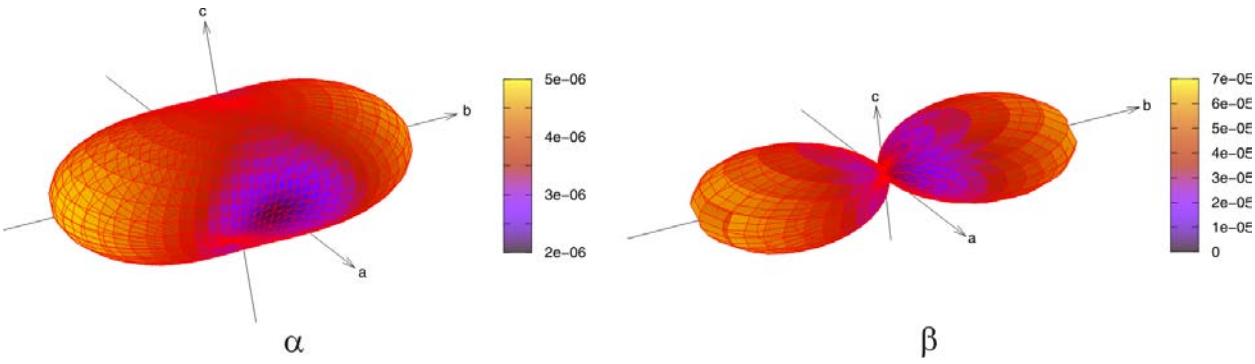

Figure 4.6 Three dimensional representation of the diffusion constants for hole transport in perylene. Whereas the α-polymorph shows rather isotropic mobility with only a slight preference towards the b-direction, the diffusion in β-perylene is strongly dominated in the b-direction with almost negligible diffusion along the c-axis.

4.2.2 Electron Transport

Table 4.8 contains the most important couplings for electron transport in perylene for both polymorphs. The highest values are found within the unit cell, where the dimers with the shortest intermolecular distances form π-stacks: 3.415 Å in α in 00:00:00_m1:m3, and 3.46 Å in β in 00:00:00_m0:m1. Transport between dimers composed of translation symmetric monomers play a less important role in α-perylene as the couplings are negligible small. The situation is different in β-perylene, where strong couplings can be found between translational symmetric monomers along the a- and b-direction. However, the dimer representing the c-direction (00:00:01_m0:m0) is very weakly coupled with a V_{ec} of only $3 \cdot 10^{-7}$ meV. A full list of couplings for electron transport in perylene is found in the appendix.

Simulations of diffusion coefficients are given in table 4.9 for isotropic movement and along the cell axes. The 3D representation is depicted in figure 4.7. Interestingly, transport in c-direction with a diffusion constant of $12.4 \cdot 10^{-6}$ m^2/s is strongly favored in β-perylene, although the corresponding dimer 00:00:01_m0:m0 is the weakest coupled dimer in table 4.8. Contributions from zig-zag pathways provide the explanation, as the strongest coupling in table 4.8 for 00:00:00_m0:m1 is also found in the symmetry equivalent dimers 00:00:01_m1:m0, 00:01:01_m1:m0 and

Table 4.8 Dimers in α- and β-perylene with the most important couplings in meV regarding electron transport. The lower part represents the coupling between dimers along the cell axes.

alpha		beta	
dimer	**V_{ec}**	**dimer**	**V_{ec}**
00:00:00_m1:m3	74.2	00:00:00_m0:m1	52.5
00:00:01_m2:m0	54.0	00:01:00_m0:m0	23.8
00:00:00_m1:m3	43.3	01:00:00_m0:m0	15.4
00:00:00_m1:m0	26.6	01:01:01_m1:m0	10.8
01:00:00_m0:m3	10.4	01:-1:00_m0:m0	1.3
01:00:00_m0:m1	5.2	01:01:00_m0:m0	0.2
01:00:00_m0:m0	9.1	01:00:00_m0:m0	15.4
00:01:00_m0:m0	$5 \cdot 10^{-2}$	00:01:00_m0:m0	23.8
00:00:01_m0:m0	$4 \cdot 10^{-5}$	00:00:01_m0:m0	$3 \cdot 10^{-7}$

00:01:00_m1:m0. However, these dimers do never include combinations between monomers outside the b-c-plane. Thus, diffusion is smallest along the a-axis in β-perylene. The α-polymorph also shows that the best transport occurs along the b-axis, although the coupling in 00:01:00_m0:m0 is very weak ($V_{ec} = 5 \cdot 10^{-2}$ meV).

Table 4.9 Calculated diffusion coefficients D in 10^{-6} m^2/s for electron transport in α- and β-perylene at T = 300 K and F = 10^7 V/m. D is given for isotropic diffusion as well as along the cell axes a, b and c.

	α	**β**
D_{iso}	6.7	7.0
D_a	2.0	3.5
D_b	11.3	5.3
D_c	6.8	12.4

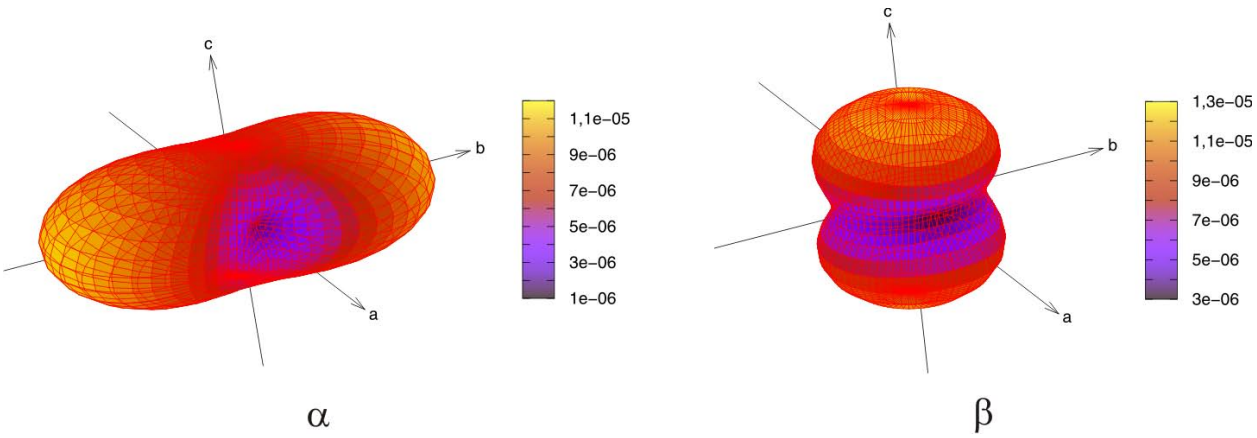

Figure 4.7 Three dimensional representation of the diffusion constants for electron transport in perylene.

To validate the results the mobilities μ were calculated for electron transport in α-perylene and compared to experimental values taken from Ref.191. These are displayed in table 4.10, which shows good agreement. Simulation of the mobilities have been done following the protocol given by Stehr *et al.*[94] at T = 300 K and an electric field strength of 10^7 V/m (field direction along the corresponding cell axis).

Table 4.10 Comparison between simulated (this work) and experimental[191] electron mobilities μ (given in cm^2/Vs) in α-perylene at T 300 K and F = 10^7 V/m.

direction	μ (sim.)	μ (exp.)	error (%)
a	0.71	0.78	8.9
b	4.08	5.53	26.2
c	2.36	2.37	0.4

5. [2.2]Paracyclophanes as Strongly Interacting π-Systems

5.1 Structural Features of [2.2]Paracyclophanes and Derivates

The following chapter describes studies on [2.2]paracyclophane (PC) and its derivates mono-hydroxy[2.2]paracyclophane (MHPC, *racemic*-4-hydroxy[2.2]para-cyclophane), *pseudo-ortho*-dihydroxy[2.2]paracyclo-phane (*o*-DHPC 4,12-dihydroxy-[2.2]paracyclophane) and *pseudo-para*-dihydroxy[2.2]paracyclophane (*p*-DHPC 4,16-dihydroxy-[2.2]-paracyclophane). The numbering of the atoms is shown exemplarily in figure 5.1, and their most stable structures in their ground and excited states in figure 5.2.

The specification of the irreducible representations of the D_2 and D_{2h} symmetric species is ambiguous as the three C_2 axes in these point groups are equivalent such that the main axis is not defined. Following the idea of the proposal of Mulliken[192] and the recommendation of the IUPAC convention, [193] we define the C_2 axis through the center of the -$(CH_2)_2$- bridge as *z*, the axis through the two benzene rings as *y*, and the remaining axis as *x*.

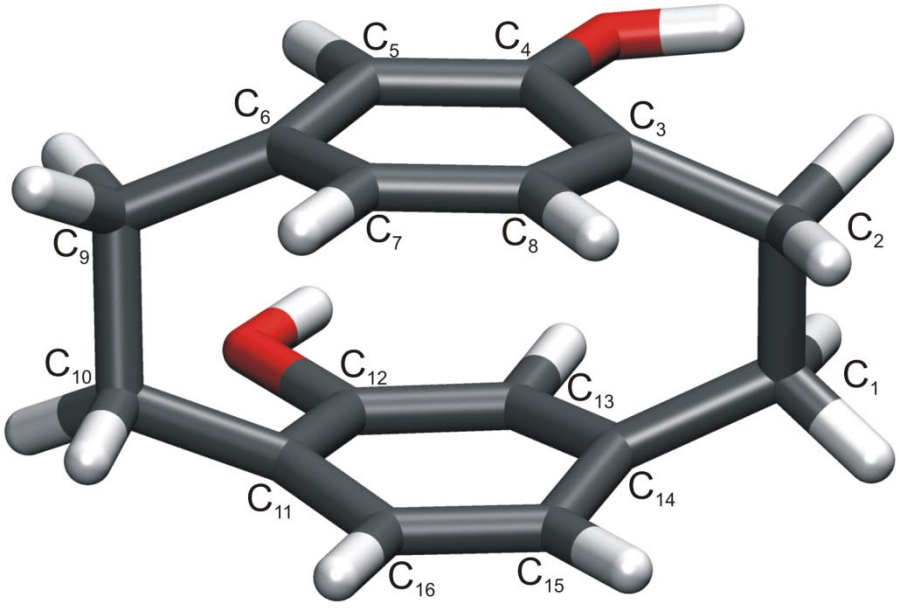

Figure 5.1 Molecular structure and labels represented by the *EZ*-rotamer of *o*-DHPC

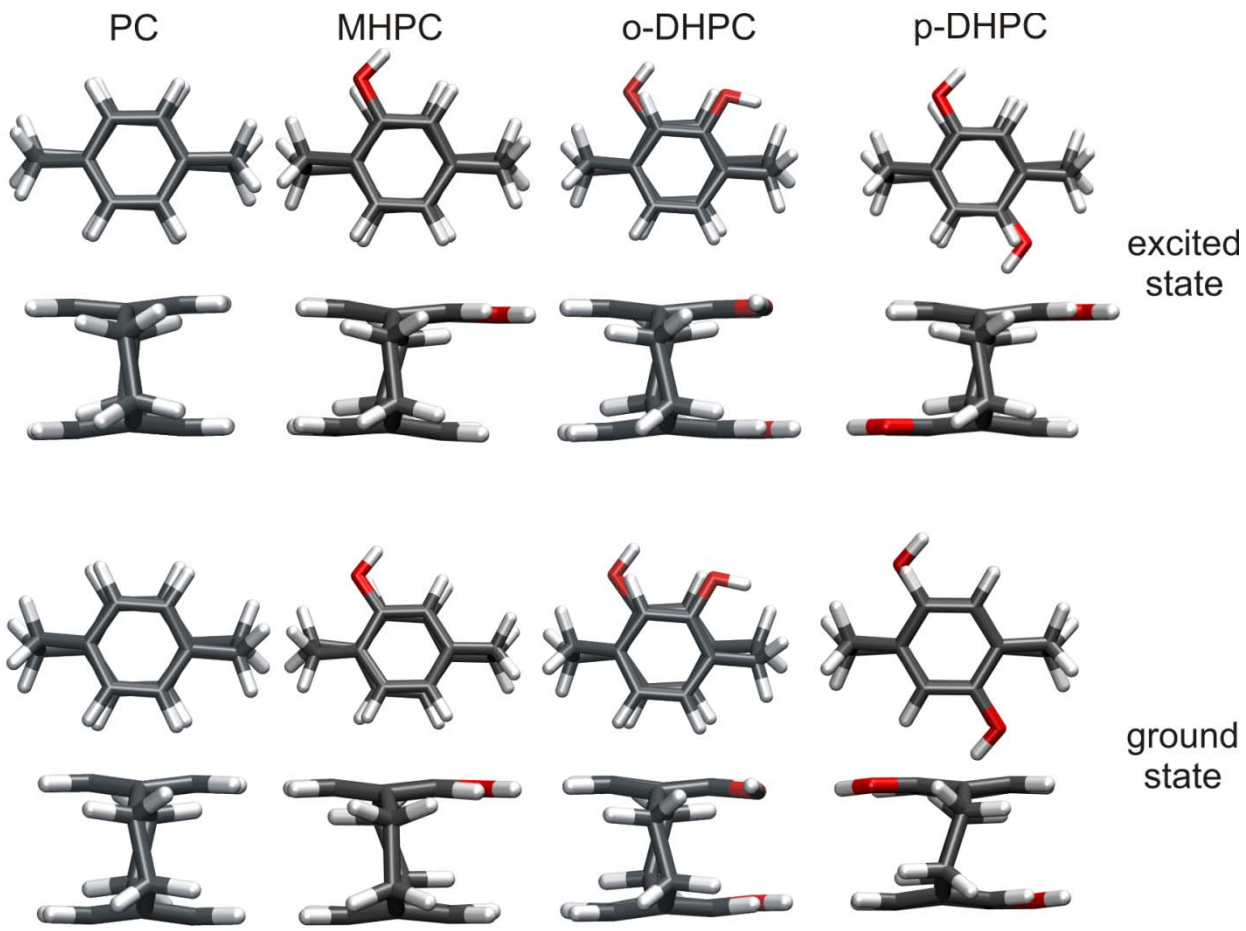

Figure 5.2 [2.2]Paracyclophane (PC), mono-hydroxy[2.2]paracyclophane (MHPC, *E*-rotamer), *pseudo-ortho*- (*o*-DHPC, *EZ*-rotamer) and *pseudo-para*-dihydroxy[2.2]paracyclophane (*p*-DHPC, *EE*-rotamer) shown in different perspectives in their ground and excited state structures.

The most important geometrical parameters for these compounds are the C_1-C_2 bond length, the inter-ring distances R(C_3-C_{14}) and R(C_4-C_{13}), and the angles θ_{twist} and θ_{shift}. The latter correspond to the twist and shift motions of the aromatic subsystems towards each other, *i.e.* twist around the y-axis, shift parallel to the x-axis. These angles are represented by a linear combination of dihedral angles as

$$\theta_{twist} = \frac{1}{8} [\theta(C_1\text{-}C_2\text{-}C_3\text{-}C_4) + \theta(C_1\text{-}C_2\text{-}C_3\text{-}C_8) + \theta(C_2\text{-}C_1\text{-}C_{14}\text{-}C_{13}) + \theta(C_2\text{-}C_1\text{-}C_{14}\text{-}C_{15})$$

$$+ \theta(C_{10}\text{-}C_9\text{-}C_6\text{-}C_5) + \theta(C_{10}\text{-}C_9\text{-}C_6\text{-}C_7) + \theta(C_9\text{-}C_{10}\text{-}C_{11}\text{-}C_{12}) + \theta(C_9\text{-}C_{10}\text{-}C_{11}\text{-}C_{16})], \quad (1)$$

and

$$\theta_{shift} = \frac{1}{8}[\theta(C_1\text{-}C_2\text{-}C_3\text{-}C_4) + \theta(C_1\text{-}C_2\text{-}C_3\text{-}C_8) + \theta(C_2\text{-}C_1\text{-}C_{14}\text{-}C_{13}) + \theta(C_2\text{-}C_1\text{-}C_{14}\text{-}C_{15}) - \theta(C_{10}\text{-}C_9\text{-}C_6\text{-}C_5) - \theta(C_{10}\text{-}C_9\text{-}C_6\text{-}C_7) - \theta(C_9\text{-}C_{10}\text{-}C_{11}\text{-}C_{12}) - \theta(C_9\text{-}C_{10}\text{-}C_{11}\text{-}C_{16})], \quad (2)$$

where $\theta(C_a\text{-}C_b\text{-}C_c\text{-}C_d)$ represents the dihedral angle between the respective atoms. This definition ensures that the twisting and shifting motions are performed in a symmetric fashion.

5.2 Experiments

5.2.1 Synthesis and Crystal Structure Determination

Racemic MHPC was purchased from ABCR GmbH and used without further purification. The synthesis of *p*-DHPC via iron-catalyzed dibromination of [2.2]paracyclophane followed by dilithiation with butyllithium and oxidative quenching with nitrophenol has been carried out as described in the literature.[194] To yield single crystals suitable for X-ray analysis the product has been recrystallized from ethanol. Racemic *o*-DHPC (97% purity) was acquired from ABCR GmbH. Single crystals suitable for X-ray analysis were obtained by recrystallization from methanol. For both *p*-DHPC and *o*-DHPC the crystal structure data were collected at a Bruker D8 diffractometer with an Apex CCD area detector and graphite monochromated $Mo_{K\alpha}$ radiation. The structure was solved using direct methods, refined with the Shelx software package[195] and expanded using Fourier techniques. All non-hydrogen atoms were refined anisotropically. Hydrogen atoms were assigned idealized positions and were included in structure factors calculations.

Crystal data for *p*-DHPC·$(EtOH)_2$: $C_{20}H_{28}O_4$, M_r = 332.42, colorless block, 0.37×0.36×0.35 mm^3, monoclinic space group $P2_1/c$, a = 8.2875(11) Å, b = 13.1716(18) Å, c = 8.3272(11) Å, β = 102.735(2)°, V = 886.6(2) $Å^3$, Z = 2, ρ_{calcd} = 1.245 $g \cdot cm^{-3}$, μ = 0.085 mm^{-1}, $F(000)$ = 360, T = 168(2) K, R_1 = 0.0457, wR^2 = 0.1248, 1758 independent reflections [$2\theta \leq 52.16°$] and 112 parameters.

Crystal data for *o*-DHPC·0.5MeOH: $C_{16.5}H_{18}O_{2.5}$, M_r = 256.31, colorless block, 0.43×0.26×0.185 mm^3, monoclinic space group C2/*c*, a = 24.937(5)Å, b = 7.8461(14)Å, c = 13.183(2)Å, α = 90.00°, β = 95.655(3)°, γ = 90.00°,

V = 2566.8(8)Å^3, Z = 8, ρ_{calcd} = 1.326 g·cm^{-3}, μ = 0.088 mm^{-1}, F(000) = 1096, T = 172(2) K, R_1 = 0.0644, wR^2 = 0.1961, 3210 independent reflections [$2\theta \leq 56.68°$] and 182 parameters.

Crystallographic data have been deposited with the Cambridge Crystallographic Data Center as supplementary publication no. CCDC–809116 (*p*-DHPC) and CCDC-809117 (*o*-DHPC). These data can be obtained free of charge from The Cambridge Crystallographic Data Centre via www.ccdc.cam.ac.uk/data_request/cif.

5.2.2 Experimental Setup of the [1+1]REMPI-Spectra

The exact experimental conditions are described in Ref.181-183. In general, the substances were spread out on glass wool and placed in the sample compartment of a modified solenoid valve. The source was heated to approximately 150 °C to evaporate the test substance which was seeded in 1.1 bar of Ar. Control experiments with He were also carried out. The molecular beam was formed and cooled by expanding the mixture of cyclophane and carrier gas into vacuum through a 0.5 mm diameter nozzle.

The vacuum apparatus consisted of a source chamber and a rotary pump and an ionization chamber equipped with a 0.4 m long Wiley-McLaren type time–of–flight (TOF) mass spectrometer perpendicular to the molecular and laser beam. The ionization chamber and the flight chamber were pumped by turbomolecular pumps backed by a rotary pump. The source and the ionization chamber were connected by a gate valve. In front of the gate a skimmer was fixed with an aperture of 1 mm. During the experiment the pressure in the ionization chamber was lower than 3×10^{-6} mbar. The skimmed jet was crossed by a perpendicular laser beam.

The experiments were performed with a nanosecond laser system consisting of a 10 Hz Nd:YAG laser pumping a grazing incidence dye laser, operating with DCM in ethanol. The dye laser output was frequency-doubled in a potassium dihydrogen phosphate (KDP) crystal and the laser beam diameter was reduced to 3 mm by a pinhole. The energy of the laser was varied between 0.5 and 5 mJ/pulse, corresponding to fluences from 7 to approximately 75 mJ/cm². The overall appearance of the spectrum did not depend on the laser power.

The molecules were excited and ionized by the [1+1] REMPI scheme. The wavelength was calibrated using a hollow cathode lamp filled with neon. In the

Wiley-McLaren time–of–flight mass spectrometer the ions were accelerated by fields of 250 V/cm and 730 V/cm, respectively, and detected by a microchannel plate detector (chevron assembly). The signals were recorded by a digital–storage oscilloscope, typically averaged over 50 shots, and transferred to a computer. The experimental setup was synchronized using a digital delay generator.

The experimental data was verified by [1+1'] REMPI experiments and by the additional method of spectral hole burning (SHB) to check for the presence of molecular isomers. A second laser system consisting of a Nd:YAG and dye laser was used for that purpose. The two laser beams were counterpropagating and adjusted temporally and spatially in the excitation region.

5.3 Computational Details

All calculations were perfomed with the TURBOMOLE program suite Version 5.10.[196] The structures of all molecules were optimized in the ground and first excited states. The theoretical investigations were done using a wide range of methods: (Time dependent) Hartree Fock and Density Functional Theory were applied using the TZV basis of Schäfer *et al.*[197] augmented with the (2df,2pd) polarization functions. The functionals used include the General Gradient Approximation-type (GGA) BP86[198] and PBE[156] functionals as well as the hybrids B3LYP[155] and BHLYP.[157] The dispersion correction of Grimme[199] has been applied for BP86 and PBE for both structure optimizations as well as adiabatic excitation energies denoted by BP86-d and PBE-d. Furthermore BP86 and PBE used the resolution of identity (RI) approximation[176, 177] with the TZV auxiliary basis sets of Weigend *et al*.[200] augmented with (2df,2pd) polarization functions. Second order Møller-Plesset perturbation method[201] (MP2), the approximate coupled cluster second order method[153] (CC2) and its spin-component scaled variants SCS-MP2[202, 203] and SCS-CC2[150-153] also applied the TZV basis sets of Schäfer *et al.*,[197] but only (2df,p) polarization functions were used as augmentation. All MP2 and CC2 calculations applied the RI approximation[176, 177] using the auxiliary basis sets of Weigend *et al.*[204] Zero point vibrational energies (ZPEs) were calculated on all levels of theory using a SV(P) basis set.[205] Vibrational frequencies shown were scaled by a factor of 0.95, which is commonly applied on this level of theory to account for anharmonicity of the

potentials and errors of the method.[206-208] Electrostatic potentials have been generated by the RICC2 module of the TURBOMOLE program suite.

5.4 Ground State Structures

5.4.1 Different Approaches in Comparison

The first step in the investigations on [2.2]paracyclophane is a correct description of the geometric structure of the parent compound and its hydroxyl substituted derivates. The results for different methods are summarized in table 5.1 and compared to X-ray structures for PC and *p*-DHPC.

While covalent bond lengths are well described in all methods the non-bonded inter-ring distances R(C_3-C_{14}) and R(C_4-C_{13}) deviate from the crystal structure. Generalized gradient approximation-type functionals (BP86 and PBE) reproduce the ground state structures of PC qualitatively correct. The inter-ring distances are overestimated by 4 - 5 pm. Improvements can be achieved by the use of Grimme´s dispersion correction,[199] which introduces bonding van der Waals interactions which are not included in normal DFT. Although the distances are now underestimated, the errors narrow down to 1 - 2 pm. The dispersion correction does not affect the twist or shift angle as these functionals reproduce perfectly the experimental value of 9°. Adding exact exchange (Hartree Fock exchange) to the functional (20 % in B3LYP, 50% in BHLYP, 100% in HF) increases the inter-ring distances slightly to the overall worst values (errors of 6 – 7 pm). Additionally, B3LYP is not able to provide even only qualitatively correct picture, as the D_{2h} structure ($\theta_{shift} = \theta_{twist} = 0°$) is predicted to be the global minimum. Recent studies of Bachrach[209] show that medium- or long-range exchange and dispersion corrected functionals like M06-2x,[210] B97-D[199] and ωB97X-D[211] also perform very nicely for the ground state structure of PC. Optimizations with MP2 give shorter distances (error of -6 pm) which is to be expected, whereas this error is less pronounced (-3 pm) for the spin-component-scaled variant SCS-MP2. θ_{shift} and θ_{twist} are found to be slightly overestimated (underestimated) by (SCS-)MP2 (HF and BHLYP). In *p*-DHPC the situation is similar. Pure GGA functionals overestimate inter-ring distances, dispersion corrected

Table 5.1 Relevant structure parameters of the ground (gs) and first excited states (es) of PC and p-DHPC for different methods (TZV(2df,2pd) basis set for all methods but (SCS-)MP2/CC2, which uses a TZV(2df,p) basis set). Distances (R) are given in pm, angles (θ, definition see text) in degrees.

molecule	parameter	BP86	BP86-d	PBE	PBE-d	B3LYP
	$R(C_1\text{-}C_2)$	161 / 158	161 / 158	161 / 158	160 / 160	161 / 158
	$R(C_3\text{-}C_{14})$	282 / 264	279 / 262	282 / 263	279 / 262	283 / 253
PC	$R(C_4\text{-}C_{13})$	315 / 294	308 / 289	314 / 293	309 / 290	316 / 278
gs / es	$R(C_8\text{-}C_{15})$	315 / 294	308 / 289	314 / 293	309 / 290	316 / 278
	θ_{twist}	9 / 4	9 / 9	9 / 5	9 / 9	0 / 10
	θ_{shift}	0 / 0	0 / 0	0 / 0	0 / 0	0 / 0
	$R(C_1\text{-}C_2)$	161 / 159	160 / 159	160 / 159	160 / 158	160 / 158
	$R(C_3\text{-}C_{14})$	280 / 272	277 / 267	280 / 271	277 / 267	281 / 265
p-DHPC	$R(C_4\text{-}C_{13})$	312 / 305	304 / 292	311 / 304	305 / 294	313 / 293
gs / es	$R(C_8\text{-}C_{15})$	311 / 305	303 / 294	310 / 303	304 /296	312 / 298
	θ_{twist}	1 / 16	0 / 35	1 / 16	0 / 16	0 / 11
	θ_{shift}	12 / -4	18 / 13	12 / -5	17 / -5	12 / -4

molecule	parameter	BHLYP	(TD)HF	MP2/CC2	SCS-MP2/ SCS-CC2	experiment
	$R(C_1\text{-}C_2)$	159 / 157	160 / 157	159 / 157	159 / 159	159 / ---
	$R(C_3\text{-}C_{14})$	280 / 261	283 / 266	274 / 253	276 / 257	278 / ---
PC	$R(C_4\text{-}C_{13})$	316 / 291	317 / 298	304 / 278	307 / 283	310 / ---
gs / es	$R(C_8\text{-}C_{15})$	316 / 291	317 / 298	304 / 278	307 / 283	310 / ---
	θ_{twist}	6 / 6	6 / 6	14 / 10	13 / 7	9 / ---
	θ_{shift}	0 / 0	0 / 0	0 / 0	0 / 0	0 / ---
	$R(C_1\text{-}C_2)$	159 / 156	160 / 157	159 / 157	159 / 157	159 / ---
	$R(C_3\text{-}C_{14})$	279 / 261	282 / 268	271 / 252	274 / 256	276 / ---
p-DHPC	$R(C_4\text{-}C_{13})$	310 / 286	315 / 306	298 / 276	302 / 281	305 / ---
gs / es	$R(C_8\text{-}C_{15})$	310 / 299	314 / 315	297 / 280	301 / 286	305 / ---
	θ_{twist}	0 / 11	0 / 15	0 / 15	0 / 12	0 / ---
	θ_{shift}	12 / 4	11 / 0	21 / -4	20 / -2	13 / ---

variants reproduce the crystal structure to a very good agreement. Interestingly θ_{shift} and θ_{twist} are better reproduced without dispersion in this compound. Exact exchange does not have a systematic effect, as BHLYP reproduces angles as well as distances in good agreement, while HF greatly overestimates distances and B3LYP lies in between. However, B3LYP performs unsatisfactorily again, as it predicts almost an eclipsed D_{2h} structure. Finally MP2, and to a lesser degree SCS-MP2, underestimate the distances while overestimating the twist angle.

The performance of the different methods can be summarized as follows: dispersion corrected GGA functionals give the best ground state structures, followed by SCS-MP2. MP2 is as good as BP86 and PBE, with MP2 underestimating and BP86 and PBE overestimating distances. BHLYP performs ok, but pure HF as well as B3LYP have the worst accuracy, since distances have the largest errors and B3LYP additionally results in qualitatively wrong structures compared to the crystal structures.

In this work we will focus on SCS-MP2 as well as SCS-CC2 and not on dispersion corrected GGA functionals. The reason for this is described in section 6.7: The most

Table 5.2 Ground state (gs) structures calculated with SCS-MP2 and excited state (es) structures calculated with SCS-CC2 for PC, MHPC, o-DHPC and p-DHPC. Both methods applied TZV(2df,p) basis sets. Distances (R) are given in pm, angles (θ, definition see text) in degree.

parameter	PC (gs/es)	o-DHPC (gs/es)	p-DHPC (gs/es)	MHPC (gs/es)
$R(C_1\text{-}C_2)$	159 / 159	159 / 157	159/ 157	159 / 157
$R(C_3\text{-}C_{14})$	276 / 257	274 / 258	274 / 256	274 / 257
$R(C_4\text{-}C_{13})$	307 / 283	296 / 280	302 / 281	301 / 281
$R(C_8\text{-}C_{15})$	307 / 283	311 / 286	301 / 286	306 / 288
θ_{twist}	±13 / 7	16 / 13	0 / 12	-10 / 11
θ_{shift}	0 / 0	0 / 0	20 / -2	-11 / 3

accurate excitation energies can be reproduced with SCS-CC2 and to avoid inconsistencies this method was also chosen for the description of the structures. The calculated SCS-MP2/SCS-CC2 ground and excited state structures for all compounds are shown in figure 5.2 and the most relevant structures are collected in table 5.2. The experimental values for PC, *o*-DHPC and *p*-DHPC can be found in table 5.3. For MHPC no X-ray structure is available.

Table 5.3 Experimental ground state structures taken from X-ray diffraction data for PC, o-DHPC and p-DHPC. Distances (R) are given in pm, angles (θ, definition see text) in degree.

parameter	**PC**	**o-DHPC**	**p-DHPC**
$R(C_1\text{-}C_2)$	159	157	159
$R(C_3\text{-}C_{14})$	278	277	276
$R(C_4\text{-}C_{13})$	310	302	305
$R(C_8\text{-}C_{15})$	310	308	305
θ_{twist}	9	9	0
θ_{shift}	0	-6	13

5.4.2 Rotamers in Hydroxy-Sustituted [2.2]Paracyclophanes

X-ray crystal structures are available for all compounds but MHPC. Nevertheless, the orientation of the hydrogen atoms within the hydroxyl groups was not addressed experimentally. This is due to the limitation of X-ray diffraction to determine the positions of hydrogens, especially when these are bound to atoms with high electron density. Hydrogen atoms depicted in X-ray structures are normally assigned idealized positions and are included in structure factors calculations.[195] However, to address some questions for the interpretation we calculated the different rotamers as well. Depending on the orientation of the hydroxyl groups two rotamers are possible in MHPC and three in *p*-DHPC and *o*-DHPC. They are termed *ZZ*, *EZ* and *EE* isomers, where *E* (*Z*) designates a hydrogen atom pointing away (towards) the $–(CH_2)_2–$ bridge. See figure 5.3 for a depiction and the relative energies of the rotamers. For *p*-DHPC the *EE* isomer was calculated to be 3.4 kJ/mol and 5.9 kJ/mol

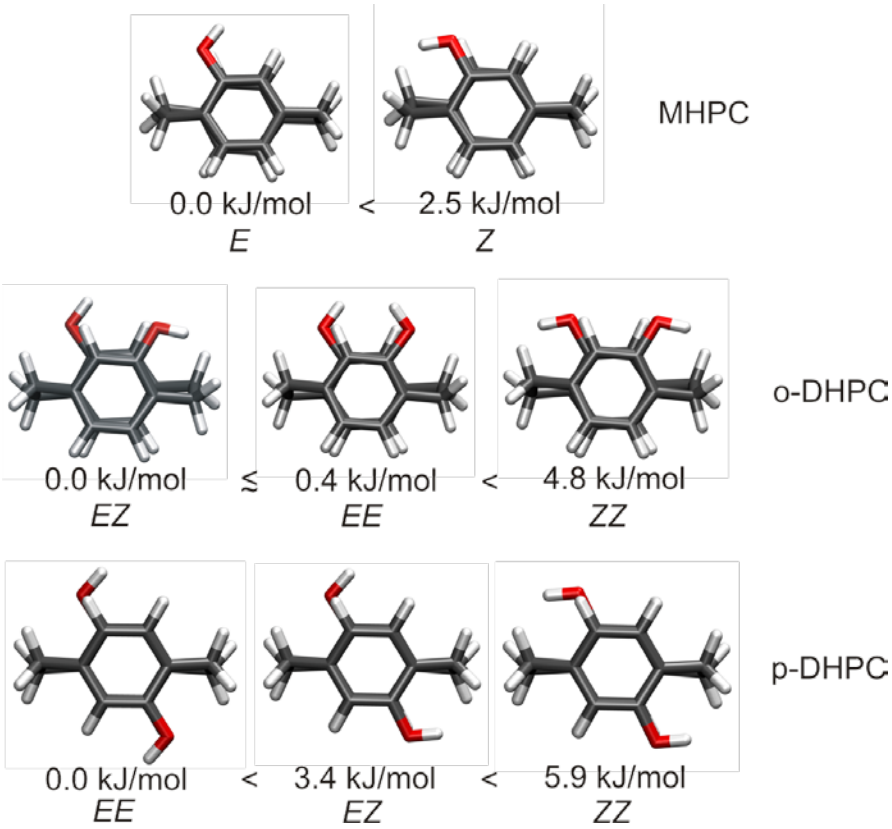

Figure 5.3 Relative energies of the different rotamers for the hydroxyl-substituted derivatives.

more stable than the *EZ* and *ZZ* isomers, respectively. Thus, the *EE* isomer represents the ground state minimum structure and will be the isomer we discuss throughout the rest of this work. For *o*-DHPC *EZ* is calculated to be the most stable conformation, being 0.4 kJ/mol and 4.8 kJ/mol lower in energy than the *EE* and *ZZ* isomers, respectively. Finally, the *E* isomer is 2.5 kJ/mol more stable than *Z* in MHPC.

5.4.3 Two Dimensional Ground State Potential Energy Plots

To quantify structural differences between the compounds, we calculated two dimensional potential energy surfaces as a function of the two internal coordinates θ_{twist} and θ_{shift} that correspond to the twist and shift motion of the benzene rings. For the definition of the angles see section 5.1. Figure 5.4 shows the potential energy surfaces for all compounds obtained by optimizing the structure for fixed θ_{shift} and θ_{twist} at the SCS-MP2/TZV(2df,p) level of theory. The global minima can also be

Table 5.4 Ground state (gs) structures calculated with SCS-MP2 and excited state (es) structures calculated with SCS-CC2 for PC, MHPC, o-DHPC and p-DHPC. Both methods applied TZV(2df,p) basis sets. Distances (R) are given in pm, angles (θ, definition see text) in degree.

parameter	PC (gs/es)	o-DHPC (gs/es)	p-DHPC (gs/es)	MHPC (gs/es)
$R(C_1\text{-}C_2)$	159 / 159	159 / 157	159/ 157	159 / 157
$R(C_3\text{-}C_{14})$	276 / 257	274 / 258	274 / 256	274 / 257
$R(C_4\text{-}C_{13})$	307 / 283	296 / 280	302 / 281	301 / 281
$R(C_8\text{-}C_{15})$	307 / 283	311 / 286	301 / 286	306 / 288
θ_{twist}	±13 / 7	16 / 13	0 / 12	-10 / 11
θ_{shift}	0 / 0	0 / 0	20 / -2	-11 / 3

taken from table 5.4. The distortion from the eclipsed structure (D_{2h}, θ_{twist} = 0° and θ_{shift} =0°) to the corresponding minimum results in an energy gain of 1.2 kJ/mol, 4.6 kJ/mol, 5.3 kJ/mol and 7.2 kJ/mol for PC, MHPC, *o*-DHPC and *p*-DHPC, respectively. These numbers and figure 5.4 demonstrate that PC itself is very flexible with respect to the twist and shift motions. Although this has been pointed out in earlier investigations,[202, 212-214] it should be noted, that substitution leads to significantly more rigid derivates. Additionally, table 5.5 summarizes the energies of the different compounds in the (next) global minimum ground state structure of the other derivates.

Table 5.5 Stabilization energies of PC, MHPC, o-DHPC and p-DHPC relative to the eclipsed structure (D_{2h}, θ_{twist} = 0° and θ_{shift} = 0°) for the ground state minimum structures of the other compounds. Angles (θ_{twist} and θ_{shift}) are given in degree, energy in kJ/mol.

$\theta_{twist}/\theta_{shift}$	PC	o-DHPC	p-DHPC	MHPC
0 / 0	1.2	5.3	7.2	4.6
±13 / 0	0.0	0.3	6.1	1.5
-16 / 0	0.1	0.0	6.2	5.8
0 / 20	2.4	7.4	0.0	10.6
-10 / -11	0.9	7.5	2.4	0.0

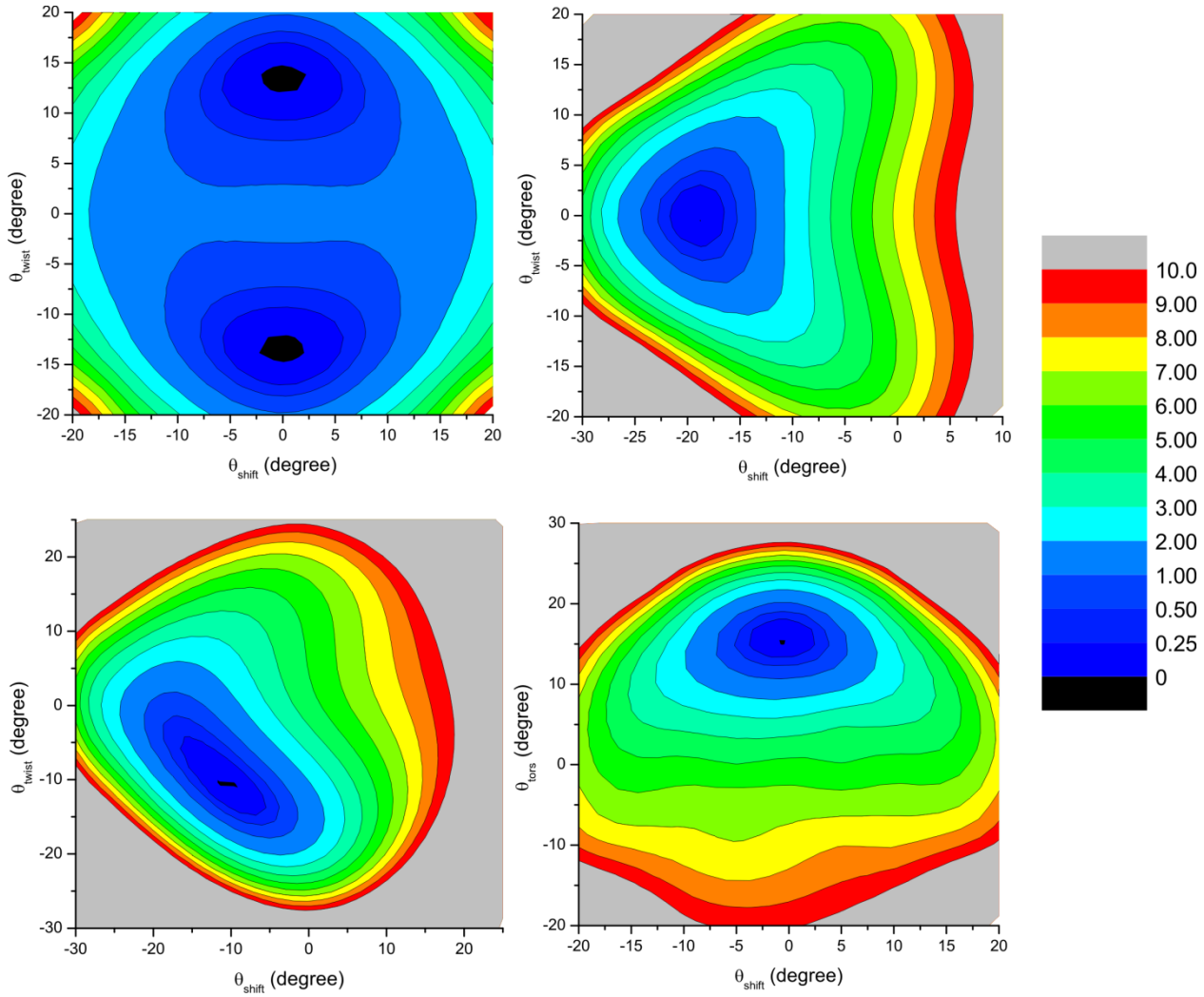

Figure 5.4 Ground state potential energy surfaces with respect to the angles θ_{twist} and θ_{shift} for the PC (top-left), MHPC (bottom-left), *p*-DHPC (top-right) and *o*-DHPC (bottom-right) molecules.

5.5 Excited State Structures

While the results of different approaches for the structure are also summarized in table 5.1, we will discuss in this paragraph only SCS--CC2/TZV(2df,p) results, as these are expected to be qualitatively the correct states (no charge transfer states) and quantitatively the correct values. In the first singlet excited states of all compounds the benzene subunits move towards each other. According to our SCS-CC2/TZV(2df,p) calculation the inter-ring distances decrease by 16-25 pm.[183, 202] While in PC and *o*-DHPC only the inter-ring distance and θ_{shift} decrease from 13°

to 7° and 16° to 13°, respectively. Nevertheless, both molecules maintain their ground state structure. In contrast to this, the equilibrium structure of *p*-DHPC changes dramatically upon excitation. On the one hand the shift is essentially removed, even inversed (θ_{shift} = +20° to θ_{shift} = -2°), on the other hand the excited state structure exhibits a former non-existing twist distortion (θ_{twist} = +12°). In contrast to the ground state the excited state structure of *p*-DHPC has the same qualitative properties as the other compounds. The global minimum structure of MHPC in the excited state is found for θ_{twist} = +11°. However, another local minimum is found for θ_{twist} = -10°, which is only 34 cm^{-1} (59 cm^{-1} if ZPE corrections are taken into account) higher in energy. Their shift angles do not differ considerably (global minimum: θ_{shift} = +3°, local minimum θ_{shift} = 0°). The energy barrier at θ_{twist} = 0° was calculated to be 64 cm^{-1} (no ZPE correction). The local minimum resembles the qualitative structural properties of the ground state whereas the global minimum has an inverse twist angle. In preceding calculations on MHPC the excited state was optimized for fixed θ_{twist} with a SV(P) basis set. There, the minima were found at θ_{twist} = ±15°, their energy difference was 43 cm^{-1}, and the barrier at θ_{twist} = 0° was 133 cm^{-1}. Thus, it can be expected that the barrier in reality is even smaller and the absolute values of θ_{twist} at the minima are also slightly smaller than the SCS-CC2/TZV(2df,p) values mentioned above.

5.6 Analysis of Ground and Excited State Structures

5.6.1 HOMO and LUMO Orbitals

While covalent bond lengths are well described in all methods the non-bonded inter- ring distances deviate from the crystal structure due to their HOMO and LUMO orbitals, which are depicted in figure 5.5. The orbitals shown are plotted for the eclipsed D_{2h} structure of PC for a better visualization and represent the HOMOs and LUMOs of all phanes. The HOMOs contribute to the explanation of the twisted ground state structures in PC, *o*-DHPC and MHPC as the plus and minus phases of the benzene subunits cause the rings to repel each other. The twist and shift displacement reduces this. The situation for the LUMO orbitals is the opposite. There, the phases have the same sign in both benzene subunits resulting in a bonding π-like character. In MP2 treatments double excitations depopulate

antibonding HOMO and populate LUMO orbitals. Thus, steric (Pauli) repulsion is reduced and inter-ring distances decrease. This effect is overestimated by standard MP2 and described more correctly by the SCS-MP2 approach. The HOMO and LUMO orbitals also explain the decreased inter-ring distances in the excited state relative to the ground state. Following the argumentation for the MP2 method, excitation promotes electrons from antibonding HOMOs to bonding LUMOs which causes the benzene subunits to approach each other. Furthermore, the values of θ_{twist} are lowered as the occupation of the twist-favoring HOMOs is reduced and that of the stack-favoring LUMOs increases.

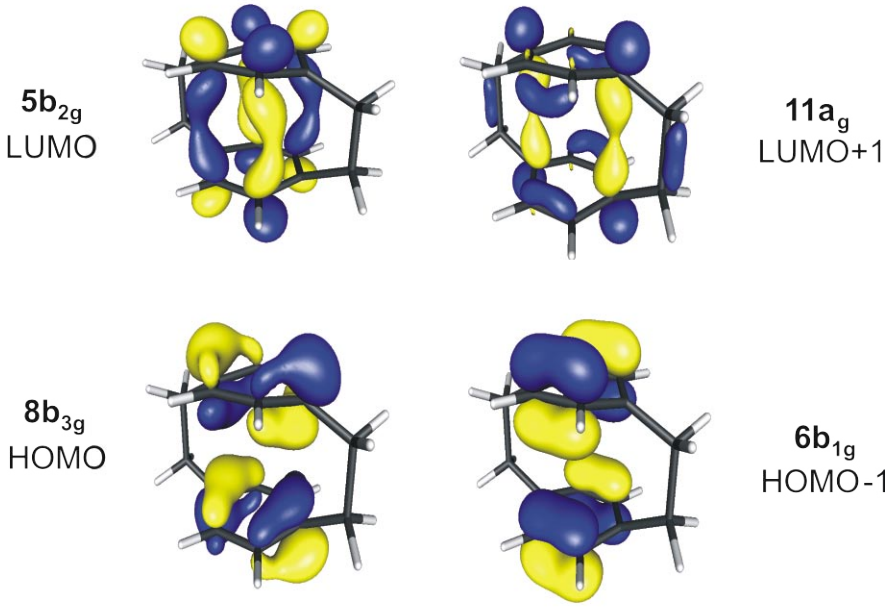

Figure 5.5 HOMO and LUMO orbitals of PC in the eclipsed D_{2h} structure.

5.6.2 Electrostatic Potential

Structural differences between the compounds can be correlated to the electrostatic potential between the benzene rings as follows: In paracyclophanes the aryl carbon atoms bonded to the bridges (C_3, C_6, C_{11}, C_{14}) give rise to a significant positive excess charge. This is visible from the ground state electrostatic potential of the PC molecule in its D_{2h} structure shown in figure 5.6 (a). The positive charge cloud in the plane between the two aromatic rings arises from the pyramidalization of these carbon atoms, the charge penetration of the π-orbitals and their exchange

repulsion. These effects cause that electron density is moved to the outer side of the molecule. For all compounds, both twist and shift motions of the molecule reduce the electrostatic interaction of the aromatic systems. Simultaneously, the Pitzer strain connected with the eclipsed conformation of the bridge C−H-bonds in the D_{2h}-structure is likewise lowered. The shifted structure of *p*-DHPC is caused by the electrostatic attraction between the negatively charged oxygen atoms and the positively charged aryl C-atoms bound to the bridge at the opposite benzene subunits. Additionally, the shift allows the positively charged hydrogen of the hydroxyl group to get closer to the negative potential caused by the π-system. A shift in the structure of o-DHPC does not lower its energy, as it does not result in a net attractive electrostatic interaction. Any attractive interaction is compensated on the corresponding other side of the molecule. Hence, we conclude that the small shift of -6° in the crystal structure is a packing effect. Due to the absence of a second hydroxyl group MHPC has the most asymmetric electrostatic potential. MHPC can maximize the attraction between its hydroxyl group and the positive charge cloud not only with a twist motion like PC, but additionally with a shift. This is unique, as the other compounds show either a twisted or shifted ground state structure.

To explain structural changes due to excitation, the electrostatic potential for the excited state is shown in Fig. 5.6 (b), and the difference potential between ground and excited state in Fig. 5.6 (c). Due to the shift in the ground state structure of *p*-DHPC, the negatively charged hydroxyl groups approach the positively charged region between the benzene rings. Upon excitation the regions between the non-bridge aryl carbon atoms and the hydrogen atoms bonded to them acquire a larger amount of electron density. This repels the hydroxyl groups, and the *p*-DHPC molecule changes its structure drastically as the shift disappears (20° to -2°) and is replaced by a twist (0° to 12°) for further stabilization. Compared to the ground state structures *o*-DHPC and PC have less twisted structures in the excited state. MHPC is the only compound with two minimum structures in the excited state. The local minimum has the same qualitatively structural features as the ground state structure regarding its twist coordinate (excited state: θ_{twist} = -10°, ground state: θ_{twist} = -10°), but the shift vanishes. In contrast, the global minimum has opposite sign for the twist coordinate (θ_{twist} = + 11). Since both excited state structures do only differ in energy

by 59 cm^{-1}, an explanation of the excited state structures given by the electrostatic potential is not reasonable.

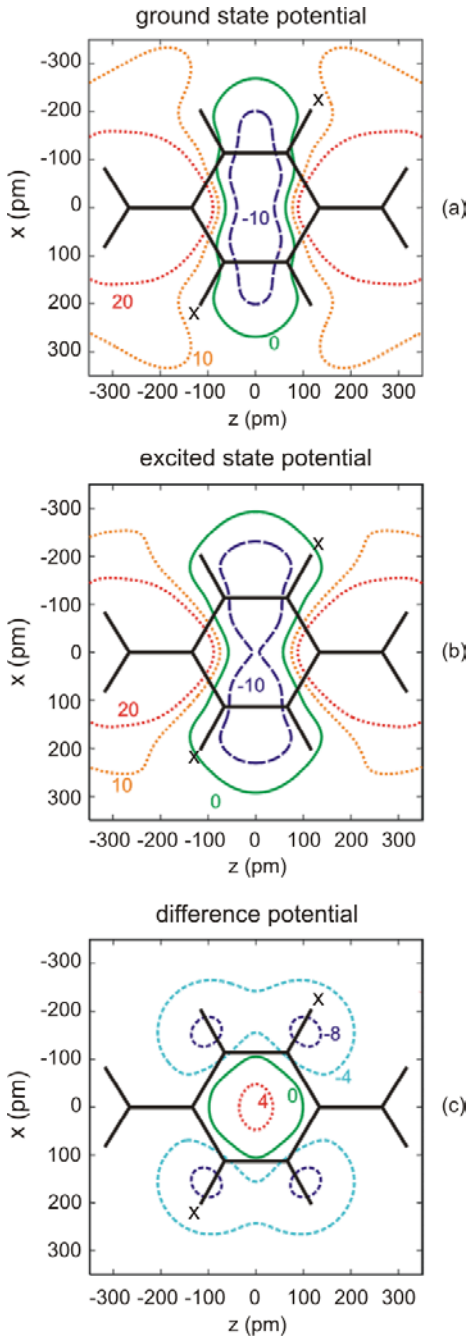

Figure 5.6 Electrostatic potential in the plane between the two benzene subunits in the eclipsed *D*2h structure of PC for the (a) ground and (b) excited state. (c) shows the difference potential between both states. Values of the contours in 10^{-3} au are indicated. X indicates the position of the hydroxyl oxygen atom in *p*-DHPC.

5.7 Adiabatic Excitation Energies

5.7.1 Finding the Appropriate Method

For the present study the use of a certain method is not justified only by its ability to reproduce the correct ground state structure. The reproduction of the correct excitation energy is even more crucial. Our original goal was to explain the reversed order in experimental excitation energies between benzene, phenol and their corresponding covalently bound dimers PC and *p*-DHPC. Figure 5.7 shows that the $S_1 \leftarrow S_0$ transition in benzene is bigger by 0.19 eV than phenol. In comparison to the dimers this order is reversed, as PC has an excitation energy of 3.82 eV and *p*-DHPC 3.90 eV. Only SCS-CC2 was able to reproduce the correct energetical order. First, the reversed order was tried to be rationalized by the Davydov splitting concept (section 2.2). By identifying the E_1 and E_2 states, which are the plus and minus linear combinations of the corresponding monomers, the calculated coupling was found to be too similar (0.53 eV in PC, 0.47 eV in *p*-DHPC) to be used as the sole explanation.

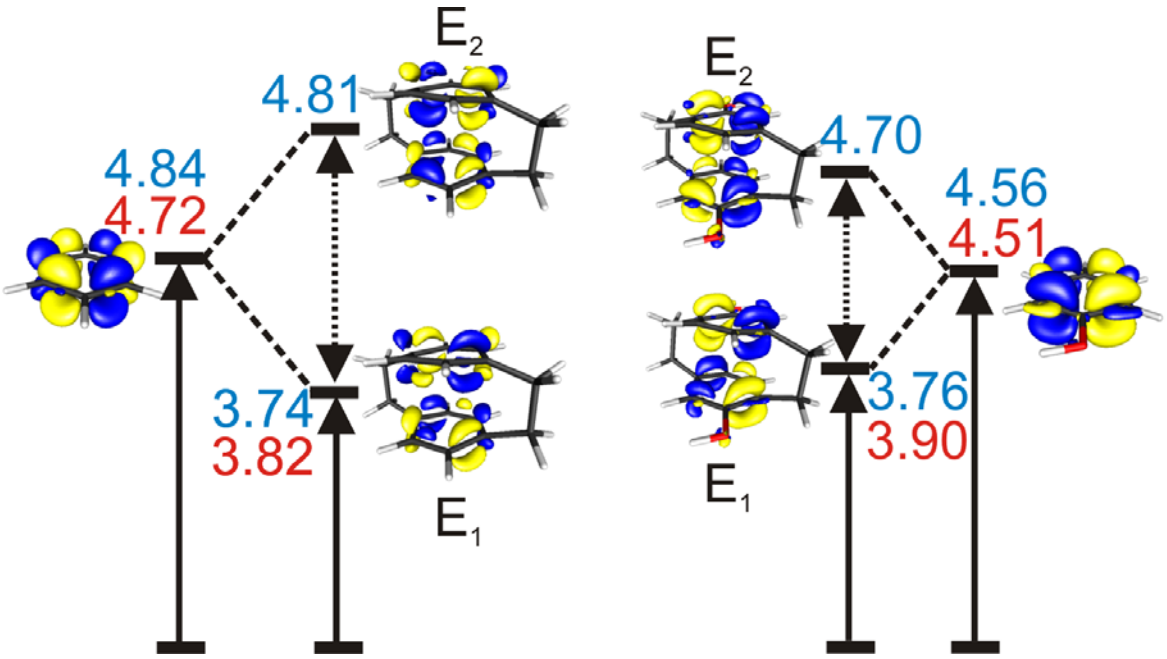

Figure 5.7 Davydov splitting in benzene, phenol and their corresponding covalently bound dimers PC and *p*-DHPC. Experimental (red) and calculated excitation energies (blue, SCS-CC2 / TZV(2df,p)) are given in eV.

Although the direction of our studies changed over time, it is still very important to evaluate carefully different approaches towards each other. Only a method which excels in all categories, *i.e.* structure and excitation energy, is appropriate. Therefore we tested the methods described in section 5.4.1 for their ability to predict correct excitation energies. As the [1+1]REMPI experiment provides adiabatic excitation energies, it is not sufficient to calculate the simpler vertical excitations, but to optimize the excited state first. A general scheme for excitation energies is shown in figure 5.8. Adiabatic excitation energies without ZPE corrections for benzene, phenol, PC and *p*-DHPC calculated with different approaches are shown in table 5.6. Benzene and phenol were calculated as these systems represent the aromatic subunits which are responsible for the Davydov splitting. A correct description of these seemed essential to analyze the reversed order in excitation energies. Although dispersion corrected GGA functionals (BP86-d and PBE-d) give nice results for phenol (error of +0.11 each) their deviation for benzene (+1.11 eV / +1.14 eV) and the investigated phanes PC and *p*-DHPC (-0.29 eV / -0.27 eV and -0.50 eV / -0.50 eV) are too large. The performance of the hybrid functionals B3LYP and BHLYP as well as TDHF is even worse for the monomer subunits (errors up to

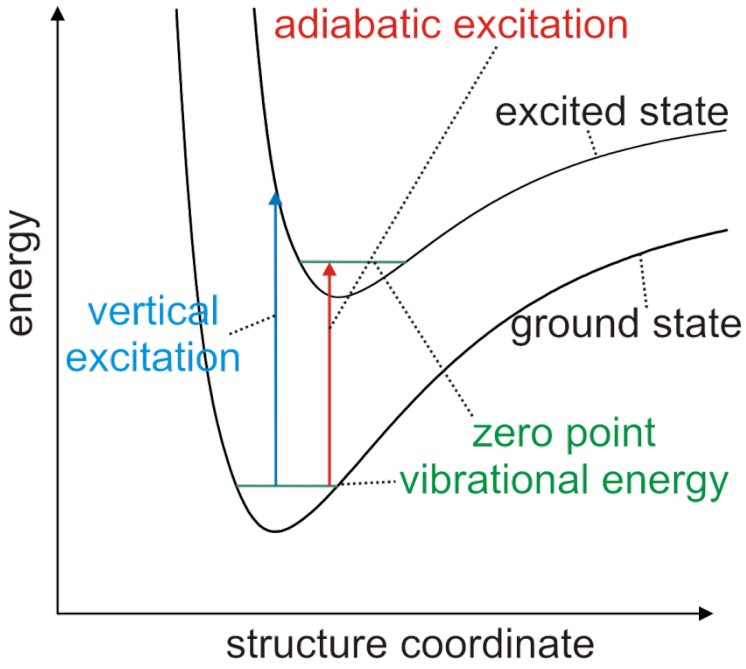

Figure 5.8 The difference between a vertical excitation and an adiabatic excitation including zero-point vibrational energy.

+1.14 eV) and still not good enough for the phanes (errors up to +1.02 eV). CC2 and its spin-component scaled variant SCS-CC2 perform significantly better. The latter reduces the errors to less than +0.22 eV and is therefore the method of choice to describe these systems.

Table 5.6 Adiabatic excitation energies without zero-point vibrational energy. All values are given in eV.

method	benzene	phenol	PC	p-DHPC
BP86-d	5.83	4.62	3.53	3.38
PBE-d	5.86	4.62	3.55	3.38
B3LYP	5.99	4.93	4.02	3.85
BHLYP	6.11	5.30	4.41	4.30
TDHF	5.86	5.58	4.84	4.71
CC2	5.12	4.82	3.85	3.82
SCS-CC2	4.94	4.71	3.89	3.88
experiment	4.72	4.51	3.82	< 3.88

5.7.2 Zero-Point Vibrational Energies

Since our calculations are to be compared to experimental [1+1]REMPI spectra a calculation of zero-point vibrational energies (ZPEs) is obligatory. The result is the vibrational spectrum and additionally a correction to the adiabatic excitation energies. Table 5.7 contains the results for the most important methods applied to our systems. It is obvious that the best results in comparison to the experiment are obtained by the SCS-CC2 method. The errors for the monomer systems benzene and phenol decrease to less than 0.07 eV, for the phanes even to less than 0.04 eV. Note that the excitation energy of *p*-DHPC cannot be determined experimentally as this will be discussed later. Less accurate but still reasonable values are produced by the CC2 method. For comparison the results of TD-B3LYP are shown. Although they give nice energies for several systems, this method totally fails for benzene. In addition it was shown in section 5.4.1, that B3LYP produces the qualitatively wrong

Table 5.7 Adiabatic excitation energies including zero-point vibrational energy. All values are given in eV.

method	benzene	phenol	PC	o-DHPC	p-DHPC
TD-B3LYP	5.70	4.61	3.89	3.94	3.73
CC2	4.95	4.67	3.71	3.80	3.67
SCS-CC2	4.79	4.56	3.78	3.87	3.71
experiment	4.72	4.51	3.82	3.90	< 3.88

structures for the ground and excited state. Therefore, this method should not be used.

Note, that in most applications ZPEs are calculated not on the demanding level of SCS-CC2. Instead the cheaper level of B3LYP is used and added to the adiabatic excitation energy of most of the more demanding methods. The results show that this is not an option for these π-systems. Whereas SCS-CC2 corrects the adiabatic excitation energies of benzene, phenol, PC and its dihydroxy derivates by 0.11 – 0.18 eV, B3LYP corrections differ from SCS-CC2 by -0.06 eV to +0.17 eV for the same compounds. *I.e*. the zero point correction at the TD-B3LYP level actually introduces errors of a similar magnitude as the corrections themselves and should, thus, not be used for SCS-CC2 excitation energies of such compounds.

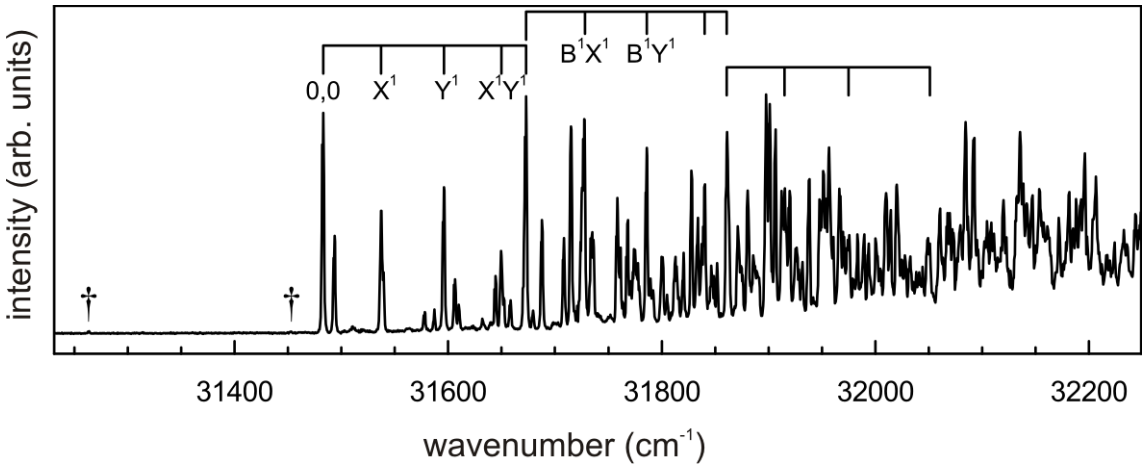

Figure 5.9 REMPI spectrum of *o*-DHPC. The vertical marks indicate progressions of the most prominent modes, see text for details.

5.8 [1+1]REMPI Spectra

[1+1]REMPI spectra have been recorded for [2.2]paracyclophane[215, 216] and its hydroxy derivates.[181-183] Figure 5.9 shows in the upper trace the spectrum of pure *o*-DHPC and in the lower trace its cluster with one water molecule. The low-wavenumber part in more detail (31230 cm^{-1} to 31750 cm^{-1}) is depicted in figure 5.10. The absolute wavenumbers are correct to within ± 2 cm^{-1}, the relative wavenumbers in figure 5.10 to within ± 1 cm^{-1}. Both figures, the experimental results and the discussion of the spectra of *o*-DHPC, can be found in Ref.183. Theoretical simulations and experimental [1+1]REMPI spectra of *o*-DHPC and *p*-DHPC in comparison are depicted in figure 5.11. Figure 5.12 shows the experimental REMPI spectrum of MHPC.

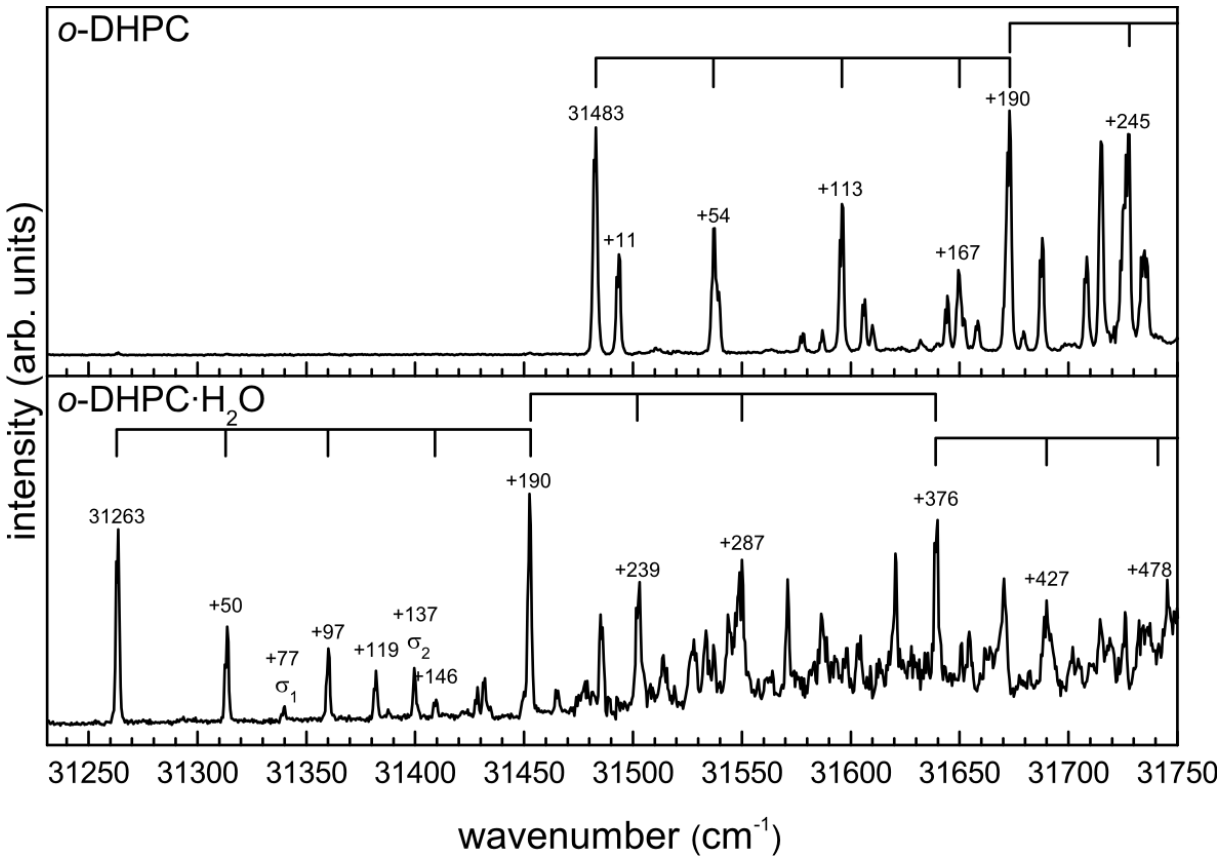

Figure 5.10 REMPI spectrum of *o*-DHPC (upper trace) and its water cluster *o*-DHPC·H_2O (lower trace) for the low-wavenumber region.

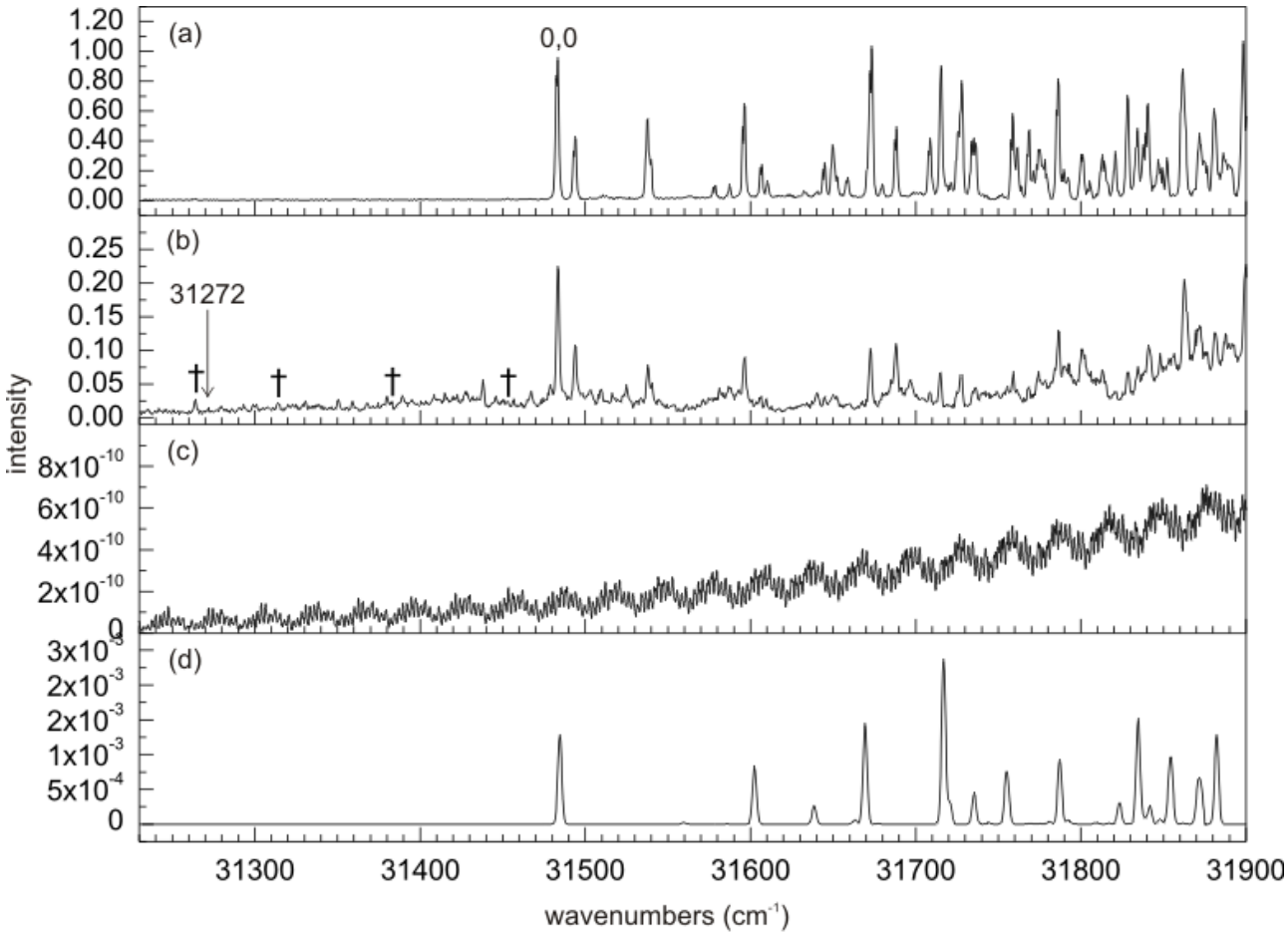

Figure 5.11 Experimental REMPI spectra of *o*-DHPC (a) and *p*-DHPC (b) as well as the calculated spectrum of *p*-DHPC (c) and o-DHPC (d). The intensity is given in arbitrary units for the experimental spectra and based on Franck-Condon factors for the simulated spectrum of *p*-DHPC. † denotes peaks from a fragmentation of the water cluster.

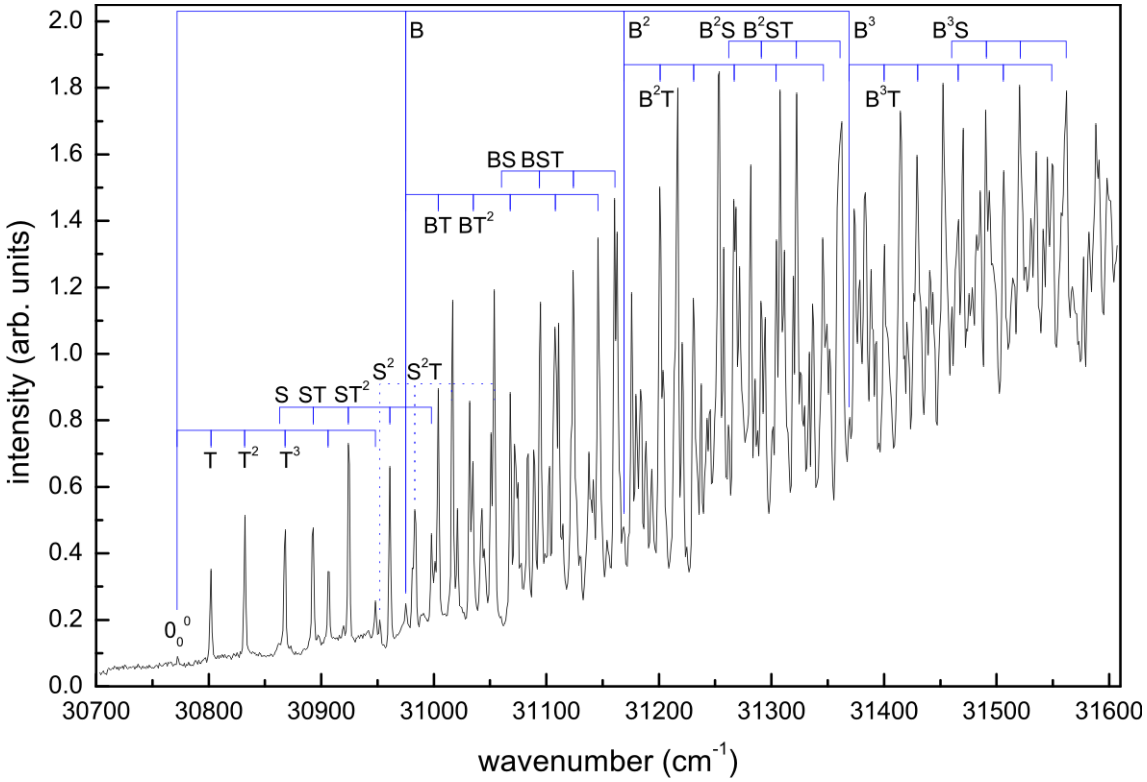

Figure 5.12 [1+1]REMPI spectrum of MHPC. Numerous progressions are identified, corresponding to twist (T), shift (S) and breathing (B) motion.

5.8.1 *o*-DHPC

Neglecting the $-(CH_2)_2-$ bridges *o*-DHPC can be regarded as two phenol units interacting like an H-aggregate, see section 2.2. Although the $S_1 \leftarrow S_0$ transition is usually forbidden for H-aggregates, here it is allowed due to lower symmetry and by vibronic coupling. Its origin is observed at 31483 cm^{-1}.

A progression is found of around 190 cm^{-1} with frequency vibration peaks at 31673 cm^{-1} (B^1, B = "breathing"), 31862 cm^{-1} (B^2) and 32052 cm^{-1} (B^3). Calculation of the vibrational spectrum results in a mode at +185 cm^{-1} in the S_1 state of the *o*-DHPC spectrum with significant breathing character. In PC a similar progression of up to eight quanta was observed in the excited state at 0,0+235 cm^{-1}.[215, 216] This fits nicely to the theory which predicts the breathing mode at +237 cm^{-1}.

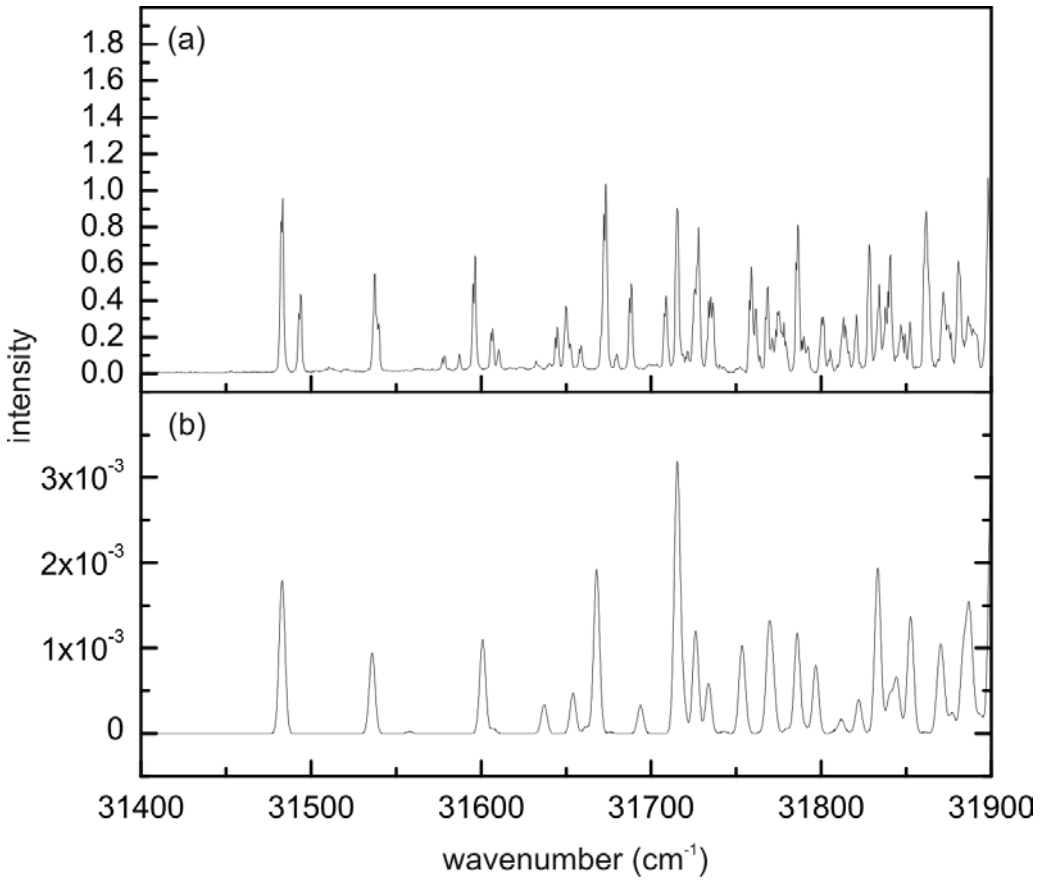

Figure 5.13 Experimental REMPI spectrum of o-DHPC (a) and simulation combining *EE*- and *EZ*-*o*-DHPC. The intensities in (b) are given as a sum over *EZ* and half of *EE*, whereas the latter was shifted by +55cm^{-1}. See text for more details.

The spectrum of *o*-DHPC also contains further progressions with lower frequencies at +55 cm^{-1}, +113 cm^{-1} and +168 cm^{-1}. However, an assignment is difficult. They might be the fundamental and the first two overtones of a mode X with an unusual anharmonicity. Alternatively, the +113 cm^{-1} mode can be assigned to a different low energy vibration Y and the band at +168 cm^{-1} to a combination band XY. Our experimental coworkers prefer the latter interpretation. Our calculations do not provide additional insight at this point. There are no modes which might explain the +55 cm^{-1} peak. A possible explanation might be given by another rotamer: *EE*-*o*-DHPC (*ZZ*-*o*-DHPC), which is calculated to be only 0.4 kJ/mol (4.8 kJ/mol) higher in energy than *EZ*-o-DHPC. The calculated $S_0 \leftarrow S_1$ transition energy is 53 cm^{-1} larger (119 cm^{-1} smaller) relative to *EE*-*o*-DHPC. To rule this possibility out additional studies both experimentally and theoretically have been conducted: We tried to use

our simulated spectra of both the *EE*- and *EZ*-rotamer to construct a combined REMPI spectrum, which might resemble the experiments. Various attempts have been made and the result is depicted in figure 5.13. Since the $S_0 \leftarrow S_1$ transition of the more stable *EZ*-isomer is lower by 53 cm^{-1} *EE* and *EZ* have been integrated by summing over the intensities of *EZ* and half of the intensities of *EE*, whereas the frequencies of *EE* have been shifted by +53 cm^{-1}. The contributions to the intensity by the *EE*-rotamer are halved to account for the statistical factor we get because there is only one EE-rotamer possible, but there are two combinations which result in an *EZ*-rotamer. The intensities (arbitrary units for the experiment, Franck-Condon-based for the simulation) have been scaled, that the 0,0 transition has the same intensity in both spectra to facilitate comparison. Although not all peaks are reproduced, many peaks of the experiment are found in the simulation. The question arises, if we now really have two different rotamers in the [1+1]REMPI experiment. Therefore, the experimentalists conducted spectral hole burning experiments. The results proved, that all transitions with strong intensity at 31483 cm^{-1}, +11 cm^{-1}, +55 cm^{-1}, +113 cm^{-1} and +190 cm^{-1} originate from the same ground state isomer, for details see Ref.183. However, from the experimental data it is not possible to say which rotamer is the carrier for the spectrum. Several other weak transitions observed between 31500 and 31700 cm^{-1} in the REMPI spectrum most likely originate from a second rotamer.

The origin of the +11 cm^{-1} band remains unsolved. Spectral hole burning excludes the possibility of a second rotamer as an explanation, nor is there any corresponding mode found in the simulations. Further hints to the assignment are obtained from the spectrum of the water cluster, see figure 5.10. The cluster itself is easily formed during the expansion of the molecular beam from residual water in the carrier gas.

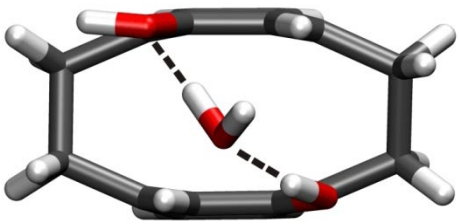

Figure 5.14 Most stable water cluster of *o*-DHPC.

Since the chromophores have two chromophores, and thus two binding sites, many cluster structures are possible making an unequivocal assignment difficult without further investigation. Therefore, the bands appearing in these spectra will not be discussed. SCS-MP2 calculations of the *EZ*-*o*-DHPC·H_2O cluster show that in the by far most stable structure the water molecule is inserted between both hydroxyl groups and interacts with both of them, see figure 5.14, resulting in a binding energy of 48.7 kJ/mol. For the *ZZ* rotamer a binding energy of 31.8 kJ/mol was computed, while for the *EE* isomer no stable structure was found with two hydrogen bonds. Although other structures with only one hydrogen bond have been found, their binding energies are significantly lower. Therefore, it can be assumed that only the cluster of the *EZ* rotamer will be present in a free jet. However, we do not see the +11 cm^{-1} band in the spectrum of the cluster. This vibration seems to be characteristic only for the monomer and indicates, that the associated motion is of little importance in the cluster. The water molecule seems to work like an anchor putting additional strain on modes associated with tilt or twist motion and might suppress excitation.

5.8.2 *p*-DHPC

The experimental spectrum of *p*-DHPC resembles the spectrum obtained for *o*-DHPC (see figure 5.11) and therefore yields almost no new data. All observed major peaks are identical to those found in the spectrum of pure *o*-DHPC. For an explanation of these see section 5.8.1. The difference between the experimental spectra arises in the additional large number of closely spaced peaks with comparably small intensities. Therefore, we assume that the major peaks in the spectrum of *p*-DHPC originate from contaminations of *o*-DHPC, while *p*-DHPC is only responsible for the noisy background. To test this hypothesis we recorded a REMPI spectrum of a 5:1 mixture of *p*-DHPC and *o*-DHPC. The results can be seen in figure 5.15. The signal intensity of the major peaks increases by a factor of 25 upon adding 16% of *o*-DHPC. This confirms the carrier of the intense bands is indeed *o*-DHPC. The only peaks that can be assigned to *p*-DHPC are lost in the magnified background noise of the mixture experiment. Note that impurities of the *para*-isomer do not affect the spectroscopy of the *ortho*-isomer.

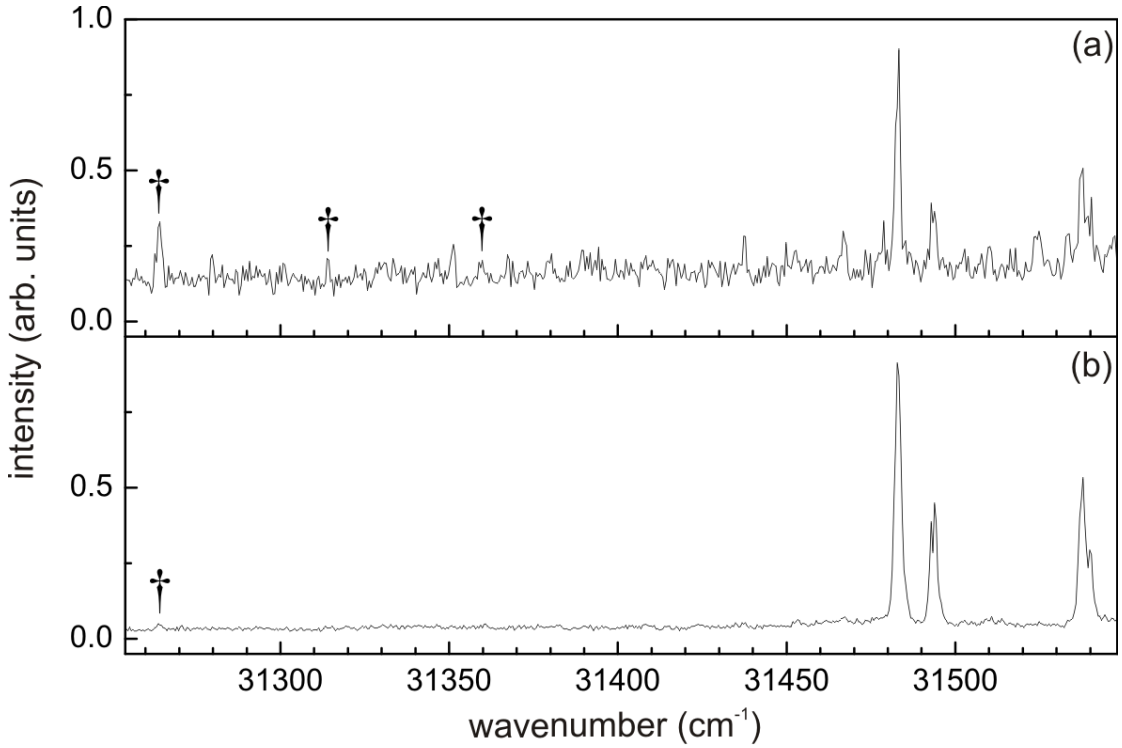

Figure 5.15 Experimental REMPI spectra of (a) pure *p*-DHPC (intensity multiplied by a factor of 25 for a better comparability) and (b) a 6:1 mixture between *p*-DHPC and *o*-DHPC. Small amounts of *o*-DHPC dominate the *p*-DHPC spectrum. The daggers indicate signals that are due to water clusters.

The first unambiguously assigned band of *p*-DHPC was found at 31272 cm^{-1} (3.88 eV). However, the origin of the $S_1 \leftarrow S_0$ transition in *p*-DHPC lies most likely at lower excitation energies. This value constitutes an upper bound, while the true origin should be significantly lower at around 3.71 eV according to the calculations, which is also significantly lower than that of *o*-DHPC. Above 31700 cm^{-1} *p*-DHPC gives rise to closely spaced signals in the REMPI spectrum that form a continuous background such that no individual bands can be assigned. The background is an order of magnitude smaller in the spectrum of *o*-DHPC.

A possible explanation for the appearance of *o*-DHPC in the *p*-DHPC spectrum could be a *para*-to-*ortho*-isomerization under the evaporation conditions in the REMPI experiment. Therefore, *p*-DHPC was sublimated, recondensated and then

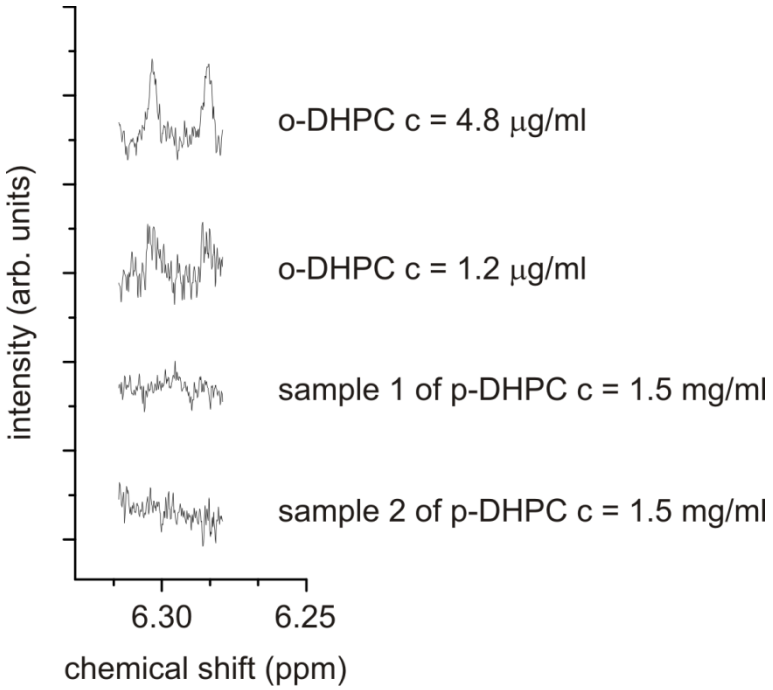

Figure 5.16 Section of ^{1}H-NMR-spectra (400 MHz, 295 K, 3000 scans, d_6-DMSO) including the signals of two chemically equivalent aromatic protons of the *o*-DHPC enantiomers. Spectra are shown for diluted *o*-DHPC in two different concentrations (4.8 µg/ml and 1.2 µg/ml) and two samples of *p*-DHPC (each 1.5 mg/ml). The spectra are shifted for better comparability.

investigated by NMR spectroscopy. The spectra prior and after this procedure are identical, which rules out that a significant amount of *p*-DHPC isomerizes to the *ortho* compound. The purity of the synthesized *p*-DHPC was determined by ^{1}H-NMR experiments. Figure 5.16 shows two diluted samples of *o*-DHPC in comparison to two samples of concentrated *p*-DHPC. While *o*-DHPC shows two signals at around 6.30 ppm no signal can be found in the spectra of *p*-DHPC. This shows that the contamination of *o*-DHPC in the spectra of *p*-DHPC is certainly less than 3 ‰.

In conclusion, to determine properties of *p*-DHPC experiments are insufficient, since the *p*-DHPC spectrum is dominated by *o*-DHPC. For an understanding of the processes associated electronic excitation a theoretical approach is necessary.

Figure 5.11 shows the simulations of the REMPI spectra of both *o*-DHPC (c) and *p*-DHPC (d). The most striking result is the difference in the intensities of both compounds. *o*-DHPC absorbs better by seven orders of magnitude. This confirms

that small impurities of *o*-DHPC will dominate the spectrum of *p*-DHPC. Furthermore, the simulation of *p*-DHPC results in many closely spaced peaks with increasing intensity, which are also found in the experimental REMPI spectrum. Note, that these peaks are missing in the experimental spectrum of *o*-DHPC. We conclude that the experimental spectrum of *o*-DHPC can mostly be explained by the simulation, while *p*-DHPC is a combination of both compounds, where all major peaks stem from the by far better absorbing *o*-DHPC and *p*-DHPC is responsible for the noisy background.

5.8.3 MHPC

Figure 5.12 shows the experimental [1+1]REMPI spectrum of MHPC. The absolute wavenumbers are correct to within ±2 cm^{-1}. As visible, the first peak appears with small intensity at 30772 cm^{-1}. A rich spectrum with a large number of transitions is observed. The band intensities grow continuously with increasing wavenumber, indicating a significant geometry change upon ionization. As the ionization energy was determined to be 7.63 eV,[182] *i.e.* very close to twice the excitation energy, additional [1+1´]REMPI experiments have been carried out. Since no further band was observed the transition at 30772 cm^{-1} (3.815 eV) was assigned the $S_1 \leftarrow S_0$ band origin of MHPC. This is in excellent agreement to the computed value of 3.79 eV. Spectral hole burning experiments excluded the possibility of two different rotamers.[182] Since the *E*-rotamer was computed to be 2.5 kJ/mol more stable than the *Z*-rotamer we assume this isomer to dominate the spectrum. The *Z*-rotamer is disfavored due to steric reasons and its population in the molecular beam is therefore assumed to be low. However, no experimental evidence such as a X-ray structure supports the stability of this isomer.

Although a simulation of the REMPI spectrum fails for this compound due to the strong anharmonicity of the twist vibration (see below) and the neglect of Duschinsky Mixing in our simulation, significant activity in modes corresponding to the twist and shift motion is expected. The most obvious pattern in the low energy region of the spectrum is a number of bands with a spacing of roughly 30 cm^{-1}. Upon closer inspection an inverse anharmonicity is observed: Bands are found at 30802 cm^{-1} (+30 cm^{-1}), 30832 cm^{-1} (+60 cm^{-1}), 30868 cm^{-1} (+96 cm^{-1}), 30906 cm^{-1} (+134 cm^{-1})

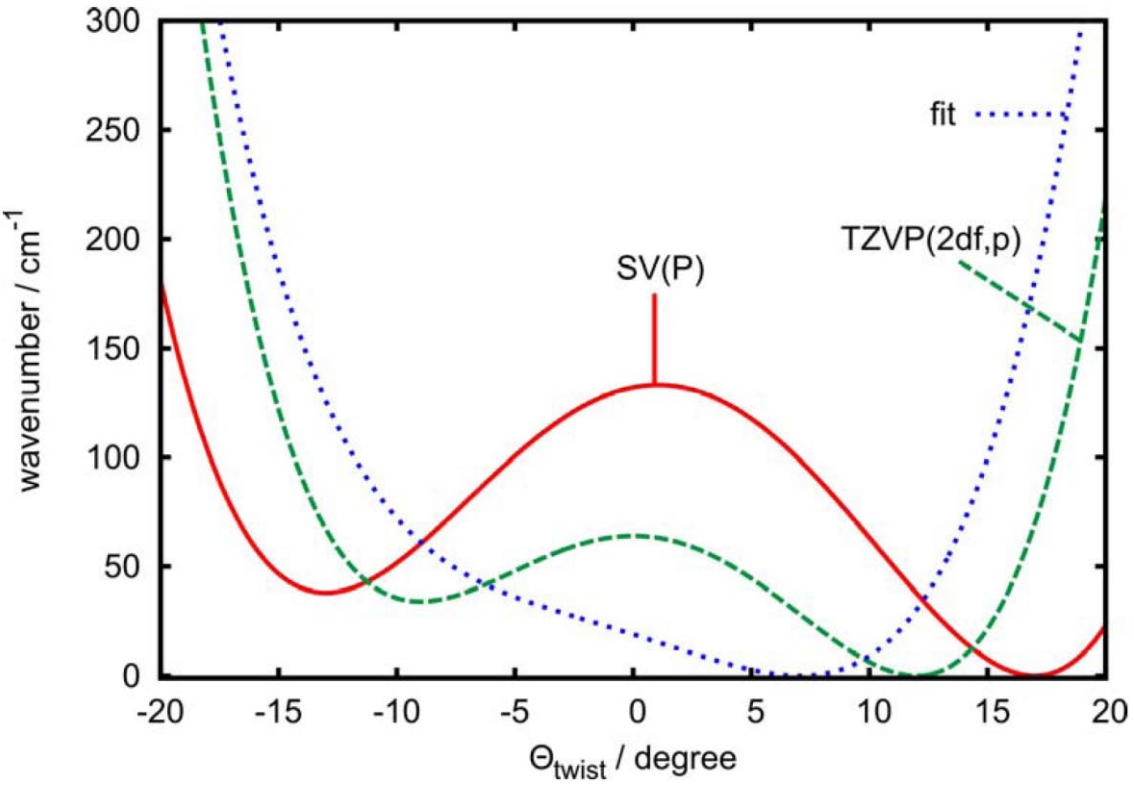

Figure 5.17 The potential energy curves of the excited sate of MHPC as a function of the twist coordinate at different levels of theory. The SV(P) [TZV(2df,p)] curve is the curve, obtained by optimizing the structure of the molecule for given θtwist values at the SCS-CC2/SV(P) [SCSCC2/TZV(2df,p)] level. The fitted curve is a fourth order polynomial that provides relative term energies and intensities fitting best to the corresponding experimental values.

and 30948 cm^{-1} (+176 cm^{-1}). Since the same pattern can be found at higher wavenumbers, it is assumed that these bands belong together and are denoted with the letter T in figure 5.12. A theoretical analysis along the twist coordinate in the excited state shows a double minimum potential with a small barrier between both minima. The θ_{shift} angle changes only slightly from 0° to 3° between both minima. Therefore, a strong coupling between twist and shift is not expected in the S_1 state. This is in contrast to the ground state, where a strong coupling between both motions is found, see figure 5.4. However, the shape of this cut depends strongly on the basis set employed: Using the SV(P) basis set, the global minimum is found at

θ_{twist} = +16° and the second at θ_{twist} = -13°, 38 cm^{-1} higher in energy. A barrier between these local minima was found for θ_{twist} = 0° which is 132 cm^{-1} above the global minimum. By improving the basis set to TZV(2df,p) θ_{twist} is reduced from +16° to +11° (-13 to -10°) in the global minimum (local minimum). While the relative energy between both is essentially not affected (34 cm^{-1}) the barrier drops to 64 cm^{-1}. Thus, the question arises, if the existence of two minima is just a basis set effect. Both potential energy curves are shown in Figure 5.17. As the calculated barrier is significantly smaller than the accuracy of the method, the present calculations do not allow to deduce unambiguously whether there is a barrier or not in the true potential. As an additional approach the shape of the excited state potential was fitted to the experimental spectrum, obtaining the potential shown in figure 5.18. The resulting term wavenumbers and intensities are collected in table 5.9 for all three potential energy curves, and their full representations as fourth-order polynomials are listed in table 5.9. The fitted potential does not provide a second minimum. However, it is significantly flattened towards negative θ_{twist}–values. Thus, the trend of the basis set improvement as well as the fitted potential energy curve indicate, that the potential energy curve may have only a single minimum, but a very flat potential energy curve in the region -10° < θ_{twist} < 10°. Even better results would be provided by a two-dimensional analysis including the coupling of shift and twist motion in the excited state. However, due to the size of the molecule and the necessary basis set for a qualitatively reasonable description, a 2D-analysis was too demanding.

For the shift mode a progression is easily identified: Assignment of the bands as 30863 cm^{-1} (+91 cm^{-1}, S) and 30952 (+180 cm^{-1}, S^2) results in a roughly spacing of 90 cm^{-1}, which fits to the calculated value of 85 cm^{-1}. Combination bands of both shift and twist are also found in the experimental spectra labelled ST, ST^2 etc. in figure 5.12. Furthermore, combination bands of the first overtone of the shift mode, S^2 with the twist mode are also observed.

Finally, a breathing mode B associated with a decrease in the inter-ring distance is expected to be active in MHPC. [1+1]REMPI experiments of PC and *o*-DHPC show such a mode at +235 cm^{-1} and 190 cm^{-1}, respectively. MHPC shows a progression with small peaks at 30975 cm^{-1} (B^1, +203 cm^{-1}), 31169 cm^{-1} (B^2) and

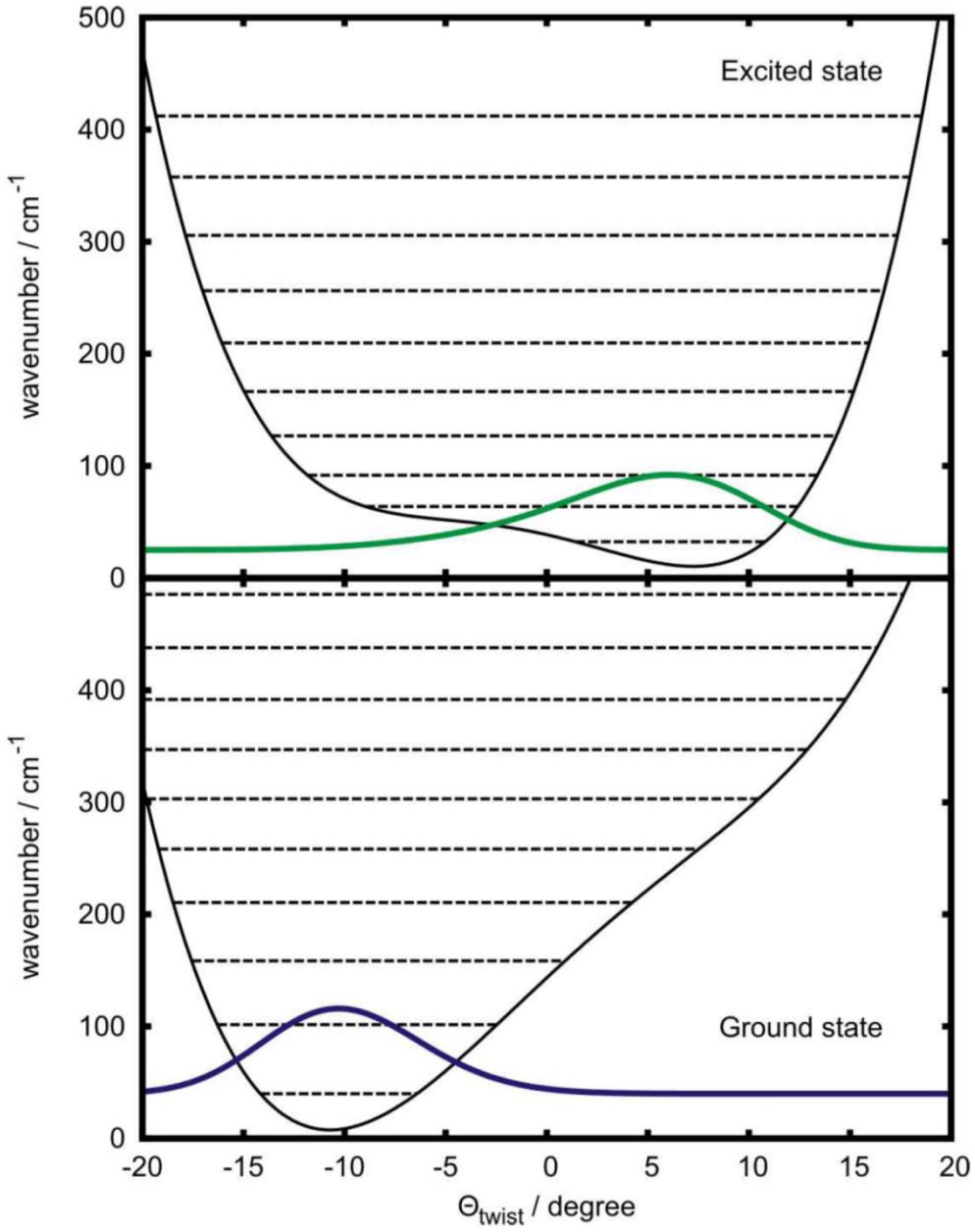

Figure 5.18 The fitted potential energy curve corresponding to the twist motion of the excited state and the corresponding calculated curve of the ground state at the SCS-MP2/TZV(2df,p) level as a function of the twist angle. Calculated energy levels (dashed lines) and the lowest vibrational wave functions (solid colored lines) of these potentials are also shown.

Table 5.8 Term wavenumbers of the S_1 state with respect to the v´ = 0 level, where v´ represents the quantum number of the twist vibration, and intensities of the transitions to these states from the ground state. Results from the SCS-CC2/SV(P) and SCS-CC2/TZV(2df,p) level are compared with those of the fitted potential energy curves and the corresponding experimental values. The standard deviation σ of the difference between calculated and experimental wavenumbers is also shown.

	wavenumber (cm^{-1})				intensity (%)			
v	**SV(P)**	**TZV(2df,p)**	**fit**	**exp.**	**SV(P)**	**TZV(2df,p)**	**fit**	**exp.**
0	0	0	0.0	0	0	0	1.4	2
1	36	28	29.8	30	88	80	16.4	20
2	57	46	60.4	60	0	13	33.4	31
3	86	73	95.5	96	10	5	29.1	23
4	103	104	134.2	134	1	0	14.8	16
5	126	141	176.0	176	1	0	4.8	8
σ	26.8	23.9	0.3					

31369 cm^{-1} (B^3) that can be assigned to the breathing mode. However, significant intensity can only be found in combination with the twist mode T. An unambiguous assignment of the B^n progression proves to be difficult. Numerous combination bands of B with shift mode S and shift with twist mode, ST, are observed. Since the mass of MHPC is between PC and *o*-DHPC, a breathing mode of MHPC at +203 cm^{-1} is perfectly reasonable. Computations predict the breathing mode in the S_1 state at 197 cm^{-1}.

Table 5.9 Parameters for the calculated and fitted one dimensional potential energy curves of the S_1 state of MHPC as a function of θ_{twist}. θ_1 and θ_2 represent the minima, E_0 is the energy for $\theta_{twist} = 0°$, E_2 is the energy at θ_2. The expansion coefficients a_0 to a_4 for the fit curves are also shown.

	SV(P)	**TZV(2df,p)**	**fit**
θ_1	16	11	7.1
θ_2	-13	-10	-
E_0 (cm^{-1})	132	64	19.0
E_2 (cm^{-1})	38	34	-
a_0	132	64	19.0
a_1	2.0875	-1.5906	-3.3912
a_2	-0.9695	-0.8406	-0.0502
a_3	-0.0151	-0.0002	0.0023
a_4	0.0022	0.0038	0.0027

6. Summary

The present work presents investigations on energy and charge transport properties in organic crystals. Chapter 4 treats exciton transport in anthracene, which is an example for weakly coupled π-systems. The electronic coupling parameter is evaluated by the monomer transition density approach. With these and the reorganization energy hopping rates are calculated in the framework of the Marcus theory. Together with the knowledge of the crystal structure, these allow us to calculate the experimental accessible exciton diffusion lengths, whose isotropic part fits nicely within the scattering of experimental values found in the literature. Furthermore, the anisotropy of the exciton diffusion lengths is reproduced qualitatively and quantitatively correct.

This chapter also contains studies about electron and hole transport in both polymorphs (α and β) of perylene. Reorganization energies as well as diffusion coefficients for both crystal structures and types of charge transport were calculated. The best transport is hole transport in β-perylene, but it is strongly isotropic. The preferred transport direction is along the b-axis of the unit cell with couplings of greater than 100 meV. However, there is no transport along the c-axis. The diffusion constant in b-direction is bigger by two orders of magnitude than in c-direction ($62.7 \cdot 10^{-6}$ m^2/s vs. $0.4 \cdot 10^{-6}$ m^2/s). Charge transport is calculated to be strongly anisotropic for holes as well as electrons in both modifications. To verify these results experimental electron mobilities have been compared to the simulations. Good agreement was found with errors of less than 27%.

As it was shown above, the calculation and measurement of transport properties between weakly coupled systems is possible. However, it is difficult to exactly determine the quality of the electronic coupling. For this reason a collaboration about strongly interacting π-systems was started between us and the research group of Prof. Ingo Fischer. There, [2.2]paracyclophanes and its derivates were investigated to show how hydroxyl substitution influences absorption properties. Overall, a combination of SCS-MP2 and SCS-CC2 performs best to address the description of geometric and electronic structures for both ground and excited states of these model systems as well as their parent compounds benzene and phenol. Only [2.2]paracyclophane shows a double minimum potential regarding a twist and shift

motion between the benzene/phenol subunits towards each other. All other systems are less flexible due to their substitution pattern. Almost all [2.2]paracyclophanes display minor changes in their geometric structure upon excitation to the S_1 state: The inter-ring distance shortens, but qualitatively they keep their shift and twist characteristics, although the extent of these deformations diminishes. The exception is *p*-DHPC, which turns from a shifted ground state structure into a twisted excited state structure. Consequently, the intensity of the 0-0 transition cannot be observed experimentally due to small Franck-Condon factors and impurities of *o*-DHPC. In the present thesis, the structures and their changes due to excitation are explained by electrostatic potentials as well as antibonding (bonding) HOMO (LUMO) orbitals.

Adiabatic excitation energies have been corrected by ZPEs and result in accuracies with errors smaller than 0.1 eV. Note that corrections on the B3LYP level worsen the results and one has to apply SCS-CC2 to achieve this accuracy. These calculations allow an interpretation of the experimental [1+1]REMPI spectra. Band progressions of the twist, shift and breathing of the [2.2]paracyclophane skeleton vibrations have been identified and show good agreement to the experiment.

This work shows that the substitution pattern in [2.2]paracyclophanes can have a significant impact on spectroscopic properties. Because these properties are directly linked to the transport properties of these materials, the hereby gained insight can be used to design materials with customized transport properties. It was shown that the SCS-CC2 method is very appropriate to predict the interaction between the π-systems

7. Zusammenfassung

Die vorliegende Arbeit präsentiert theoretische Untersuchungen zu Energie- und Ladungs-Transporteigenschaften in organischen Kristallen. Kapitel 4 behandelt Exzitonentransport in Anthracen bei dem der Fall einer schwachen Kopplung zwischen den π-Systemen vorliegt. Die elektronische Kopplung wird mit dem „monomer transition density“ (MTD) Ansatz berechnet. Aus den Kopplungen und Reorganisationsenergien werden mit der Marcus-Theorie Hüpfraten berechnet. Mit Kenntnis der Kristallstrukturen werden daraus in die experimentell zugänglichen Exzitonendiffusionslängen berechnet, deren isotroper Anteil im Rahmen der Streuung der experimentell zugänglichen Daten reproduziert werden. Auch die Anisotropie der Exzitonendiffusionslängen wird qualitativ und quantitativ im Rahmen der zu erwartenden Messgenauigkeit richtig wiedergegeben.

Weiterhin enthält Kapitel 4 Untersuchungen zum Elektronen- und Lochtransport in den zwei verschiedenen Modifikationen (α und β) von Perylen. Reorganisationsenergien sowie Diffusionskonstanten wurden für beide beide Kristallstrukturen und Typen des Ladungstransports berechnet. Den besten Transport stellt dabei Lochtransport in β-Perylen dar, jedoch ist dieser stark isotrop. Die bevorzugte Transportrichtung is entlang der b-Achse der Einheitszelle mit elektronischen Kopplungen von größer als 100 meV. Allerdings gibt es hier keinerlei Lochtransport in Richtung der c-Achse. Die Diffusionskonstante in Richtung der b-Achse ist um zwei Größenordnungen größer als die in c-Richtung ($62.7 \cdot 10^{-6}$ m^2/s vs. $0.4 \cdot 10^{-6}$ m^2/s). Der Ladungstransport wird sowohl für Löcher, als auch für Elektronen in beiden Perylenmodifikationen immer stark anisotrop berechnet. Um diese Resultate zu verifizieren wurden experimentelle Elektronenmobilitäten in α-Perylen mit den Simulationen verglichen. Es stellte sich eine sehr gute Übereinstimmung heraus mit Fehlern von nur maximal 27%.

Wie oben gezeigt, ist es möglich Transporteigenschaften in zwischen schwach wechselwirkenden Systemen zu berechnen und zu messen. Allerdings ist es hier schwierig, die Güte der zu Grunde liegenden Kopplungsparameter genau anzugeben. Aus diesem Gunde wurde eine Zusammenarbeit über stark wechselwirkede Systeme zwischen uns sowie den Arbeitskreis von Prof. Ingo Fischer begonnen. Dort wurden [2.2]Paracyclophane und dessen Derivate

untersucht um zu zeigen, wie Substitution mit Hydroxylgruppen deren Absorptionseigenschaften beeinflusst. Eine Kombination der SCS-MP2 und SCS-CC2-Methoden liefert hierbei insgesamt die besten Ergebnisse um die geometrischen und elektronischen Strukturen für Grund- und angeregte Zustände dieser Modellsysteme sowie deren Stammmolekülen Benzol und Phenol zu beschreiben. Strukturell weist nur [2.2]Paracyclophan im Grundzustand ein Doppelminimumspotenzial bzgl. Verschiebung und Verdrillung der Benzol/Phenol-einheiten untereinander auf. Alle anderen Systeme sind aufgrund ihrer Substitution weniger flexibel. Fast alle untersuchten [2.2]Paracyclophane zeigen nur geringe Strukturänderungen bei der Anregung in den S_1 Zustand: Der Abstand zwischen den Ringen wird kürzer, aber qualitativ behalten sie ihre Verdrillung und Verschiebung bei, wenn auch das Ausmaß dieser Verzerrungen reduziert wird. Die Ausnahme hierbei ist *p*-DHPC, welches von einer verschoben Struktur im Grundzustand in eine verdrillte Struktur im angeregten Zustand übergeht. Dies hat zur Konsequenz, dass die Intensität des 0-0-Übergangs aufgrund der Franck-Condon Faktoren für *p*-DHPC experimentell nicht mehr beobachtet werden kann und von Verunreinigungen durch *o*-DHPC überdeckt wird. Die Strukturen der Paracyclophane und deren Änderung durch elektronische Übergänge werden in dieser Arbeit durch elektrostatische Potenziale sowie den antibindenen (bindenden) HOMO (LUMO) Orbitalen erklärt.

Adiabatische Anregungsenergien wurden mit Nullpunktsschwingungsenergien korrigiert und liefern Genauigkeiten deren Fehler weniger als 0,1 eV beträgt. Hierbei ist zu beachten, dass eine Korrektur auf B3LYP Niveau die Ergebnisse verschlechtert und man die Berechnung der Schwingungsfrequenzen auf SCS-CC2 durchführen muss um diese Genauigkeit zu erhalten. Aufgrund dieser Rechnungen wurde eine Interpretation der experimentellen [1+1]REMPI Spektren möglich. Bandenprogressionen für die Schwingungen der Verschiebung, der Verdrillung und einer Atmung im [2.2]Paracyclophanskelett wurden identifiziert und zeigen gute Übereinstimmung zum Experiment.

Diese Arbeiten zeigen, dass das Substitutionsschema von [2.2]Paracyclophanen eine erhebliche Auswirkung auf die spektroskopischen Eigenschaften haben kann. Da diese Eigenschaften direkt mit den Transporteigenschaften dieser Materialien verbunden ist, kann das hier gewonnene Verständnis der spektroskopischen Eigenschaften genutzt werden, um Materialien mit maßgeschneiderten

Transporteigenschaften zu designen. Es konnte gezeigt werden, dass die SCS-CC2-Methode sehr gut geeignet ist, die zu Grunde liegende Wechselwirkung zwischen den π-Systemen vorherzusagen.

8. References and Notes

1. http://www.eia.doe.gov/oiaf/ieo/world.html.
2. www.ren21.net.
3. http://www.ren21.net/Portals/97/documents/GSR/REN21_GSR_2010_full_revised%20Sept2010.pdf.
4. http://gcep.stanford.edu/research/exergycharts.html.
5. http://www.desertec.org/.
6. http://en.wikipedia.org/wiki/Cost_of_electricity_by_source.
7. http://www.pro-physik.de/Phy/leadArticle.do?laid=11414.
8. L. Valentini, A. Marrocchi, M. Seri, F. Mengoni, F. Meloni, A. Taticchi and J. M. Kenny, *Thin Solid Films*, 2008, **516**, 7193.
9. M. Riede, T. Mueller, W. Tress, R. Schueppel and K. Leo, *Nanotechnology*, 2008, **19**.
10. B. Kippelen and J. L. Bredas, *Energ Environ Sci*, 2009, **2**, 251-261.
11. G. Dennler, M. C. Scharber and C. J. Brabec, *Adv. Mater.*, 2009, **21**, 1323-1338.
12. G. Chidichimo and L. Filippelli, *Int J Photoenergy*, 2010.
13. C. Deibel and V. Dyakonov, *Rep. Prog. Phys.*, 2010, **73**.
14. H. Hopf, *Angew. Chem. Int. Ed.*, 2008, **47**, 9808-9812.
15. S. Amthor, C. Lambert, S. Dümmler, I. Fischer and J. Schelter, *J. Phys. Chem. A*, 2006, **110**, 5204-5214.
16. C. D. Dimitrakopoulos and P. R. L. Malenfant, *Adv. Mater.*, 2002, **14**, 99.
17. C. R. Newman, C. D. Frisbie, D. A. da Silva, J. L. Bredas, P. C. Ewbank and K. R. Mann, *Chem. Mater.*, 2004, **16**, 4436-4451.
18. A. Facchetti, *Mater. Today*, 2007, **10**, 28-37.
19. V. Subramanian, P. C. Chang, J. B. Lee, S. E. Molesa and S. K. Volkman, *Ieee T Compon Pack T*, 2005, **28**, 742-747.
20. K. Myny, S. Steudel, S. Smout, P. Vicca, F. Furthner, B. van der Putten, A. K. Tripathi, G. H. Gelinck, J. Genoe, W. Dehaene and P. Heremans, *Org. Electron.*, 2010, **11**, 1176-1179.
21. W. Hu, B. Gompf, J. Pflaum, D. Schweitzer and M. Dressel, *Appl. Phys. Lett.*, 2004, **84**, 4720.
22. N. R. Armstrong, W. N. Wang, D. M. Alloway, D. Placencia, E. Ratcliff and M. Brumbach, *Macromol. Rapid Commun.*, 2009, **30**, 717-731.
23. R. Meerheim, B. Lussem and K. Leo, *Proceedings of the IEEE*, 2009, **97**, 1606-1626.
24. A. P. Kulkarni, C. J. Tonzola, A. Babel and S. A. Jenekhe, *Chem. Mater.*, 2004, **16**, 4556-4573.
25. S. Nespurek and J. Sworakowski, *IEEE Eng. Med. Biol. Mag.*, 1994, **13**, 45-57.
26. J. Buback, P. Nuernberger, M. Kullmann, F. Langhojer, R. Schmidt, F. Wurthner and T. Brixner, *J. Phys. Chem. A*, 2011, **115**, 3924-3935.
27. C. Joachim and J. K. Gimzewski, *Chem. Phys. Lett.*, 1997, **265**, 353-357.
28. R. R. Birge, *Am. Sci.*, 1994, **82**, 348-355.
29. B. C. L. Cradall, J., *Nanotechnology: Research and Perspectives*, MIT Press, Cambridge, 1992.
30. M. A. Fox, *Acc. Chem. Res.*, 1999, **32**, 201-207.
31. J. S. Brooks, *Chem. Soc. Rev.*, 2010, **39**, 2667-2694.
32. H. Klauk, *Chem. Soc. Rev.*, 2010, **39**, 2643-2666.

33. C. Katan, F. Terenziani, O. Mongin, M. H. V. Werts, L. Porres, T. Pons, J. Mertz, S. Tretiak and M. Blanchard-Desce, *J. Phys. Chem. A*, 2005, **109**, 3024-3037.
34. A. Masumov, S. Tretiak, J. W. Hong, B. Liu and G. C. Bazan, *J. Chem. Phys.*, 2005, **122**, 224505.
35. P. P. Neelakandan and D. Ramaiah, *Angew. Chem. Int. Ed.*, 2008, **47**, 8407.
36. A. Kahnt, D. M. Guldi, A. d. l. Escosura, M. V. Martinez-Diaz and T. Torres, *J. Mater. Chem.*, 2008, **18**, 77-82.
37. D. S. Seferos, S. A. Trammell, G. C. Bazan and J. G. Kushmerick, *P Natl Acad Sci USA*, 2005, **102**, 8821-8825.
38. G. Bazan, *J. Org. Chem.*, 2007, **72**, 8615-8635.
39. Y. Morisaki and Y. Chujo, *Angew. Chem. Int. Ed.*, 2006, **45**, 6430.
40. D. S. Seferos, A. Szuchmacher Blum, J. G. Kushmerick and G. C. Bazan, *J. Am. Chem. Soc.*, 2006, **128**, 11260-11267.
41. C. J. Brown and A. C. Farthing, *Nature*, 1949, **164**, 915-916.
42. F. Vögtle, *Cyclophane Chemistry*, Wiley-VCH, New York, 1993.
43. H. Takemura, *Cyclophane Chemistry for the 21st Century*, Research-Signpost, Trivan-Drum, 2002.
44. R. G. Hopf, *Modern Cyclophane Chemistry*, Wiley-VCH, Weinheim, 2004.
45. N. V. Vorontsova, G. S. Bystrova, D. Y. Antonov, A. V. Vologzhanina, I. A. Godovikov and M. M. Il'in, *Tetrahedron-Asymmetr*, 2010, **21**, 731-738.
46. C. J. Friedmann, S. Ay and S. Brase, *J. Org. Chem.*, 2010, **75**, 4612-4614.
47. T. Z. Zhang, L. X. Dai and X. L. Hou, *Tetrahedron-Asymmetr*, 2007, **18**, 251-259.
48. D. Y. Antonov, V. I. Rozenberg, T. I. Danilova, Z. A. Starikova and H. Hopf, *Eur. J. Org. Chem.*, 2008, 1038-1048.
49. P. Marquetand, Julius-Maximilians Universität Würzburg, 2007.
50. G. Baym, *Lectures on Quantum Mechanics*, Benjamin-Cummings, Menlo Park, 1973.
51. F. Schwabl, *Quantenmechanik*, Springer Verlag, Berlin Heidelberg, 1993.
52. P. W. Atkins and R. S. Friedman, *Molecular Quantum Mechanics*, Oxford University Press Inc., New York, 1997.
53. G. Wentzel, *Zeitschrift für Physik*, 1926, **40**, 574-589.
54. G. Wentzel, *Zeitschrift für Physik*, 1927, **43**, 524-530.
55. E. Fermi, *Nuclear Physics*, University Of Chicago Press, Chicago, 1950.
56. P. A. M. Dirac, *Proc. R. Soc. London, Ser. A*, 1927, **114**, 243-265.
57. M. Malagoli, V. Coropceanu, D. A. da Silva and J. L. Bredas, *J. Chem. Phys.*, 2004, **120**, 7490-7496.
58. E. B. Wilson, J. C. Decius and P. C. Cross, *Molecular Vibrations*, Dover, New York, 1980.
59. J. R. Reimers, *J. Chem. Phys.*, 2001, **115**, 9103-9109.
60. V. Coropceanu, J. M. Andre, M. Malagoli and J. L. Bredas, *Theor. Chem. Acc.*, 2003, **110**, 59-69.
61. F. Duschinsky, *Acta Physiochimica USSR*, 1937, 551.
62. P. Chen, *Unimolecular and Biomolecular Ion-Molecule Reaction Dynamics*, Wiley VCH, New York, 1994.
63. C. J. Ballhausen, *Molecular Electronic Structures of Transition Metal Complexes*, McGraw-Hill, New York, 1979.
64. R. A. Marcus, *Rev Mod Phys*, 1993, **65**, 599-610.
65. R. A. Marcus, *J. Chem. Phys.*, 1956, **24**, 966.

66. R. A. Marcus, *J. Chem. Phys.*, 1956, **24**, 979.
67. R. A. Marcus, *J. Chem. Phys.*, 1957, **26**, 867.
68. R. A. Marcus, *J. Chem. Phys.*, 1957, **26**, 872.
69. R. A. Marcus, *Discussion of the Faraday Society*, 1960, **29**, 21.
70. R. A. Marcus, *J. Chem. Phys.*, 1963, **67**, 853.
71. R. A. Marcus, *J. Chem. Phys.*, 1965, **43**, 679.
72. R. A. Marcus and N. Sutin, *Biochim. Biophys. Acta*, 1985, **811**, 265.
73. N. S. Hush, *J. Chem. Phys.*, 1958, **28**, 962.
74. F. Jensen, *Introduction to Computational Chemistry*, Wiley-VCH, Weinheim, 2007.
75. R. P. Bell, *Proceedings of the Royal Society*, 1936, **154**, 414.
76. M. G. Evans and M. Polyani, *J. Chem. Soc., Faraday Trans.*, 1936, **32**, 1340.
77. G. S. Hammond, *J. Am. Chem. Soc.*, 1955, **77**, 334.
78. D. M. Guldi and K. D. Asmus, *J. Am. Chem. Soc.*, 1997, **119**, 5744-5745.
79. G. L. Closs, L. T. Calcaterra, N. J. Green, K. W. Penfield and J. R. Miller, *J. Phys. Chem.*, 1986, **90**, 3673-3683.
80. J. E. Norton and J. L. Bredas, *J. Am. Chem. Soc.*, 2008, **130**, 12377-12384.
81. D. P. McMahon and A. Troisi, *J Phys Chem Lett*, 2010, **1**, 941-946.
82. W. Y. Liang, *Physics Education*, 1970, **5**, 226.
83. J. Frenkel, *Phys Rev*, 1931, **37**, 17-44.
84. G. H. Wannier, *Phys Rev*, 1937, **52**, 191-197.
85. R. Peierls, *Ann Phys-Berlin*, 1932, **405**, 905.
86. N. F. Mott, *Transactions of the Faraday Society*, 1938, **34**, 500.
87. P. Pringsheim and A. Kronenberg, *Zeitschrift für Physik*, 1927, **40**, 75.
88. I. V. Obreimov and V. d. Haas, *Proceedings of the Royal Society*, 1929, **31**, 53.
89. I. V. Obreimov and A. F. Prikhotko, *Phys. Z. Sov.*, 1936, **9**, 34.
90. A. S. Davydov, *Zh Eksp Teor Fiz*+, 1948, **18**, 210-218.
91. A. S. Davydov, *Theory of Molecular Excitons*, McGraw-Hill, New York, 1962.
92. Y.-H. Li and S. Gregory, *Geochim. Cosmochim. Acta*, 1974, **38**, 703-714.
93. P. W. Atkins, *Physikalische Chemie*, Wiley-VCH, Weinheim, 2001.
94. V. Stehr, J. Pfister, R. F. Fink, B. Engels and C. Deibel, *Phys Rev B*, 2011.
95. P. T. Landsberg, *European Journal of Physics*, 1981, **2**, 213.
96. V. Coropceanu, J. Cornil, D. A. da Silva, Y. Olivier, R. Silbey and J. L. Bredas, *Chem. Rev.*, 2007, **107**, 2165-2165.
97. S. H. Wen, A. Li, J. L. Song, W. Q. Deng, K. L. Han and W. A. Goddard, *J. Phys. Chem. B*, 2009, **113**, 8813-8819.
98. Y. H. Liu, Y. Xie and Z. Y. Lu, *Chem. Phys.*, 2010, **367**, 160-166.
99. W. Q. Deng and W. A. Goddard, *J. Phys. Chem. B*, 2004, **108**, 8614-8621.
100. P. M. Borsenberger, L. Pautmeier, R. Richert and H. Bassler, *J. Chem. Phys.*, 1991, **94**, 8276-8281.
101. H. Houili, E. Tutis, I. Batistic and L. Zuppiroli, *J. Appl. Phys.*, 2006, **100**.
102. Z. G. Yu, D. L. Smith, A. Saxena, R. L. Martin and A. R. Bishop, *Phys Rev B*, 2001, **6308**.
103. L. Pautmeier, R. Richert and H. Bassler, *Philos Mag B*, 1991, **63**, 587-601.
104. J. M. Casado and J. J. Mejias, *Philos Mag B*, 1994, **70**, 1111-1116.
105. J. Bisquert, *Phys. Chem. Chem. Phys.*, 2008, **10**, 3175-3194.
106. J. A. Anta, I. Mora-Sero, T. Dittrich and J. Bisquert, *Phys. Chem. Chem. Phys.*, 2008, **10**, 4478-4485.
107. S. V. Novikov and G. G. Malliaras, *Phys Status Solidi B*, 2006, **243**, 387-390.

108. Y. Roichman and N. Tessler, *Appl. Phys. Lett.*, 2002, **80**, 1948-1950.
109. S. D. Baranovskii, T. Faber, F. Hensel and P. Thomas, *Physica Status Solidi B-Basic Research*, 1998, **205**, 87-90.
110. M. Abkowitz, H. Bassler and M. Stolka, *Philos Mag B*, 1991, **63**, 201-220.
111. H. Bassler, *Physica Status Solidi B-Basic Research*, 1993, **175**, 15-56.
112. R. Richert, L. Pautmeier and H. Bassler, *Phys. Rev. Lett.*, 1989, **63**, 547-550.
113. Y. Olivier, Université de Mons-Hainaut, 2008.
114. C. Kittel, *Introduction to Solid State Physics*, 8th edn., Wiley VCH, Weinheim, 2005.
115. T. Holstein, *Ann Phys-New York*, 1959, **8**, 343-389.
116. R. E. Peierls, *Quantum Theory of Solids*, 1st ed. edn., Oxford University Press, Oxford, 1955.
117. K. Hannewald, V. M. Stojanovic, J. M. T. Schellekens, P. A. Bobbert, G. Kresse and J. Hafner, *Phys Rev B*, 2004, **69**.
118. K. Hannewald and P. A. Bobbert, *Appl. Phys. Lett.*, 2004, **85**, 1535-1537.
119. F. Ortmann, F. Bechstedt and K. Hannewald, *New J Phys*, 2010, **12**, -.
120. F. Ortmann, F. Bechstedt and K. Hannewald, *J Phys-Condens Mat*, 2010, **22**.
121. A. Troisi, G. Orlandi and J. E. Anthony, *Chem. Mater.*, 2005, **17**, 5024-5031.
122. S. Stafstrom, *Chem. Soc. Rev.*, 2010, **39**, 2484-2499.
123. A. Troisi, *Adv. Mater.*, 2007, **19**, 2000.
124. A. Troisi and G. Orlandi, *Phys. Rev. Lett.*, 2006, **96**.
125. M. Newton, *Chem. Rev.*, 1991, **91**, 767-792.
126. R. F. Fink, J. Pfister, H. M. Zhao and B. Engels, *Chem. Phys.*, 2008, **346**, 275-285.
127. B. O. Roos, *Int. J. Quantum Chem*, 1980, **17**, 175-189.
128. B. O. Roos and P. R. Taylor, *Chem. Phys.*, 1980, **48**, 157-173.
129. P. Siegbahn, A. Heiberg, B. Roos and B. Levy, *Phys. Scr.*, 1980, **21**, 323-327.
130. T. Förster, *Ann Phys-Berlin*, 1948, **2**, 55-75.
131. T. Förster, *Modern Quantum Chemistry, Istanbul Lectures, Part III: Action of Light and Organic Crystals*, Academic Press, New York, 1965.
132. R. Eisenschitz and F. London, *Zeitschrift für Physik*, 1930, **60**, 491.
133. D. A. Bricarello, E. J. Mills, J. Petrlova, J. C. Voss and A. N. Parikh, *J. Lipid Res.*, 2010, **51**, 2731-2738.
134. S. Madathil and K. Fahmy, *J. Biol. Chem.*, 2009, **284**, 28801-28809.
135. I. Pechtl, H. Hocking, D. Kavanagh and P. Barlow, *Mol Immunol*, 2008, **45**, 4124-4124.
136. M. Jose, D. K. Nair, W. D. Altrock, T. Dresbach, E. D. Gundelfinger and W. Zuschratter, *Biophys. J.*, 2008, **94**, 1483-1496.
137. E. Wientjes, I. H. M. van Stokkum, H. van Amerongen and R. Croce, *Biophys. J.*, 2011, **100**, 1372-1380.
138. A. Satake, S. Azuma, Y. Kuramochi, S. Hirota and Y. Kobuke, *Chem-Eur J*, 2011, **17**, 855-865.
139. S. Maruta, D. Kosumi, T. Horibe, R. Fujii, M. Sugisaki, R. J. Cogdell and H. Hashimoto, *Phys Status Solidi B*, 2011, **248**, 403-407.
140. J. Martiskainen, R. Kananavicius, J. Linnanto, H. Lehtivuori, M. Keranen, V. Aumanen, N. Tkachenko and J. Korppi-Tommola, *Photosynth. Res.*, 2011, **107**, 195-207.
141. P. R. Selvin, M. P. Klein and J. E. Hearst, *Biophys. J.*, 1994, **66**, A237-A237.
142. D. D. Thomas, W. F. Carlsen and L. Stryer, *P Natl Acad Sci USA*, 1978, **75**, 5746-5750.

143. D. L. Dexter, *J. Chem. Phys.*, 1953, **21**, 836-850.
144. V. May and O. Kühn, *Charge and Energy Transfer Dynamics in Molecular Systems*, Wiley-VCH, Weinheim, 2005.
145. G. D. Scholes, *Annu. Rev. Phys. Chem.*, 2003, **54**, 57-87.
146. R. McWeeny, *Methods of Molecular Quantum Mechanics*, second edition edn., Academic Press, London, 1992.
147. B. P. Krueger, G. D. Scholes and G. R. Fleming, *J. Phys. Chem. B*, 1998, **102**, 9603-9603.
148. H. Langhals, A. J. Esterbauer, A. Walter, E. Riedle and I. Pugliesi, *J. Am. Chem. Soc.*, 2010, **132**, 16777-16782.
149. T. Helgaker, P. Jorgensen and J. Olsen, *Molecular Electronic Structure Theory, Energy and Wave Functions*, Wiley, Chichester, 2000.
150. A. Hellweg, S. A. Grün and C. Hättig, *Phys. Chem. Chem. Phys.*, 2008, **10**, 4119-4127.
151. O. Christiansen, H. Koch and P. Jørgensen, *Chem. Phys. Lett.*, 1995, **243**, 409-418.
152. C. Hättig and A. Köhn, *J. Chem. Phys.*, 2002, **117**, 6939-6951.
153. C. Hättig and F. Weigend, *J. Chem. Phys.*, 2000, **113**, 5154-5161.
154. E. Sagvolden, F. Furche and A. Kohn, *J Chem Theory Comput*, 2009, **5**, 873-880.
155. A. D. Becke, *J. Chem. Phys.*, 1993, **98**, 5648-5652.
156. J. P. Perdew, K. Burke and M. Ernzerhof, *Phys. Rev. Lett.*, 1996, **77**, 3865-3868.
157. A. D. Becke, *J. Chem. Phys.*, 1993, **98**, 1372-1377.
158. D. A. da Silva, E. G. Kim and J. L. Bredas, *Adv. Mater.*, 2005, **17**, 1072.
159. G. R. Hutchison, M. A. Ratner and T. J. Marks, *J. Am. Chem. Soc.*, 2005, **127**, 16866-16881.
160. V. Lemaur, D. A. Da Silva Filho, V. Coropceanu, M. Lehmann, Y. Geerts, J. Piris, M. G. Debije, A. M. Van de Craats, K. Senthilkumar, L. D. A. Siebbeles, J. M. Warman, J. L. Bredas and J. Cornil, *J. Am. Chem. Soc.*, 2004, **126**, 3271-3279.
161. J. L. Bredas, J. P. Calbert, D. A. da Silva and J. Cornil, *P Natl Acad Sci USA*, 2002, **99**, 5804-5809.
162. O. Kwon, V. Coropceanu, N. E. Gruhn, J. C. Durivage, J. G. Laquindanum, H. E. Katz, J. Cornil and J. L. Bredas, *J. Chem. Phys.*, 2004, **120**, 8186-8194.
163. J. S. Huang and M. Kertesz, *Chem. Phys. Lett.*, 2004, **390**, 110-115.
164. T. Koopmans, *Physica*, 1934, **1**, 104.
165. V. Razumas, K. Larsson, Y. Miezis and T. Nylander, *J. Phys. Chem.*, 1996, **100**, 11766-11774.
166. L. Blancafort and A. A. Voityuk, *J. Phys. Chem. A*, 2006, **110**, 6426-6432.
167. K. Senthilkumar, F. C. Grozema, F. M. Bickelhaupt and L. D. A. Siebbeles, *J. Chem. Phys.*, 2003, **119**, 9809-9817.
168. K. D. Jordan and M. N. Paddonrow, *J. Phys. Chem.*, 1992, **96**, 1188-1196.
169. H. Li, J. L. Bredas and C. Lennartz, *J. Chem. Phys.*, 2007, **126**.
170. E. F. Valeev, V. Coropceanu, D. A. da Silva, S. Salman and J. L. Bredas, *J. Am. Chem. Soc.*, 2006, **128**, 9882-9886.
171. V. V. Eremenko, *Sov. Phys. Solid State*, 1961, **2**, 1426.
172. S. D. Khan-Magometova, *Opt. Spectry.*, 1964, **16**, 475.
173. B. J. Mulder, *Philips Res. Rept.*, 1967, **22**, 142.
174. Y. Takahashi, *J. Phys. Soc. Japan*, 1970, **29**, 525.

175. C. P. Brock and J. D. Dunitz, *Acta Crystallogr B*, 1990, **46**, 795-806.
176. K. Eichkorn, O. Treutler, H. Öhm, M. Häser and R. Ahlrichs, *Chem. Phys. Lett.*, 1995, **242**, 652-660.
177. O. Vahtras, J. Almlof and M. W. Feyereisen, *Chem. Phys. Lett.*, 1993, **213**, 514-518.
178. P. A. M. Dirac, *Proceedings of the Royal Society A*, 1929, **123**, 714.
179. J. C. Slater, *Phys Rev*, 1951, **81**, 385.
180. C. T. Lee, W. T. Yang and R. G. Parr, *Phys Rev B*, 1988, **37**, 785-789.
181. J. Pfister, C. Schon, W. Roth, C. Kaiser, C. Lambert, K. Gruß, H. Braunschweig, I. Fischer, R. F. Rink and B. Engels, *J. Phys. Chem. A*, 2011, **115**, 3583-3591.
182. C. Schon, W. Roth, I. Fischer, J. Pfister, R. F. Fink and B. Engels, *Phys. Chem. Chem. Phys.*, 2011, **13**, 11076 - 11082.
183. C. Schon, W. Roth, I. Fischer, J. Pfister, C. Kaiser, R. F. Fink and B. Engels, *Phys. Chem. Chem. Phys.*, 2010, **12**, 9339-9346.
184. Y. Kawashima, T. Hashimoto, H. Nakano and K. Hirao, *Theor. Chem. Acc.*, 1999, **102**, 49-64.
185. W. R. Lambert, P. M. Felker, J. A. Syage and A. H. Zewail, *J. Chem. Phys.*, 1984, **81**, 2195-2208.
186. R. P. Steiner and J. Michl, *J. Am. Chem. Soc.*, 1978, **100**, 6861-6867.
187. D. M. Donaldson, J. M. Robertson and J. G. White, *Proc R Soc Lon Ser-A*, 1953, **220**, 311-321.
188. J. Tanaka, *Bull. Chem. Soc. Jpn.*, 1963, **36**, 1237-1249.
189. M. Botoshansky, R. H. Herbstein and M. Kapon, *Helv. Chim. Acta*, 2003, **86**, 1113-1128.
190. J. C. Sancho-Garcia, A. J. Perez-Jimenez, Y. Olivier and J. Cornil, *Phys. Chem. Chem. Phys.*, 2010, **12**, 9381-9388.
191. H. Landolt, K.-H. Hellwege and B. Predel, *Landolt-Börnstein*, Springer, Berlin, 1985.
192. R. S. Mulliken, *J. Chem. Phys.*, 1955, **23**, 1997-2011.
193. C. J. H. Schutte, J. E. Bertie, P. R. Bunker, J. T. Hougen, I. M. Mills, J. K. G. Watson and B. P. Winnewisser, *Pure Appl. Chem.*, 1997, **69**, 1641-1649.
194. H. J. Reich and D. J. Cram, *J. Am. Chem. Soc.*, 1969, **91**, 3527.
195. G. M. Sheldrick, *Acta Crystallogr., Sect. A: Fundam. Crystallogr.*, 2008, **64**, 112-122.
196. R. Ahlrichs, S. Böcker, M. Ehrig, K. Eichkorn, S. Elliott, F. Haase, M. Häser, H. Horn, C. Huber, U. Huniar, M. Kattannek, C. Kölmel, M. Kollwitz, C. Ochsenfeld, H. Öhm, A. Schäfer, U. Schneider, O. Treutler, M. von Arnim, F. Weigend, P. Weis and H. Weiss, *TURBOMOLE 5.10*, (2008), University of Karlsruhe: Karlsruhe, Germany.
197. A. Schafer, C. Huber and R. Ahlrichs, *J. Chem. Phys.*, 1994, **100**, 5829-5835.
198. J. P. Perdew, *Phys Rev B*, 1986, **33**, 8822-8824.
199. S. Grimme, *J. Comput. Chem.*, 2006, **27**, 1787-1799.
200. F. Weigend, *Phys. Chem. Chem. Phys.*, 2006, **8**, 1057-1065.
201. F. Weigend and M. Haser, *Theor. Chem. Acc.*, 1997, **97**, 331-340.
202. S. Grimme, *Chemistry - A European Journal*, 2004, **10**, 3423.
203. J. Antony and S. Grimme, *J. Phys. Chem. A*, 2007, **111**, 4862-4868.
204. F. Weigend, M. Häser, H. Patzelt and R. Ahlrichs, *Chem. Phys. Lett.*, 1998, **294**, 143-152.
205. A. Schafer, H. Horn and R. Ahlrichs, *J. Chem. Phys.*, 1992, **97**, 2571-2577.

206. J. A. Pople, A. P. Scott, M. W. Wong and L. Radom, *Isr. J. Chem.*, 1993, **33**, 345-350.
207. A. P. Scott and L. Radom, *J. Phys. Chem.*, 1996, **100**, 16502-16513.
208. P. Sinha, S. E. Boesch, C. M. Gu, R. A. Wheeler and A. K. Wilson, *J. Phys. Chem. A*, 2004, **108**, 9213-9217.
209. S. M. Bachrach, *J. Phys. Chem. A*, 2011, **accepted**.
210. Y. Zhao and D. G. Truhlar, *Org. Lett.*, 2006, **8**, 5753-5755.
211. J. D. Chai and M. Head-Gordon, *Phys. Chem. Chem. Phys.*, 2008, **10**, 6615-6620.
212. H. Hope, J. Bernstein and K. N. Trueblood, *Acta Crystallogr., Sect. B: Struct. Crystallogr. Cryst. Chem.*, 1972, **28**, 1733.
213. K. Lonsdale, H. J. Milledge and K. V. K. Rao, *Proc. R. Soc. London, Ser. A*, 1960, **A 255**, 82.
214. M. Nagel, R. Allmann, S. H. Eltamany and H. Hopf, *Chem. Ber.*, 1982, **115**, 3203.
215. R. Zimmermann, Resonance ionization spectroscopy 1996: Eighth international symposium, 1997.
216. T. L. Shen, J. E. Jackson, J. H. Yeh, D. G. Nocera and G. E. Leroi, *Chem. Phys. Lett.*, 1992, **191**, 149-156.

9. Appendix

Table A.1 V_{ec} in eV for hole transport in α-perylene. Dimers with V_{ec} < 0.001 eV are not shown.

1st monomer	2nd monomer	a	b	c	V_{ec}/eV
2	0	0	1	1	0.049
3	1	0	0	0	0.049
1	0	0	1	0	0.029
2	3	0	1	0	0.029
3	2	0	0	0	0.029
1	0	0	0	0	0.029
3	0	0	0	0	0.020
3	0	0	0	1	0.020
2	1	0	0	0	0.020
2	1	0	0	1	0.020
0	1	1	-1	0	0.011
3	2	1	0	0	0.011
0	1	1	0	0	0.011
3	2	1	-1	0	0.011
1	2	1	0	0	0.009
2	1	1	0	1	0.009
0	3	1	0	0	0.009
3	0	1	0	1	0.009
1	3	1	0	0	0.003
2	0	1	1	1	0.003
0	2	1	-1	0	0.002
3	1	1	0	1	0.002
1	1	1	0	0	0.001
2	2	1	0	0	0.001
3	3	1	0	0	0.001
0	0	1	0	0	0.001
3	1	1	0	0	0.001
0	2	1	-1	-1	0.001

Table A.2 V_{ec} in eV for electron transport in α-perylene. Dimers with V_{ec} < 0.001 eV are not shown.

1st monomer	2nd monomer	a	b	c	V_{ec}/eV
2	0	0	1	1	0.074
3	1	0	0	0	0.074
1	3	0	1	0	0.054
2	0	0	0	1	0.054
2	1	0	0	0	0.043
2	1	0	0	1	0.043
3	0	0	0	0	0.043
3	0	0	0	1	0.043
2	3	0	1	0	0.027
1	0	0	0	0	0.027
3	2	0	0	0	0.027
1	0	0	1	0	0.027
0	3	1	0	0	0.010
1	2	1	0	0	0.010
2	1	1	0	1	0.010
3	0	1	0	1	0.010
2	2	1	0	0	0.009
1	1	1	0	0	0.009
3	3	1	0	0	0.009
0	0	1	0	0	0.009
3	2	1	0	0	0.005
0	1	1	-1	0	0.005
0	1	1	0	0	0.005
3	2	1	-1	0	0.005
1	3	1	0	0	0.003
2	0	1	1	1	0.003
2	0	0	1	0	0.001
3	1	0	0	1	0.001
3	1	1	0	0	0.001
0	2	1	-1	-1	0.001

Table A.3 V_{ec} in eV for hole transport in β-perylene. Dimers with V_{ec} < 0.001 eV are not shown.

1st monomer	2nd monomer	a	b	c	V_{ec}/eV
0	0	0	1	0	0.128
1	1	0	1	0	0.128
0	1	1	0	0	0.010
0	1	1	-1	0	0.010
1	0	1	1	1	0.010
1	0	1	0	1	0.010
0	0	1	0	0	0.002
1	1	1	0	0	0.002
1	1	1	1	0	0.002
0	0	1	-1	0	0.002
1	0	0	0	1	0.001
1	0	0	1	0	0.001
1	0	0	0	0	0.001
1	0	0	1	1	0.001

Table A.4 V_{ec} in eV for electron transport in β-perylene. Dimers with V_{ec} < 0.001 eV are not shown.

1st monomer	2nd monomer	a	b	c	V_{ec}/eV
1	0	0	0	1	0.052
1	0	0	0	0	0.052
1	0	0	1	1	0.052
1	0	0	1	0	0.052
0	0	0	1	0	0.024
1	1	0	1	0	0.024
1	1	1	0	0	0.015
0	0	1	0	0	0.015
0	1	1	-1	0	0.011
0	1	1	0	0	0.011
1	0	1	0	1	0.011
1	0	1	1	1	0.011
0	0	1	-1	0	0.001
1	1	1	1	0	0.001

Danksagung

An dieser Stelle möchte ich all jenen danken, die mir bei der Anfertigung dieser Doktorarbeit mit Rat und Tat zur Seite standen. Diese sind:

Priv.-Doz. Dr. Reinhold Fink, der mir wohl in den letzten vier Jahren mit Abstand am meisten geholfen hat. Ohne seine Anleitung wäre diese Dissertation nicht das, was sie nun ist. Sein offenes Ohr für jegliche Frage, sein Sachverständnis und seine Geduld waren mir immer eine große Hilfe.

Vera Stehr, die durch ihre Physikkenntnisse und Programmierfertigkeiten viele Probleme gelöst hat und mir einen weiteren Blickwinkel für die Fragestellungen ermöglichte. Durch die Kooperation mit ihr wurden viele Aufgaben im Bereich des Ladungstransports erfolgreich bewältigt.

Prof. Dr. Ingo Fischer und Christof Schon. Die ergebnisreiche Kooperation mit ihnen ermöglichte die Veröffentlichung von drei Publikationen. Dabei standen sie mir mit ihrer spektroskopischen Expertise stets zur Seite. Durch die Verknüpfung von Theorie und Praxis konnten hier Fragestellungen angegangen werden, die für die jeweiligen Gruppen alleine nicht lösbar gewesen wären.

Katrin Gruß für die Kristallstrukturen und ihre Geduld mit meinen Fragen.

Conrad Kaiser für die Synthese des *p*-DHPC (oder war´s doch *o*-DHPC?). Wer hätte gedacht, dass dieses Molekül zu drei Veröffentlichungen führen würde. Wir beide sicherlich nicht!

Dr. Hongmei Zhao und Dr. Wenlan Liu, mit denen ich viele sinnvolle, fachbezogene und weniger sinnvolle, dafür lustige, fachfremde Diskussionen führen durfte. Durch sie konnte ich meine Englischkenntnisse aufpolieren und mir die eine oder andere chinesische Phrase aneignen.

Alexander Paasche und Thomas Schmidt. Ich möchte mich für die langen Jahre der freundschaftlichen Zusammenarbeit und insbesondere der Clusterwartung bedanken. Weiterhin konnten sie mir bei diversen kleineren Computerkrankheiten immer aushelfen, was in einem theoretischen Arbeitskreis von hohem Wert ist.

Christoph Grebner, die Person, mit der ich mich wohl in den letzten Jahren am Besten verstanden habe und dessen Kommentare und Ansichten bei mir immer für Erheiterung und Bestätigung sorgten.

Uschi Rüppel, die ich noch nie in meinem Leben Ursula genannt habe, auch wenn man sie so im elmut findet! Ihre lebendige Art und nahezu unendliche Hilfsbereitschaft haben mir das Leben im Arbeitskreis sehr angenehm gemacht. Durch ihren Arbeitseifer halte ich sie für die wohl beste Sekretärin der Universität, und plädiere für eine Gehaltserhöhung!

Die noch nicht namentlich genannten Mitglieder des Arbeitskreises, in deren Mitte ich mich sehr wohl gefühlt habe dank Skiseminaren, unserer Kochgruppe und anderen Aktivitäten.

Besonderen Dank gilt meinem Chef Prof. Dr. Bernd Engels. Ihm danke ich für die Finanzierung unter anderem über das GRK1221 „Steuerung elektronischer Eigenschaften von Aggregaten π-konjugierter Moleküle“. Herzlichen Dank für das interessante Thema, für die fachliche Betreuung, für die vielen Konferenzen, die Touren durch Köln und den freundlichen, aber bestimmten Führungsstil.